UNIVERSITY OF CALIFORNIA SAN DIEGO

Polymer Engineering Methods

to Improve the Interface Between Materials Science and Biology

A Dissertation submitted in partial satisfaction of the requirements
for the degree
Doctor of Philosophy

in

Nanoengineering

by

Yi Zheng

Committee in charge:

Professor Jonathan Pokorski, Chair
Professor Jinhye Bae, Co-Chair
Professor Karen Christman
Professor Darren Lipomi

2023

The Dissertation of Yi Zheng is approved, and it is acceptable in quality and form for publication on microfilm and electronically.

University of California San Diego

2023

DEDICATION

"There is only one heroism in the world: to see the world as it is, and to love it."

- Romain Rolland

To Anyone who and I have been in a period of confusion,

Everything will be **ALRIGHT** in the end (I mean it is just another beginning for myself…).

TABLE OF CONTENTS

LIST OF FIGURES

LIST OF TABLES

LIST OF ABBREVIATIONS

CAD	computer-assisted design
2PP	multiphoton polymerization
DLP	digital light processing
ASD	amorphous solid dispersion
TMGMV	tobacco mosaic green mild virus
RAFT	reversible addition fragmentation chain transfer polymerization
CPMV	cowpea mosaic virus
FDA	Food and Drug Administration
TAAs	Tumor-associated antigens
PRRS	Pathogen pattern recognition receptors
HME	Hot melt extrusion
CNTs	carbon nanotubes
CNCs	cellulose nanocrystals
TMV	tobacco mosaic virus
PEG	poly(ethylene glycol)
PVA	poly(vinyl alcohol)
VLPs	virus-like particles
VNPs	virus nanoparticles
DLS	dynamic light scattering
FPLC	fast protein liquid chromatography
Cryo-EM	cryo-electron microscopy
DIW	direct ink writing
PEDOT:PSS	poly(3,4-ethylenedioxythiophene) polystyrene sulfonate
PET	polyethylene terephthalate
DBSA	dodecylbenzenesulfonic acid
μECoG	micro-Electrocorticography
SNR	signal-to-noise ratio

ACKNOWLEDGEMENTS

I can't imagine how much I will go through for the next five years when I first started my PhD in 2017. I have interacted with too many people for the past five years, good and bad, but I want to express sincere gratitude to all of them for educating me to become a mentally strong and determined person. Among them, I want to first acknowledge my best advisor Jon. I cannot make this done without your professional mentorship, kind emotional support, and the great lab culture that you have been devoted to. Aside from the abundant knowledge of polymer science, chemistry, and molecular biology, you taught me so much about how to become a better person. I become so much more open-minded, chill and laid-back in personality, and down-to-earth when I start picturing new ideas compared to, I was seven years ago when I first met you. More importantly, you showed me how to be a person with dignity. It was a truly wonderful and unique PhD journey having you as my advisor, mentor, and friend.

Next, I want to thank my other dissertation committee members: Prof. Darren Lipomi, Prof. Jinhye Bae, Prof. Karen Christman and Prof. Shengqiang Cai (thank you for the suggestions in my Senate Exam) for their valuable suggestions, comments, and time to my research projects. I want to thank my great collaborators and my good friends as well, Dr. Nicole Steinmetz, Dr. Chao Wang, Eric Chung, Dr. Parker Lee, Yangdong Wang, Fan Zhang. Dr. Shaomin Zhang, and Dr. Kiryl D. Piatkevich, especially Dr. Nanjia Zhou, thank you for the generous support and knowledge sharing with me in the extreme challenging situation, I am so proud of us to publish such a great work. I want to acknowledge the selfless help and informative discussion from Dr. Zhong Chen, Dr. Xiaohe Miao and Dr. Chao Zhang from the Instrumentation and Service Center for Molecular Sciences at Westlake University. Thanks to Guillaume Castillon for the professional TEM knowledge, Dr. Jorge Leganes (you are the happiest person I ever met!), Dr. Ivonne Gonzalez

Gamboa for bringing joyfulness to me as well as knowledge sharing, Dr. Hui Cai (thanks for the selfless academic discussion and offer help for me to move), Dr. Peiran Wei, Dr. Oscar Ortega-Rivera and Dr. Sourabh Shukla for the selfless knowledge sharing. Matt you are so much less serious than before! I appreciate your knowledge sharing.

I am more than appreciative to be in such a great lab and having so many awesome labmates: the first generation Pokorski buddies, especially the three great Dr. ladies: Jacky, Sieun, Melanie who have set the standards to be both pretty and smart for me to look up to, and Parker has been my great mentor and friend. Dr. Derek and Dr. Justin are the best humorous and funny "couple" friends you could ever have, Elizabathe is such a nice listener, and a thinker, Sam and Luis are so nice and caring, Dr. Thai, Dr. Han Sol and Dr. Debika are such great post-doc friends. Dr. David shared so many great stories and insightful discussions with me. I enjoy chatting with Elizabeth, Gaby, Elizabathe and Thai about feminism a lot. I feel grateful to meet the great entrepreneurship folks in the last Fall Quarter I am at UCSD, Dr. Daniel Sun, Dr. Ashley Beckwith, Dr. Yajing Zhao and Dr. Mohammad A. Alkhadra thanks for sharing about your personal journey with me and selfless support with me. Joyce Tiglo, thanks for picking me to join the NSF I-Corps and helping me to start my entrepreneurship journey. Thank you, Dr. Todd and Dr. John, for sharing your entrepreneurial mindset with me, and thanks Sam for all the support and being such a respectful human being. I feel glad to meet such smart and warmly nice peers like Aditya Vasan and Lisa Eshun-Wilson. Hope we can launch our products soon!

Thank you for all my great friends with me all the time. Yue Jin has been my great supporter, and thanks for being there with me without any judgement when I was in the most challenging time. Dr. Yuan Yao and Dr. Yue Hui, Jiajun Shou (and Fish Egg!), Hangyu Chen for the happy time we had in Hangzhou. Tian Fu, Dr. Xinyue Chen, Ting Jiang, Yafei Jian, Sophia Sun, Dr.

Yuesong Shi and Dr. Lu Han thanks for all the emotional support, Dr. Min Tang for being a reliable friend and sharing the same vision with me hoping to change the world to a better place. Dr. Shangting You and Jiaoao Guan for having tripped with me together to so many beautiful nature preserves. Dr. Qiguang He, thank you for all the support and patience, especially during the time when I got stuck in China. Dr. Henry and Deniz thanks for being so funny, nice, and helpful to me.

Lastly but not least, I want to thank my parents, Jide Zheng and Hong Chen. I cannot be so brave and confident without you on my back, thanks for all the support, and the greatest patience when I was in a bad mood (especially my mom here). I want to especially thank my dad for his continuous self-development, and being so generous, optimistic, and patient. And of course, for his professional advice when I encounter difficulties. I hope I will grow into someone respectful like him to provide help to others when in need and hope to generate some research findings that are worth collaborating on. 感谢大家对我的包容与鼓励，还希望自己再接再厉，所向披靡。

Chapter 1, in full, is a reprint of "Green nanofillers: Plant virus reinforcement in hydrophilic polymer nanocomposites" as it appears in *Polymer*, 2018, Zheng, Y., Dougherty, M. L., Konkolewicz, D., Steinmetz, N. F., & Pokorski, J. K. The dissertation author was the primary investigator and author of this paper.

Chapter 2, in full, is a reprint of "Freeze-drying to produce efficacious CPMV virus-like particles" as it appears in *Nano Letters,* 2019, Zheng, Y., Lee, P. W., Wang, C., Thomas, L. D., Stewart, P. L., Steinmetz, N. F., & Pokorski, J. K. The dissertation author was the primary investigator and author.

Chapter 3, in part, is a reprint of "Hot melt extrusion: An emerging manufacturing method for slow and sustained protein delivery" as it appears in *WIREs Nanomedicine and Nanobiotechnology, 2021,* Zheng, Y., & Pokorski, J.K. The dissertation author was the primary investigator and author.

Chapter 4, in full, is a reprint of "Coagulation Bath-Assisted 3D Printing of PEDOT: PSS with High Resolution and Strong Substrate Adhesion for Bioelectronic Devices" as it appears in *Advanced Materials Technologies*, 2022, Zheng, Y., Wang, Y., Zhang, F., Zhang, S., Piatkevich, K. D., Zhou, N., & Pokorski, J. K. The dissertation author was the primary investigator and author.

VITA

2016 Bachelor of Engineering in Biomaterials, Beijing University of Chemical Technology

2017 Master of Science in Macromolecular Science, Case Western Reserve University

2023 Doctor of Philosophy in NanoEngineering, University of California San Diego

PUBLICATIONS

1. **Zheng, Y.**, Wang, Y., Zhang, F., Zhang, S., Piatkevich, K. D., Zhou, N., & Pokorski, J. K. (2022). Coagulation Bath-Assisted 3D Printing of PEDOT: PSS with High Resolution and Strong Substrate Adhesion for Bioelectronic Devices. Advanced Materials Technologies, 2101514.

2. **Zheng, Y.**, & Pokorski, J. K. (2021). Hot melt extrusion: An emerging manufacturing method for slow and sustained protein delivery. Wiley Interdisciplinary Reviews: Nanomedicine and Nanobiotechnology, 13(5), e1712.

3. **Zheng, Y.**, Lee, P. W., Wang, C., Thomas, L. D., Stewart, P. L., Steinmetz, N. F., & Pokorski, J. K. (2019). Freeze-drying to produce efficacious CPMV virus-like particles. Nano letters, 19(3), 2099-2105.

4. **Zheng, Y.**, Dougherty, M. L., Konkolewicz, D., Steinmetz, N. F., & Pokorski, J. K. (2018). Green nanofillers: Plant virus reinforcement in hydrophilic polymer nanocomposites. Polymer, 142, 72-79.

5. Wang, H., Sheng, T., Zhao, S., **Zheng, Y.**, Yu, J., Zhang, Y., & Gu, Z. (2021). Recent advances in transdermal sensors for glucose monitoring. Current Opinion in Biomedical Engineering, 20, 100326.

6. Ortega-Rivera, O. A., Shukla, S., Shin, M. D., Chen, A., Beiss, V., Moreno-Gonzalez, M. A., **Zheng, Y.**, Clark, A. E., Carlin, A. F., Pokorski, J. K., & Steinmetz, N. F. (2021). Cowpea Mosaic Virus Nanoparticle Vaccine Candidates Displaying Peptide Epitopes Can Neutralize the Severe Acute Respiratory Syndrome Coronavirus. ACS infectious diseases, 7(11), 3096- 3110.

7. Lee, P. W., Isarov, S. A., Wallat, J. D., Molugu, S. K., Shukla, S., Sun, J. E., Zhang, J., **Zheng, Y.,** Dougherty M.L., Konkolewicz D., Stewart, P.L., Steinmetz, N.F., Hore, M. J.A., & Pokorski, J. K. (2017). Polymer structure and conformation alter the antigenicity of virus-like particle–polymer conjugates. Journal of the American Chemical Society, 139(9), 3312-3315.

8. Tiu, B. D. B., Kernan, D. L., Tiu, S. B., Wen, A. M., **Zheng, Y.**, Pokorski, J. K., Advincula, R. C., & Steinmetz, N. F. (2017). Electrostatic layer-by-layer construction of fibrous TMV biofilms. Nanoscale, 9(4), 1580-1590

ABSTRACT OF THE DISSERTATION

Polymer Engineering Methods

to Improve the Interface Between Materials Science and Biology

by

Yi Zheng

Doctor of Philosophy in NanoEngineering

University of California San Diego, 2023

Professor Jonathan K. Pokorski, Chair
Professor Jinhye Bae, Co-Chair

Polymers are a group of materials that consist of large molecules (macromolecules) arranged in a pattern of repeating small subunits. They can be classified into natural polymers and synthetic polymers, degradable and non-degradable polymers. A variety of processing techniques are available to process the polymers, including hot melt extrusion, additive manufacturing, and molding. The versatility of polymer science enables its broad applications to range from packaging, and automotive to biomedical concerns. Particularly, the application in biomedical

fields has been of the utmost interest because of the hope of increased longevity and improved quality of life. We here investigated novel polymer engineering methods to improve the interface between materials science and biology and presented a couple of biomedical applications examples based on protein/ polymer composites and non-degradable conductive polymers.

Virus nanoparticles (VNPs) (plant viruses in this thesis) are virus-based nanoparticles with highly symmetrical, polyvalent, and monodisperse structures. They can have icosahedral or rod-shaped geometry. Interestingly, the rod-shaped virus, tobacco mild green mosaic virus (TMGMV) presents as high as 1 GPa Young's modulus and has been utilized as a hydrophilic nanofiller to strengthen the hydrogel networks in this thesis. Cowpea mosaic virus (CPMV) by itself is a potent cancer immunotherapy agent, however, multi-dosage injections are generally required for CPMV treatment. This brings challenges for patients' compliance as well as difficulty in treating hard-to-inject tumors. Here, we introduced a hot melt extrusion (HME) fabrication method to manufacture a sustained CPMV delivery device. A lyophilization-based genomic material elimination method was accidentally discovered in the development of the CPMV implant. A small molecule STING agonist sustained delivery implant was further fabricated based on the reported HME method and the *in vivo* efficacy of the biomedical device was examined with murine models.

Poly(3,4-ethylenedioxythiophene) (PEDOT) is so far the most conductive commercial conductive polymer, however, 3D printable PEDOT is still under development. We here developed a coagulation-bath-assisted method to pattern PEDOT hydrogel, which resulted in high conductivity and biological tissue-matched mechanical properties. A cortex-wide brain-machine interface was fabricated based on the developed technology, and its feasibility has been studied with an electrical stimulation experiment observed by a wide-field microscope.

Polymer science is a highly multidisciplinary subject, we here separately presented the engineering methods of polymers to fabricate protein/polymer composites for drug delivery, and conductive polymers for bioelectronics. However, the idea of protein/polymer composites and bioelectronics can be combined and enabled a “living material” based on bioelectronics. The concept of wirelessly controllable contact lenses for immunotherapy has been proposed in the outlook of the thesis. With the hope of improved human health and increased living quality, the development from the perspective of polymer engineering was studied in this thesis and served for further research investigations.

INTRODUCTION

0.1 Polymers in biomedical fields

Polymers are a group of materials that consist of large molecules (macromolecules) arranged in a pattern of repeating small subunits.[1] Polymers are classified into natural polymers and synthetic polymers based on the origin of the material composition. Synthetic polymers have more controllable and consistent properties than natural polymers. Synthetic polymers also have the advantage of providing high chemical flexibility, yielding great versatility in physical, mechanical, and biological properties. Therefore, they have achieved tremendous success in numerous industrial applications, such as packaging, automotive, consumer goods, aerospace, building, agriculture and medical concerns.[2,3] Particularly, the application in biomedical fields have been among the utmost interest because of the hope of increased longevity and improved quality of life.[4,5] A range of applications have been demonstrated, including general surgical implants such as sutures, tissue adhesives and sealants, and scaffolds for ligament and tendon repair; vascular and cardiovascular intervention, such as vascular stents and vascular grafts; ophthalmology, such as contact lenses and intraocular lenses; dentistry composites[6]; drug delivery systems, such as drug-polymer conjugates, nanoparticles delivery system and sustained delivery implants[7] and more recently bioelectronics, such as skin-inspired wearable devices,[8] brain-machine interface (BMI)[9] and soft robotics[10].

0.1.1 Degradable polymers in biomedical fields

The synthetic polymers used in biomedical applications can be classified based on their degradability. Degradation is an irreversible process, resulting in the change of the polymers' physical properties caused by the breakage of polymer chains through biological or passive activities, such as enzymatic catalysis or hydrolysis, respectively.[11] The degradation leads to the

self-removal of the materials after they have served their function. Therefore, degradable polymers are of utmost interest when selecting the polymer substrates for biomedical applications that require resorption of the polymer, such as drug delivery and tissue engineering. Degradable polymers commonly perform chain-scission on hydrolytically labile chemical bonds, such as esters, anhydrides, acetal, carbonates, amides, urethanes, and phosphates.[12] Among them, poly glycolic acid (PGA), polylactic acid (PLA) and their copolymer poly(lactide-*co*-glycolide) (PLGA) are the earliest degradable polymers ever investigated for biomedical use, and have been approved by FDA for implantation in humans.[13] In the thesis, we investigated the application of PLGA in manufacturing sustained protein and small molecule drugs delivery implants.

0.1.2 Important non-degradable polymers in biomedical fields

In contrast to degradable polymers, non-degradable polymers are a resistant to degradation by hydrolytic and other mechanisms operating in the biological environments. Therefore, they offer attractiveness of biological inertness, high versatility in mechanical properties and a variety of available processing options.[14]

Among all the non-degradable polymers in biomedical fields, polyethylene oxides (PEO) are a widely used hydrophilic polymer. It can increase the biocompatibility, solubility, and bioavailability of incorporated therapeutics, and it is also a great plasticizer used to modify the formulation of drug products. PEO has a range of different molecular weights and in many forms (liquid, wax, solid). It is generally regarded as safe by the FDA and is approved for many applications.[15] We here used the property of low melting temperature of low molecular weight PEG to modulate the formulation of protein/ polymer mixture to achieve desired processability for HME manufactured sustained delivery implants.

Conductive polymers are a special type of non-degradable polymer that possesses unique molecular-level electrical conductivity due to its unique conjugated chain structure. The importance of conductive polymers was recognized by the 2000 Nobel Prize in chemistry (polyacetylene).[16] Polythiophene (PT), polypyrrole (PPy), polyphenylene, polyaniline (PANi) and poly(3,4-ethylene dioxythiophene) (PEDOT) are some of the most widely used conductive polymers in biomedical applications, such as 3D tissue engineering scaffold construction.[17] Among them, PEDOT provides the highest conductivity and therefore are of utmost interest.[18] We here developed a 3D printable PEDOT hydrogel formulation and a bioelectronics to demonstrate the advances of the material.

0.2 Processing and fabrication techniques of polymers for biomedical applications

Synthesis and processing of polymers are both critical design parameters to determine the functional utility of a given polymer. In the biomedical field, polymer synthesis is generally utilized for formulation design, new material development and novel drug delivery systems, while processing and fabrication are utilized to offer a structure, shape, or delivery device of synthesized polymers. Conventional processing techniques of polymers including injection molding, pultrusion, extrusion, and filament winding,[19] they own the merits of ease of scale-up, high throughout and low-cost. Among them, extrusion has been widely used in the pharmaceutical industry. Hot melt extrusion not only offers an efficient and cost-effective processing manner, but also introduces several advantages such as solvent-free processing, enhanced solubility and bioavailability, and improved content uniformity.[20]

Additive manufacturing, also known as 3D printing, is becoming a major processing technique for polymers in biomedical fields. It is a versatile technology platform for computer-assisted design (CAD) and rapid manufacturing. Based on the formation of structures, 3D printing

techniques can be categorized into material extrusion, material jetting, binder jetting, sheer lamination, vat photopolymerization, powder bed fusion, and directed energy deposition.[21] Material extrusion (commonly known as bioprinting) and vat photopolymerization (primarily stereolithography (SLA) and digital light processing (DLP)) are widely used for polymer-based biomedical applications, such as micro scaffolds for tissue engineering. [22–24] Bioprinting offers multi-material printing and thus enables wearable-device prototyping, implants and tissue engineering, among other appplications.[25–28]

Molding is a process that shapes the material into a refined structure with a prefabricated mold. It is a common processing method for polymeric biomedical products. For polymers with high melting temperatures, injection molding is commonly used. Moreover, molding provides a highly versatile fabrication platform, such as a guided model for the development of material[29], and it can be simply designed to a structure used for rapid prototyping.[30] Furthermore, CNC machining is vital in the process of polymers in biomedical fields. It is a precise method to fabricate the top-quality molds used for injection molding as well as the die used for hot melt extrusion.

These processing techniques are not independent, instead they can be combined to use in an innovative way to support the development of a given biomedical application. For example, hot melt extrusion can be used to fabricate an amorphous solid dispersion (ASD) filament, and the filament can be printed into a specific shape to realize certain functionality, such as a star-shaped tablet that attached to the intestine for sustained release[31]. 3D printing can support molding by first setting a disposable designed pattern, then pouring polydimethylsiloxane (PDMS) to create a geometrically unique negative cavity. Processing is not independent of synthesis, however; processing tools can act as a reactor, such as reactive hot melt extrusion[32] and direct-write assembly[33]. In a word, with a targeted application need, polymers can be synthesized, modified,

and processed/ fabricated into various forms, such as gels, solids, sprays, coatings, nanoparticles, and knitted fabrics.

0.3 Hydrogels in biomedical applications

Hydrogels are hydrophilic, three-dimensional networks containing large amounts of water. The high-water content of hydrogels makes them highly biocompatible, and thus hydrogels are considered to have great potential for biomedical applications. Examples of the applications range from tissue engineering, drug delivery, self-healing materials, to biosensors and hemostatic bandages.[34] Poor mechanical properties are the main hindrance for hydrogels; addition of reinforcing filler to the polymer matrix and polymer matrix manipulation are two strategies to strengthen the hydrogel network.[35] Incorporating high mechanical strength nanoparticles into the hydrogel network by mixing is the simplest method;[36] nanoparticles with high aspect ratio serve as a great strengthening agent by absorbing impact energy and providing load transferring. However, there are limited types of commercialized nanotubes, such as carbon nanotubes. Commercially available carbon nanotubes (CNCs) are commonly hydrophobic or even superhydrophobic,[37] and tend to form poor interfaces with hydrogels and form aggregates in the hydrogels. Therefore, new types of hydrophilic nanotubes are needed.

0.4 Drug delivery systems

A polymeric drug delivery system can be formulated in the form of drug-polymer conjugates, nanoparticle-encapsulated delivery systems, and drug delivery implants (scaffold) with the goal of introducing active pharmaceutical ingredients (APIs) into the polymer in a designed manner that controls release. It improves safety and efficacy by controlling the rate, time, and place of release of drugs in the body.[38]

Polymer-drug conjugates and polymer-protein conjugates are common drug delivery systems. The polymer is covalently attached to the non-active functional groups of the API in order to improve the pharmacokinetic and pharmacodynamic properties of pharmaceutics through a variety of measures, including increased plasma half-life, protection of the therapeutic from proteolytic enzymes, reduction in immunogenicity, enhanced stability of therapeutics, enhanced solubility of low MW drugs, and the potential for targeted delivery.[7] A variety of polymers have been used for polymer-drug conjugates, such as PEG, HPMA, and more recently polynorbornene[39]. Similarly, nanoparticle delivery systems can increase the pharmacological properties of APIs by protecting them from degradation, reducing renal clearance and providing sustained release kinetics.[40] However, drug-polymer conjugates and nanoparticle delivery systems generally require repeated intravenous injections in the medical setting. Skin reactions, such as pain, swelling, and soreness are frequently caused by intravenous (IV) injections.[41] Small or collapsed veins pose challenges to healthcare professionals for IV injections ,[42] and patients who have trypanophobia may have difficulty accepting IV injection-related treatment[43]. Furthermore, unexpected special circumstances such as the COVID-19 pandemic may result in limited access to trained health care professions. These factors may affect the efficacy of the treatments associated with repeated IV injections.

Polymer-based drug delivery implants are a polymeric drug delivery device incorporating APIs in a targeted and localized manner and may achieve a therapeutic effect with zero-order drug delivery. Implantation of the drug delivery device normally requires a healthcare professional for insertion, however, it only requires a single administration and leads to no reliance on patient compliance compared to the repeated scheduling of the other types of drug delivery treatments. It also can increase the efficacy of the treatment in general.[44] This new route of drug delivery has

great promise, and therefore a high-throughput manufacturing is needed for the fabrication of such treatments.

0.5 Conductive polymers in bioelectronics

The term "cyborg" was first coined by Manfred E. Clynes and Nathan S. Kline to conceptualize self-regulating extraterrestrial humans in 1960.[45] This conceptual idea is emerging to reality by the milestone contributions on the field of bioelectronics.[46] Bioelectronics is the application of electrical engineering principles to biology, medicine, behavior or health.[47] These devices can be presented in a epidermal and wearable form, implantable form, and ingestible and minimally invasive form, [48] for a range of biomedical applications from biosensors for monitoring of metabolites and nutrients,[49] biomechanics of deep tissue,[50] and neural responses to speech,[51] to therapy devices for cardiac surgery,[52] prosthetic control and cognitive monitoring,[53] and neuromodulation.[54] The materials used for bioelectronics need to mechanically bridge the soft living tissue to rigid electronic system, and enable efficient ionic and electronic signal transmission. Conductive hydrogels possess a unique set of properties to bridge the gap between biology and electronics, providing features for future bioelectronics development. Conductive hydrogels can be classified into ionically conductive hydrogels, conductive nanocomposite hydrogels and conducting polymer hydrogels.[55] Among them, conducting polymer hydrogels, especially PEDOT, own high molecular-level conductivity, and are therefore of utmost interest. Lithography is still the most common method to fabricate PEDOT-based bioelectronics, however, clean-room access is required for lithography and may limit the development of PEDOT-based bioelectronics development. Moreover, 3D structures are preferred for biological tissue engineering to best mimic the morphology and function of natural tissues, yet lithography can only offer 2D planar structures.

Therefore, a 3D printable PEDOT fabrication is required to unearth the full potential of PEDOT in biomedical applications, one of the major goals of this dissertation.

0.6 Dissertation structure

The goal of my dissertation is to utilize the strength of polymers and to apply them to improve their interface with biological systems, including improvement of low-mechanical strength hydrogels, a drug delivery implants fabricated in a high-throughput method and a 3D printable PEDOT technology.

This thesis organically connects polymer science and biomedical engineering to demonstrate the tremendous potential of polymers in biotechnology research. We present a range of work, from the design and characterization of materials and fabricated biomedical devices based on the novel materials, to the application of the biomedical devices in murine models to the demonstration of feasibility and strength of innovative solutions based on polymer synthesis and processing.

Chapter 1 strengthens hydrogel systems by incorporating a rod-shaped plant virus, tobacco mosaic green mild virus (TMGMV). We investigated its great potential as a versatile hydrophilic nanofillers to strengthen different hydrophilic polymeric systems. We used a living polymerization technique – reversible addition fragmentation chain transfer polymerization (RAFT) to synthesize the hydrogel in a controlled manner to ensure the batch-to-batch quality, as well as solution casting as a processing method for films.

Chapter 2 discusses an important finding in which freeze drying results in genomic material being ejected from viral nanoparticles (cowpea mosaic virus, CPMV), likely rendering them non-infectious. We observed the finding during the investigation of the drug delivery implant system (as discussed in Chapter 3), and further improved and developed the findings to a protocol for the fabrication of RNA-free virus-like particles. In chapter 3, we discuss the potential of hot melt

extrusion to produce sustained-release drug delivery implants. We examined feasibility in manufacturing of both protein pharmaceuticals (CPMV) and small molecule drugs (diamidobenzimidazole (diABZI)), and the efficacy of the produced drug delivery implant in murine models.

Chapter 4 describes a coagulation-bath assisted manufacturing method to develop 3D printable PEDOT formulation. The printed material possesses advanced properties such as high conductivity and stable electrochemical properties, and the printing method enables a range of fabrication innovations, such as multi-material 3D printing and simple modification of the printed PEDOT by the change of coagulation bath. With the great properties of the reported PEDOT, we further demonstrate a μECoG cortex-wide neural interface fabricated based on the technique. Lastly, Chapter 5 summarizes the dissertation and provides an outlook to direct the future investigation based on the findings and developments reported in this dissertation.

CHAPTER 1 ROD-SHAPED PLANT VIRUS – REINFORCED HYDROPHILIC POLYMERIC COMPOSITES

1.1 Introduction

Hydrogels are three-dimensional, hydrophilic, polymeric networks with the ability to absorb large quantities of aqueous solution and can swell up to 40-fold when compared with their dry weight[56]. Hydrogels are of particular use in biomedical applications because the high water content mimics that of hydrated tissues, making them a strong candidate to replace native tissue functions for organ replacement[57]. Furthermore, the high water content contributes to their bio-compatibility[58]. Thus hydrogels have many applications in the medical and pharmaceutical sectors, such as contact lenses, wound dressings, hygiene products, and drug delivery systems[59]. A key limiting factor for the use of hydrogels in medicine are their poor mechanical properties[60]. For example, hydrogels can easily collapse and limit cell motility through the gel, which hampers feasibility in regenerative medicine[61]. Additionally, mechanically unstable hydrogels used for cell encapsulation may result in unexpected cell release and death upon collapse[62]. Another example where poor mechanical properties can limit biomedical utility is the durability of contact lenses caused by poor toughness of the hydrogel[63].

For this reason, several different strategies have been used to improve the mechanical properties of polymeric hydrogels, including topological gels, double-network gels and nanocomposite hydrogels[64]. Among these strategies, recent trends indicate significant and growing interest in developing nanocomposite hydrogels with a host of nanofillers. In particular, high aspect ratio nanotubes have become a common addition to hydrogels that improve mechanical properties, and better mimic the natural tissue organization and its resulting composition[65,66]. High aspect ratio nanotubes can not only absorb energy but also allow an ideal transfer of load from the soft polymer matrix to the stiff filler when the composite is put under mechanical stress. In other

words, the modulus of the resulting composite will be similar to the high modulus and strength of the nanofillers[67]. The mechanism of reinforcement for nanotube-enhanced hydrogels is similar to how steel bars reinforce concrete.

Carbon nanotubes (CNTs) are one of the most common nanotubes used as reinforcing agents for hydrogels; they have an extremely high Young's modulus of ~1 TPa[68]. However, it has been generally recognized that the reinforcing efficiency of CNTs largely depends on their dispersion[69]. CNTs have a hydrophobic surface which makes them challenging to fully disperse into aqueous matrices. As a result, CNTs tend to form clusters and bundles in the matrix[70]. These large aggregates of nanofillers initiate cracks in composites, rather than reinforcing them[71]. Besides that, favorable interactions between the nanotubes and matrix are necessary for good load transfer between the two, however, poor interfaces are often formed between CNTs and the surrounding matrix[72]. In order to solve these issues, modifying the surface of nanotubes has been used to improve dispersion within the nanocomposite[72]. Surface modification has been accomplished through attachment of moieties that undergo π–π interactions[73], non-covalent interactions (polymer wrapping)[74], and covalent attachments[75]. However, these methods can affect the integrity of the nanotubes and can be cumbersome to implement. In contrast, cellulose nanocrystals (CNCs) have a high elastic modulus of ~143 GPa and are hydrophilic, which make them good candidates for composite hydrogels[76]. However, the processing method and source of CNCs greatly impacts their morphology. The abundant hydrogen bonding of cellulose causes aggregation of cellulose nanocrystals to form bundles which restricts their future uses[77]. As such, we sought to explore a high aspect ratio protein nanoparticle that can homogenously disperse in aqueous solutions, tobacco mild green mosaic virus (TMGMV).

TMGMV is a plant virus and a characteristic member of the tobamovirus genus; it is closely related to the most common and well-studied member of this genus, tobacco mosaic virus (TMV). TMGMV and TMV share 65% amino acid sequence similarity[78] and are essentially structurally and morphologically identical. However, TMGMV is produced on a vast scale for agricultural uses when compared to TMV, thus TMGMV was chosen as a more economical alternative[79]. Based on its rather narrow host range (compared to TMV)[80], TMGMV may also provide a safer alternative from a biosafety point of view for implementation in materials. TMGMV is a RNA-containing virus comprised of rod-shaped nanoparticles with a geometry of 308 nm in length and 18 nm in diameter (Figure 1.1)[81]. Considering the structural similarity of TMGMV to TMV, TMGMV is likely to exhibit a similar high bending modulus value as TMV, reported at 1 GPa or greater, and provide ample strength to enhance the mechanical properties of hydrogels[82,83]. Viruses provide additional benefits as nanofillers, as they can be chemically and genetically modified to incorporate functional ligands with high density and ordered arrangement[84]. TMV has been extensively researched in materials and nanoscience, showing outstanding potential to direct stem cell differentiation in the field of regenerative medicine[85–89]. Given, the already impressive biological results of tobamovirus particles, this chapter describes the robust mechanical properties of tobamoviruses could be readily translated to the improvement of mechanical features of hydrophilic nanocomposites. In this chapter, we will describe the TMGMV- enhanced polymeric hydrogels system. Due to the utilization of living polymerization - RAFT, we achieved controlled polymerization and assured the mechanical performance batch to batch. Due to the formation of hydrogel, we here use glass scintillation vials as the shaping mold to shape the hydrogel.

1.2 Results and Discussion

1.2.1 Design of the uniform dispersed polymer network

Poly(ethylene glycol) (PEG) hydrogels have been extensively used in biomedical fields as matrices for controlling drug delivery and as cell delivery vehicles for promoting tissue growth and repair[57]. Step-growth, chain-growth, or mixed-mode polymerizations are primary mechanisms to synthesize covalently cross-linked PEG hydrogels, while non-covalent interactions can also drive polymer cross-linking and gel formation[90]. The varying synthetic routes to PEG hydrogels can lead to tunable physicochemical properties such as permeability, molecular diffusivity, equilibrium water content, elasticity, modulus, and degradation rate[59,91]. Reversible addition-fragmentation chain-transfer polymerization (RAFT), a reversible deactivation radical polymerization system offers various advantages when compared to traditional polymerization chemistry, such as more uniform polymers, controlled size and structure, and active chain ends for further derivatization[92]. As such, we chose to use RAFT to synthesize polyPEGMEA hydrogels with PEG dimethacrylate cross-linking.

1.2.2 Fabrication of TMGMV- reinforced composites

In our system, covalent cross-linking restricted chain movements in the PPEGMEA hydrogel, while physical cross-linking between PPEGMEA chains and TMGMV further hinder chain movement and significantly increased toughness of the polymer nanocomposites (Figure 1.1B). Reagents were homogeneously mixed and heated at 45 °C for 3 h to form stable gels. TMGMV was shown to be stable to these conditions (Figure S1.1 and Figure S1.2). TMGMV concentration was varied in the system (0.1 wt%, 0.2 wt%, 0.5 wt%, 1 wt%, 2 wt% and 5 wt%) to determine the effect of filler concentration on gel properties. Due to the hydrophilicity of TMGMV, no phase separation was observed even at the highest concentrations during the gel forming reactions. Pure

PPEGMEA formed transparent yellow gels, while TMGMV nanocomposite gels were opaque yellow due to the addition of TMGMV which scatters light (Figure 1.1C), as TMGMV concentration increases, the opacity of the gels increased.

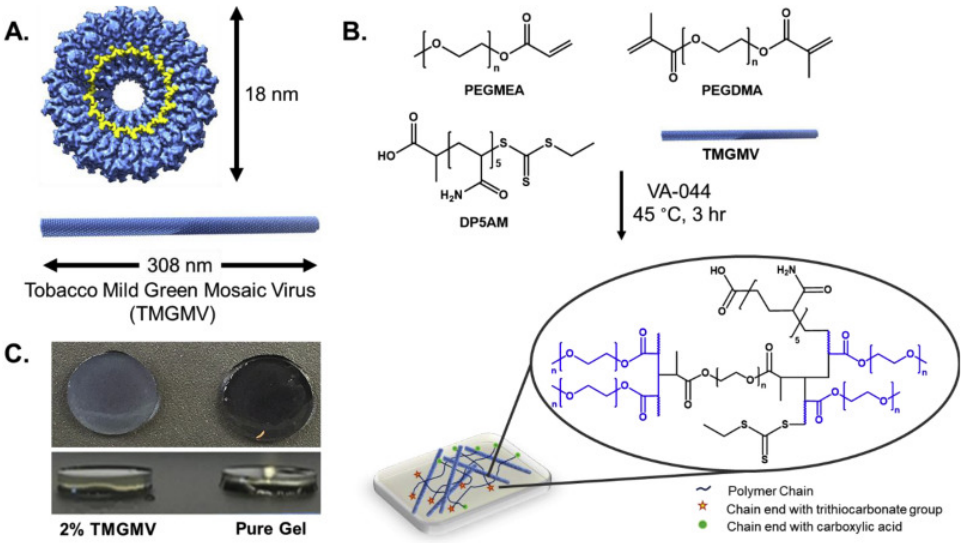

Figure 1.1 Schematic of nanocomposite synthesis and images. A) Surface model of crystal structure of TMGMV: PDB = 1VTM. B) Synthetic scheme for RAFT hydrogel formation. C) Digital micrographs of hydrogels with and without 2 w/w% TMGMV.

1.2.3 Characterizations of TMGMV - reinforced composites

Hydrophilic PEG-based polymers will hydrate and swell in an aqueous environment. Swelling in turn will lead to changes in physical, chemical and biological properties that affect protein adsorption and cell adhesion. The pure hydrogel exhibited an almost six-fold increase in water uptake by weight at equilibrium when compared to the dry weight. As TMGMV concentration increased in nanocomposites, the swelling concomitantly decreased to less than four-fold after saturation (Figure 1.2). This result is expected, as TMGMV forms physical cross-links that were inelastic, limiting swelling. TMGMV may also occupy void spaces within the polymer network and make the hydrogel more compact than a pure hydrogel. As a result, the nanocomposite hydrogel swelled much less than the pure hydrogel due to the rigid nature of the viral nanoparticle

as TMGMV content increased. However, the highest TMGV content (5 wt%) deviated from the trend and had a much higher swelling ratio when compared to other hydrogel composites. The high concentration of TMGMV likely forms large bundles and aggregates, causing defects and voids within the hydrogel matrix (which is further supported by SEM analysis, see below and Figure 1.3). More water may enter in these defects and voids, thus causing the 5 wt% TMGMV hydrogel to deviate from the trend.

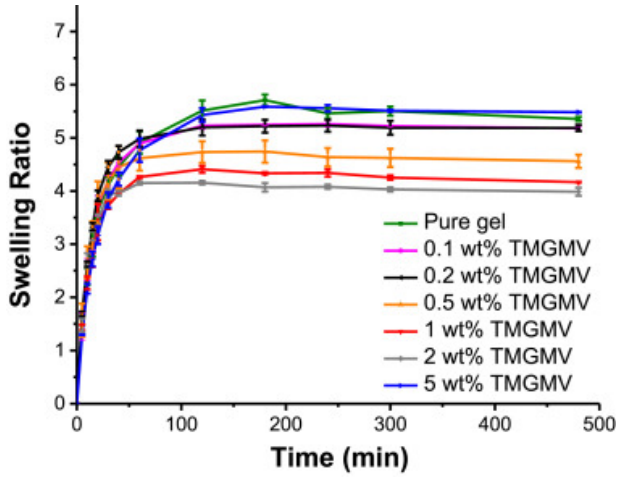

Figure 1.2 Kinetics of hydrogel swelling. Swelling saturation was reached after 300 min for all hydrogels. Swelling ratio is calculated as a relative-fold weight increase.

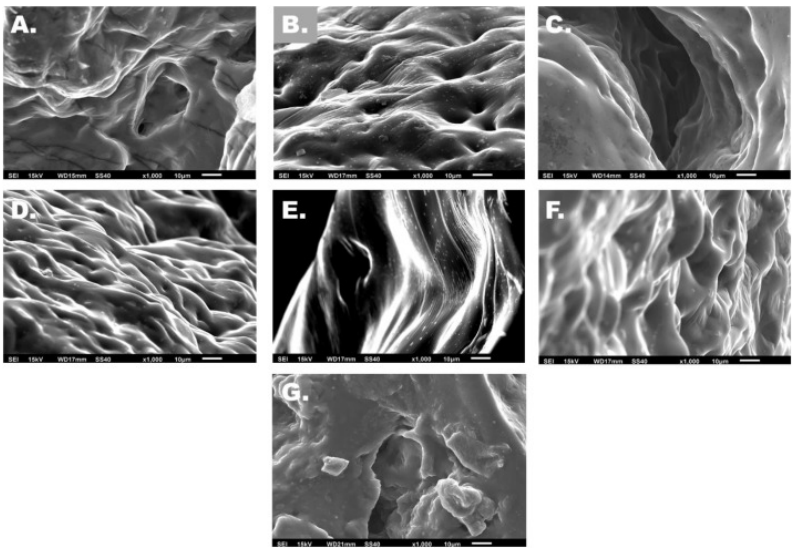

Figure 1.3 SEM micrographs of PPEGMEA/TMGMV hydrogels. A) PPEGMEA hydrogel, B–G) PPEGMEA hydrogel contains 0.1 wt%, 0.2 wt%, 0.5 wt%, 1 wt%, 2 wt% and 5 wt% TMGMV, respectively. Smooth surfaces were observed without obvious aggregates or defects for PPEGMEA hydrogel and PPEGMEA/TMGMV hydrogel at concentrations below 5%. Obvious defects and aggregates can be seen in G.

SEM was carried out to detect the microstructure of lyophilized hydrogels (Figure 1.3). The cross-sectional surfaces of hydrogels were very smooth as expected and no obvious porous structure was observed. Gels comprised of TMGMV between 0 and 2 wt% were very smooth exhibiting a homogenous surface. Additionally, these gels all have consistent morphology without obvious aggregates or defects. This implied that the TMGMV nanofillers were homogenously dispersed in PPEGMEA (Figure 1.3A–F). However, rigid rods have a tendency to self-assemble end to end (also refer to as tail to end) and side to side[93]. When in acidic conditions, TMV particles assemble head to tail which is most likely caused by complementary hydrophobic interactions between the dipolar ends of the helical structure[94]. Similarly, the possibility of interaction between TMGMV particles will largely increase at high concentration even in a neutral environment, which may lead to formation of aggregates and bundles. 5 wt% TMGMV gels showed significant defects and cratering in the micrographs (Figure 1.3 G), which is consistent with the observed increase in swelling ratio.

In sum, low concentrations of TMGMV were homogenously dispersed in the polymer matrix, while high concentrations of TMGMV led to defects in hydrogels. Mechanical testing was used to further study the influence of TMGMV on the mechanical performance of these gels.

The mechanical properties of the nanocomposites were tested with a universal testing machine in compression mode (Figure 1.4). The compressive moduli increased with increasing TMGMV concentrations between 0.1 wt% to 2 wt%, as well as the compressive strength at 30% strain (Figure 1.4). The compressive modulus of nanocomposites with 2 wt% TMGMV increased approximately two-fold compared to the polymer control. The high modulus at 2 wt% was due to high strength of the filler content and physical cross-linking caused by interactions of TMGMV at the interface with the PPEGMEA matrix. When high load was applied to the hydrogel, TMGMV acted as an effective energy transfer agent to distribute energy throughout the matrix as well as an energy absorber. However, once the concentration of TMGMV reached the highest value of 5 wt%, the enhanced mechanical properties of the gel diminished likely caused by aggregation and bundling of the nanofillers observed in previous morphology results.

A.

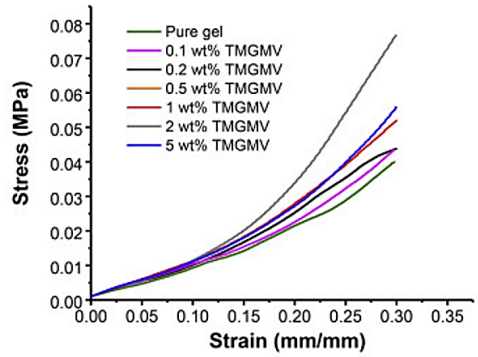

B.

Samples	Stress at 30% Strain (kPa)	Compressive Modulus (kPa)
Pure	40.4 ± 2.1	67.4 ± 0.3
0.1 wt%	44.1 ± 1.2	73.4 ± 0.6
0.2 wt%	45.4 ± 2.8	81.7 ± 0.7
0.5 wt%	52.7 ± 2.7	86.2 ± 4.2
1 wt%	52.8 ± 1.0	99.2 ± 0.8
2 wt%	78.9 ± 12.5	106.6 ± 3.0
5 wt%	54.5 ± 7.3	85.6 ± 2.1

Figure 1.4 Mechanical properties of nanocomposites. A) Compressive properties of nanocomposite hydrogels were determined using compression testing. The effect of TMGMV concentration on the loading during the compression test is shown. B) Compressive moduli increased with an increase of TMGMV concentration in the range of 0.1 wt% to 2 wt%.

In order to better characterize the hydrogels to suit particular applications, shear rheology was conducted to observe mechanical properties. The storage modulus (G′) and the loss modulus (G″), which represented the elastically stored energy (the elastic portion) and the energy dissipated as heat (the viscous portion) within the hydrogel, respectively, were evaluated against non-virus controls using a constant strain rheometer. The nanocomposites were studied at frequencies ranging from 100 rad s−1 to 10 rad s−1 with 0.1% strain. The small strain was applied to ensure that values were in the linear viscoelastic regime, and the frequency was selected to ensure a plateau modulus could be reached.

The G′ values were greater than G″ values and showed a large viscoelastic plateau at all frequencies, indicating that all samples were hydrogels (Figure 1.5). No crossover point between the G′ and G″ was observed, indicating stable elastic properties in the range measured. The relation between viscoelastic properties of the nanocomposites to concentration of TMGMV followed the results of compression testing. The storage modulus increased from a value of around 2500 Pa–9500 Pa with only 0.1 wt% addition of TMGMV. The storage modulus increased with the increasing amounts of TMGMV loading from the range of 0.1 wt% to 1 wt%, and had an almost seven-fold of increase in storage modulus at 1%. However, the increasing trend stopped at the concentration of 2 wt% and dropped significantly when the TMGMV reached a high level of 5 wt%. This further supports the notion that TMGMV forms aggregates and/or leads to structural inhomogeneity at the highest concentrations studied.

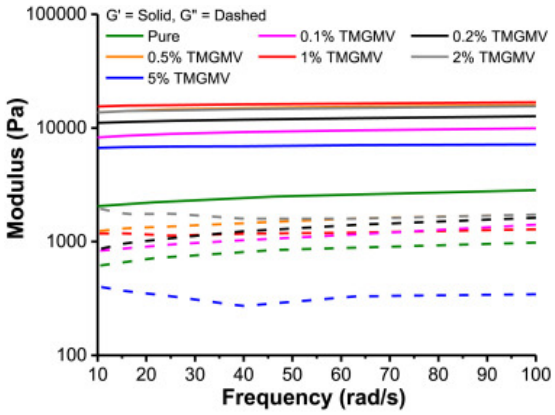

Figure 1.5 Rheological properties of TMGMV composite gels.

Taken together, these data showed that the mechanical properties of chemically-cross-linked composite hydrogels can be significantly improved with the addition of appropriate amounts of TMGMV. High concentrations of TMGMV may cause unwanted aggregation or bundling which may interfere with mechanical enhancement.

1.2.4 Versatility of TMGMV in various hydrophilic systems

After successful reinforcement of PEG hydrogels with TMGMV, we aimed to demonstrate that TMGMV could strengthen other hydrophilic polymer systems. To accomplish this, a series of poly(vinyl alcohol) (PVA) and TMGMV composite films were made. PVA is a commercially available water-soluble synthetic polymer and has excellent film forming and emulsifying properties. PVA films also exhibit high tensile strength and flexibility. Thus, it has been widely used as a matrix for the preparation of nanocomposites. Due to the large number of hydroxyl groups in PVA, hydrogen bonding has a pronounced effect on the bulk properties of PVA materials.

PVA exhibits different crystalline structures based on the stereochemistry of the PVA, which results in different hydrogen bonding patterns[95]. Hydrophobic nanotubes, such as carbon

nanotubes, strictly interact with PVA films by non-covalent forces (van der Waals), and have been shown to largely enhance the mechanical properties of PVA films by forming crystalline coatings around the nanotubes and a strong correlation between the fracture surface and the edge of this crystalline coating[96,97]. However, CNTs still have the problem of hydrophobicity. In order to see whether hydrophilic TMGMV can also strengthen PVA films, we measured the tensile properties as well as the dynamic mechanical properties of PVA/TMGMV nanocomposites. DSC was carried out to measure the impact of TMGMV on the crystallization of PVA films as well as the mechanism of reinforcement.

A series of varied concentration of TMGMV at 0.8 wt%, 1.6 wt%, 3.2 wt% reinforced PVA composite films were manufactured by solvent casting PVA. Tensile properties of the dry PVA films reinforced by the TMGMV were evaluated (Figure 1.6). The tensile modulus increased by ~60% with increasing TMGMV content up to 1.6 wt% (Figure 1.6A). Interestingly, this was followed by a sudden drop at 3.2 wt%, which reduced the value of tensile modulus by half when compared to the neat PVA film. A similar trend was also observed in tensile strength (Figure 1.6B). The highest tensile strength occurs at 1.6 wt% TMGMV content, which increased by ~60%. When the 3.2 wt% of TMGMV was added, the presence of the TMGMV adversely affected the tensile strength.

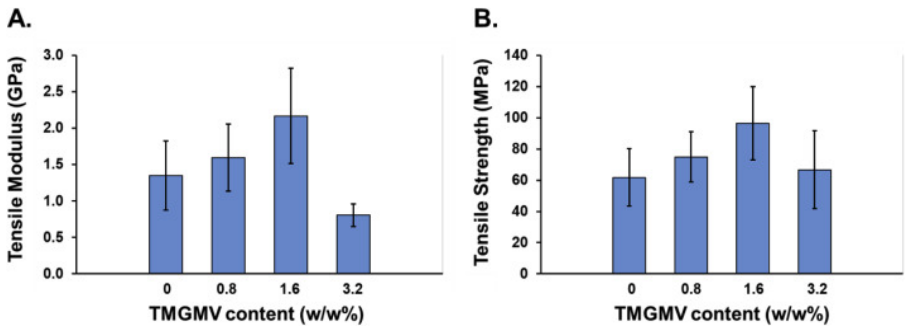

Figure 1.6 Tensile properties of TMGMV/PVA composites. A) Tensile modulus of dry PVA/TMGMV films. B) Tensile strength of dry PVA/TMGMV films.

Similar results were observed in dynamic mechanical analysis. The storage modulus (E') versus temperature curves for neat PVA films and the TMGMV-reinforced nanocomposites were evaluated using DMA in order to examine the thermomechanical properties of the nanocomposites (Figure 1.7). The reinforcing effect of the TMGMV appeared even at low temperatures. When the 1.6 wt% TMGMV was incorporated into the PVA matrix, the E' of the resultant nanocomposite greatly increased, by 42%, and addition of 0.8 wt% resulted in a 34% increase compared to that of the neat PVA film at 37 °C. 3.2 wt% TMGMV, however, only showed a small increase of 6%. PVA films have a crystalline structure due to abundant hydrogen bonding. The nanocomposites underwent strain-induced crystallization during tensile tests, which contributed to the enhancement of mechanical performance[99]. With little strain caused by DMA, there was little strain-induced crystallization compared to tensile testing. Herein, the enhancement of mechanical performance shown by DMA from an improved stiffness of the nanocomposite as well as the dense physical bonding between TMGMV and PVA. However, TMGMV tended to aggregate at 3.2 wt% and led to decreased mechanical performance.

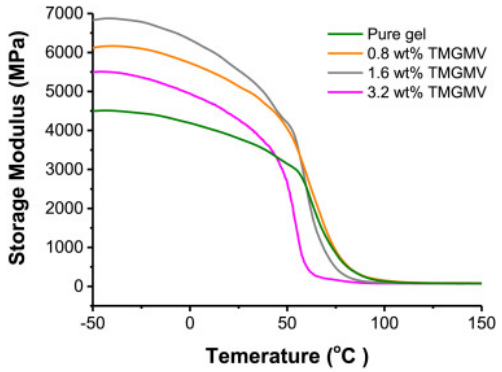

Figure 1.7 Dynamic mechanical analysis. Storage tensile modulus (E′) versus temperature for TMGMV-reinforced PVA nanocomposites.

To confirm the strengthening hypothesis of TMGMV to PVA, differential scanning calorimetry (DSC) measurements were carried out on all films both before and after tensile testing. It can be concluded from Table 1.1 that melting point and crystallinity of nanocomposites were

somewhat dependent on the concentration of TMGMV, showing a slight decrease in melting temperature at low weight percentages of TMGMV. The original melting temperature, however, was recovered upon elongation likely indicating strain induced crystallization. Furthermore, this TMGMV-nucleated and strain-induced crystallization was observed when comparing the original crystallinity and crystallinity after tensile break. Neat PVA showed an increase in crystallinity of 1% following break, while 0.8 wt% TMGV increased by 47.3%, 1.6 wt% TMGMV increased by 54.4%, and 3.2 wt% TMGMV increased by 34.1%. All of which, within error, recovered the original crystallinity of the PVA films.

Table 1.1 Tabulated DSC data of neat PVA and PVA/TMGMV nanocomposite films.

Empty Cell	**PVA**	**0.8 wt% TMGMV**	**1.6 wt% TMGMV**	**3.2 wt% TMGMV**
Original T_m(°C)	207.8 ± 0.8	197.9 ± 8.2	195.3 ± 7.2	209.4 ± 0.3
T_m after tensile break (°C)	208.4 ± 0.3	210.7 ± 4.9	207.1 ± 9.2	212.3 ± 0.0
Original crystallinity (%)	30.5 ± 1.1	21.3 ± 8.4	19.0 ± 3.0	25.7 ± 6.5
Crystallinity after tensile break (%)	30.8 ± 4.3	31 .4 ± 5.6	29.4 ± 5.2	34.4 ± 1.3
Increase (%)	1.0	47.3	54.4	34.1

1.3 Experiment section

1.3.1 Materials

Potassium phosphate monobasic, potassium phosphate dibasic heptahydrate, poly(ethylene glycol) methyl ether acrylate (Mn = 480), poly(ethylene glycol) dimethacrylate, sodium cyanoborohydride, N,N-dimethylformamide (DMF) (99%), dichloromethane (DCM) (99.8%), hexane (95%), ethyl ether, trifluoroacetic acid (TFA), polyvinyl alcohol (average Mw 130,000,

99+% hydrolyzed) were purchased from Sigma Aldrich. TMGMV was purchased from BioProdex. 2,2′ -azobis[2-(2-imidazolin-2-yl)propane] dihydrochloride was purchased from Wako Chemicals USA, Inc.

1.3.2 Synthesis of Oligo(Acrylamide)-chain transfer agent (O-Am-CTA)

The synthesis was adapted from a previously published procedure [36]. To synthesize oligoacrylamide- CTA (O-Am-CTA), RAFT polymerization was used to grow a short oligomer of acrylamide from PAETC in a mixture of methanol and water. AIBN (1 equiv), PAETC (10 equiv) and acrylamide (50.2 equiv) were added to a glass vial with 10 mL of methanol and mixed to dissolve. The reaction mixture was transferred to a round-bottomed flask with 10 mL of water. The flask was purged with nitrogen gas for 10 min to remove oxygen. The reaction was heated to 65 °C in an oil bath to initiate polymerization, and the temperature was maintained for 15 h. Samples, upon completion of the reaction, were analyzed via 1H NMR to confirm at least 95% conversion of the monomer. The final reaction mixture was precipitated by dropwise addition to an ice cold solution of 200 mL of THF and 50 mL of ether. The resulting mixture was centrifuged at 6000 rpm for 2 min until all precipitate had been isolated. The collected product, O-Am-CTA, was left to dry in a fume hood.

1.3.3 Synthesis of PPEGMEA/TMGMV hydrogels

TMGMV was thawed overnight at 4 °C and dialyzed against 10 mM kP pH 7.0 for 48 h to remove any low molecular weight impurities. Then TMGMV was centrifuged using a table top centrifuge at 10,000 rpm for 10 min to remove any aggregates or large plant debris. Purified solutions were stored at 4 °C in 10 mM kP pH 7.0 at concentrations varying between 10 and 20 mg mL−1. UV-visible spectroscopy and fast protein liquid chromatography using a Superose6

column was used to verify the intact state of TMGMV; intact TMGMV elutes at 8 mL with an absorbance ratio of A260/280 of 1.2. UV-visible spectroscopy was used to calculate the concentration of TMGMV with the Beer Lambert Law (ε 260 nm = 3 mL mg–1 cm–1)[81]. 2,2′ -azobis[2-(2-imidazolin-2-yl)propane] dihydrochloride (VA-044) was made into a 16 mg mL−1 initiator stock (KP buffer, pH 7.2). 5 × 10−6 mol of initiator solution was first used to fully dissolve 0.0077 g CTA. PPEGMEA, PEGDMA and TMGMV were added via pipette into a 20 mL glass scintillation vial, the total volume of the added KP buffer was 1 mL. The stoichiometry for hydrogel synthesis was optimized to yield a stable and elastic hydrogel, given the following ratios: monomer: CTA: initiator: crosslinker = 185:3:1:15. The initial conditions were then modified to introduce increasing amounts of the TMGMV nanofillers: 0, 0.1 wt%, 0.2 wt%, 0.5 wt%, 1 wt%, 2 wt% and 5 wt%. After bubbling the precursor solution with nitrogen for 30 min to remove dissolved oxygen, the solution was heated to 45 °C in an oil bath for 3 h to form a gel.

1.3.4 PVA/TMGMV film fabrication

PVA powder was dissolved to 3.25 wt% in deionized water at 85 °C with rapid stirring for 6 h to obtain a colorless transparent homogenous solution. TMGMV was added to 10 mL of room temperature PVA solution at the following concentrations: 0.8 wt%, 1.6 wt%, 3.2 wt%. The solution was vortexed to disperse the filler and poured into a 60 × 15 mm glass petri dish. The aqueous fraction was allowed to evaporate under ambient conditions for ~48 h until film formation was apparent. Residual water in the film was removed in a vacuum oven at 40 °C for 6 h.

1.3.5 Equilibrium swelling

The equilibrium swelling ratio of the PPEGMEA/TMGMV hydrogel was estimated by comparing the dry and the swollen weights. The swollen gel incubated in PBS (pH = 7.2) was

taken out and patted dry with filter paper to measure the weight at regular time intervals until equilibrium was attained. The equilibrium swelling ratio was calculated using Equation (1): W% = (Ws – Wd)/Wd × 100%, where Ws and Wd are the weights of swollen and dry nanocomposites, respectively. The results were performed in triplicate and the error is calculated as standard deviation.

1.3.6 Mechanical testing

Rheology - An ARES G2 rheometer was used to determine the viscoelastic properties of nanocomposite gels, all experiments were performed using the advanced Peltier system (APS) to precisely control temperature and a 25 mm steel parallel plate geometry. The temperature was set at 37 °C and the gap distance was not more than 2 mm. Strain sweep experiments were performed using an oscillatory shear strain ranging from 0.1% to 100% and a constant frequency of 1 Hz. 0.1% strain was in the linear viscoelasticity region and was chosen to use for frequency sweep experiments. Frequency sweep experiments were tested at frequencies ranging from 100 to 10 Hz and an oscillatory shear strain of 0.1%.

Compression testing - An MTS compression system was used to test the mechanical properties of the hydrogels. Cylindrical hydrogel samples with 15.75 mm diameter were subjected to a 30% compressive strain at a strain rate of 0.1 mm s−1. The compressive modulus of each sample was calculated by fitting a line through the linear region of the data measured between 3 and 5% strain. Compression testing results were replicated in triplicate with hydrogels synthesized on different days. Error is calculated as standard deviation.

Tensile testing - Tensile tests were performed using a Zwick testing machine (Xforce P load with a nominal force of 100 N). The cross head speed was 5 mm/min and the preload was 0.1 N. The specimens were cut to a width of 10 mm and a length of 50 mm. The thickness of the sample was

calculated before the test. Tensile testing results were replicated in triplicate with different PVA film batches. Error is calculated as standard deviation.

Dynamic mechanical analysis (DMA) - The DMA was conducted in a film tensile mode on a DMA (Q800, TA, USA) with a temperature range from −50 °C to 150 °C at a heating rate of 10 °C min−1, 0.1% strain is used. DMA results were replicated in triplicate with different PVA film batches.

Scanning electron microscopy - To observe the surface of PPEGMEA hydrogel, scanning electron microscopy (SEM) was performed using a JEOL SEM under an emission voltage of 30 kV.

Differential scanning calorimetry (DSC) - DSC was performed using a TA Q100 with nitrogen as a purging gas. The samples underwent a heat/cool/heat cycle in order to diminish thermal history. The samples were heated from 60 °C to 220 °C at a rate of 10 °C min−1 and held at 220 °C for 1 min to allow the system equilibrate, then cooled the system from 220 °C to 60 °C at a rate of 10 °C min−1 and held at 60 °C for 1 min. An enthalpy of 155 J/g for a theoretical 100% crystalline PVA was used[76]. The crystallinity of neat PVA and PVA/TMGMV composites were calculated by deduction of the weight percentage of TMGMV. DSC results were replicated in triplicate with different PVA films and error is calculated as standard deviation.

1.4 Conclusion

This chapter describes the use of the rod-shaped plant virus, TMGMV, to strengthen different hydrophilic polymer systems. Due to the high modulus of these protein nanotubes, it was found that significant reinforcement could be had even at low concentrations. TMGMV as a reinforcing agent is manufactured in scale using molecular farming and its manufacture is a positive contributor to the environment, rather than non-biological nanofillers. Furthermore, this work complements the improved biological properties seen by other groups and goes into much greater depth regarding the capabilities of viruses to tune mechanical properties of composites. The work presented herein provides another variable that can be tuned in forming composite materials. Given the ubiquity of viruses and the variety of shapes, sizes and particle flexibility, the potential for use in nanocomposites remains largely untapped. In the future, we will continue to investigate new viral particles as fillers, as well as functional viral composites to create biomedical or catalytic materials.

1.5 Supplemental Figures

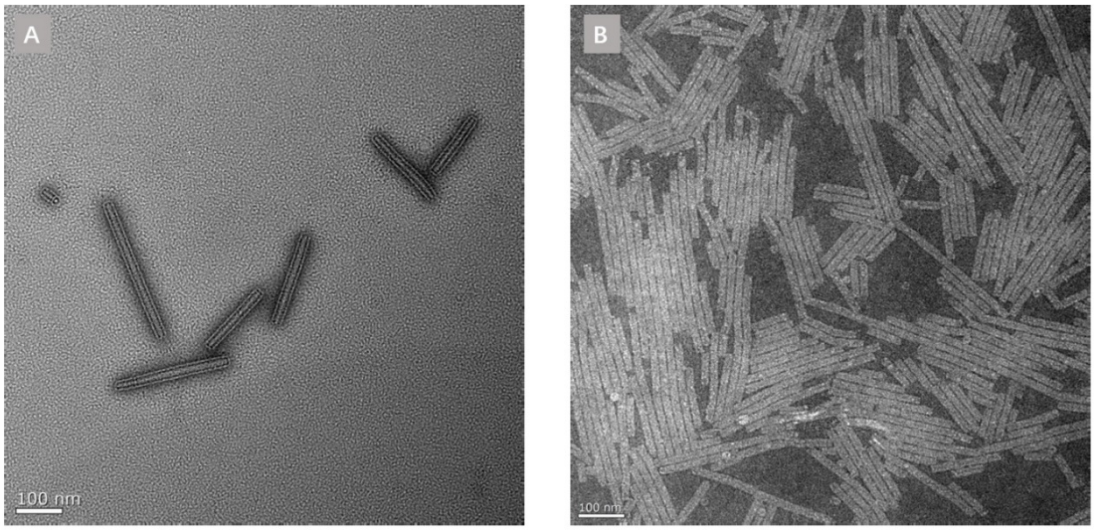

Figure S1.1 Transmission electron micrographs of TMGMV. A) Wild type TMGMV stored at 4°C, B) TMGMV after heating for 3h at 45°C.

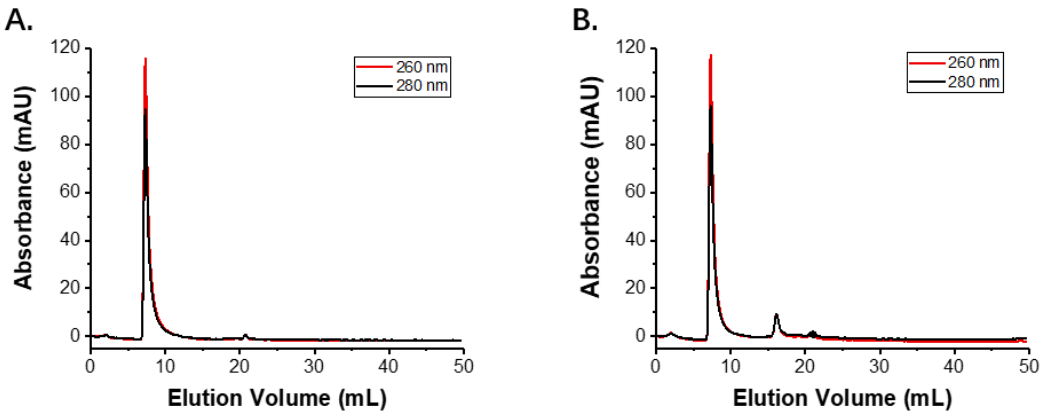

Figure S1.2 FPLC chromatogram of TMGMV. A) Wild type TMGMV stored at 4°C, B) TMGMV after heating for 3h at 45°C.

Acknowledgements

Chapter 1, in full, is a reprint of the material as it appears in “Green nanofillers: Plant virus reinforcement in hydrophilic polymer nanocomposites." Polymer 142 (2018): 72-79, by Yi Zheng, Melissa Lucius Dougherty, Dominik Konkolewicz, Nicole F.Steinmetz, Jonathan K. Pokorski. The dissertation author was the primary investigator and first author.

CHAPTER 2 FREEZE DRYING – BASED METHODOLOGY FOR RNA REMOVAL

2.1 Introduction

Virus-like particles (VLPs) are a subclass of VNPs lacking genomic material but retaining capsid structure and thus can elicit a similar immune response. The absence of nucleic acids makes them noninfectious and eliminates a potential uncontrolled immunostimulatory source, rendering VLPs ideal building blocks for immunotherapy[98]. As such, several VLP vaccines are in clinical trials or have been approved by the FDA. The most well-known is that of Gardasil, consisting of the major capsid protein of several human papilloma virus (HPV) subtypes[99]. VLPs have also been approved and are commonly used for vaccination against hepatitis B and hepatitis E[100]. Beyond this, a vast amount of resources has been dedicated toward preclinical and clinical trials of VLP vaccine candidates[101]. These novel therapies can be directed against the VLP itself or against antigens decorated about the VLP surface[102,103].

One of the most sought-after areas in vaccine development is the development of cancer immunotherapies. A recent exciting innovation in cancer immunotherapy is the generation of in situ cancer vaccines, where an immunostimulatory agent is directly administered to a tumor site. The attributes of this class of therapy are that they are near universal immunotherapies, since no antigen is displayed. In situ vaccines elicit a strong memory antitumor immune response by inducing immunogenic cancer cell death. This facilitates the release of tumor-associated antigens, increases the number of APCs, and enhances their activation to induce antitumor T cell responses, which results in systemic antitumor immunity[104]. One of the tools used for in situ vaccination are oncolytic viruses[105], though the degree of immune responses they induce can relate to the particular virus used, the tumor burden, and the immunogenicity[106]. Additionally, safety concerns like infection and proliferation of oncolytic viruses cannot be eliminated since they are infectious[107].

Recently, plant viruses emerged as in situ vaccines and showed exciting therapeutic effects in curing metastatic disease. In one example, a papaya mosaic virus had the capacity to activate the innate immune system and reduce tumor volume in a murine melanoma model[108]. Furthermore, VLPs derived from cowpea mosaic virus engineered to lack the viral RNA (eCPMV) achieve therapeutic activity in various poorly immunogenic murine tumor models, induce long-lasting antitumor immunity, and eradicate metastatic sites[109]. eCPMV has been further probed and was shown to be a privileged immunotherapy when compared to other plant-derived VLPs and VNPs[110]. eCPMV in combination with radiation was able to successfully treat advanced oral melanoma in companion pets[111]. Lastly, CPMV was formulated into slow release devices for intraperitoneal implantation and single-dose treatment of disseminated ovarian carcinomas[112]. eCPMV has clearly shown great utility and promise for cancer immunotherapy, giving us strong impetus to further this technology.

The current method used to produce eCPMV is the agroinfiltration of Nicotiana bethamiana plants using a plasmid-based expression system[113]. This methodology could potentially introduce immunostimulatory contaminants such as lipopolysaccharide (LPS) during bacterial infiltration[114,115]. Furthermore, scalable implementation of agroinfiltration is tedious, and yields are often significantly lower than wild-type CPMV production[116]. Chemical methods exist for RNA removal from wild-type CPMV; however, trace amounts of RNA remained present, fractionation was necessary to obtain mostly empty particles, and the harsh conditions denatured the capsid over time[117]. In this chapter, we describe a streamlined method to produce eCPMV from native CPMV with a simple experimental setup and low demands for equipment and materials. A simple freeze-drying procedure ejected the RNA from the capsid, and RNase treatment was able to degrade the remaining nucleic acids to produce lyo-eCPMV. A series of characterization

methods were carried out to show that the empty capsids maintained an intact capsid conformation. Furthermore, in situ injection of lyo-eCPMV was observed to have similar efficacy in tumor suppression as bacterially derived eCPMV.

2. 2 Results and discussion

2.2.1 Lyo-eCPMV production and characterization

This method was found empirically and serendipitously when we tried to lyophilize CPMV particles for storage and device manufacture. Removal of RNA from the capsid begins with a slow freeze of a CPMV aqueous solution at −20 °C. Temperature, time, and concentration are critical factors during the freezing step prior to lyophilization. Typical freezing procedures using liquid N2 were unable to fully eject the RNA and resulted in increased aggregation, decreasing the yield (Figure S2.1). Our optimized conditions were a slow freeze in a laboratory freezer (−20 °C, 4 days), followed by lyophilization. These conditions resulted in ideal capsid uniformity and complete removal of RNA. Furthermore, concentration during freezing is a critical factor in obtaining a sufficient yield. At high concentrations (>10 mg/mL), particles aggregate and significant fractions are unable to resuspend following lyophilization; however, dilute solutions of ∼1 mg/mL lessen particle aggregation and maintain high yields. Following freezing, a four-day negative pressure lyophilization was the shortest time required in order to achieve complete dehydration and RNA ejection based on our observations. The resulting dry powder was a mixture of RNA, intact RNA-free particle, and a small amount of protein aggregates; the resulting mixture of components is referred to as lyo-CPMV. Lyo-CPMV was resuspended into buffered solution, and aggregates were removed by centrifugation and decanting. The last step in the lyo-eCPMV preparation is removal of genomic RNA. This was accomplished using RNase A, an extremely common endonuclease, to cleave the RNA into small fragments, which were easily removed using

diafiltration with 100 kDa molecular weight cutoff centrifugal filters. Lyo-eCPMV was recovered at a yield of 0.5 mg of particles/1 g of infected leaf tissue, which was competitive with the yield of eCPMV as prepared by agroinfiltration[118]. (Figure 2.1).

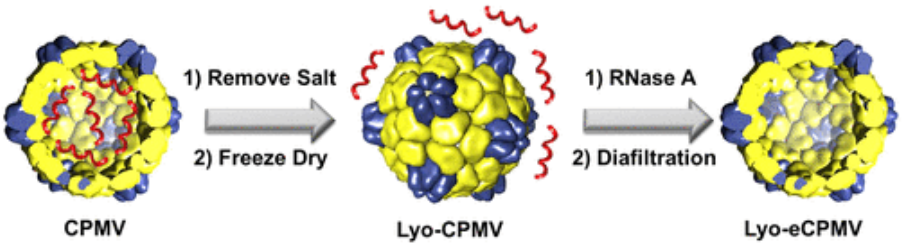

Figure 2.1 Schematic of RNA removal from CPMV. Wild-type CPMV were freeze-dried, which resulted in intact lyo-CMPV. RNase A was used to remove genomic RNA and generate lyo-eCPMV.

2.2.2 Characterization of RNA content of lyo-eCPMV and particles purity

Next, we used agarose gel electrophoresis to determine particle integrity and to test whether residual RNA would be associated with the VLPs following lyophilization (Figure 2.2A). The placement of the bands is determined by the absolute mobility of the viral nanoparticles, which is dependent on the presence of RNA within the capsid. VLPs with RNA have a higher electrophoretic mobility toward the anode based on the additional negative charge contribution from the RNA. Native CPMV is detectable under UV light after EtBr staining and under white light after Coomassie brilliant blue staining, indicating intact particles with encapsulated RNA. (The appearance of a double band can be explained by the two different electrophoretic forms of the virus.)[119] By contrast, lyo-CPMV shows "free" RNA with a high electrophoretic mobility that is not associated with the capsid protein; therefore, suggesting that the RNA was ejected during the lyophilization process. Native CPMV contains a bipartite RNA genome with RNA-1 of 5.9 kb and RNA-2 of 3.5 kb;[120–122] the fact that only one RNA band is observed may suggest that the RNA may be degraded, aggregated, or cannot be resolved under the conditions tested. Taken

together, agarose gel electrophoresis gave a strong indication that RNA was ejected to form a nucleic acid-free VLP.

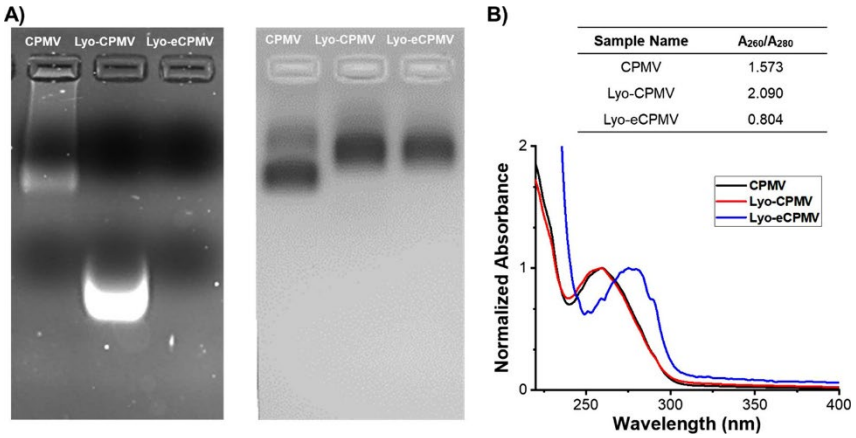

Figure 2.2 Characterization of RNA removal. A) 1% (w/v) agarose gel stained with ethidium bromide (left) and Coomassie brilliant blue (right). B) UV–vis spectra and results for CPMV, lyo-CPMV, and lyo-eCPMV.

Further evidence of RNA removal can be found in UV–vis spectroscopy (Figure 2.2B); the encapsulated nucleic acids have a dominant absorbance peak at 260 nm, while absorbance at 280 nm is reflective of the protein capsid with a lesser contribution from the nucleic acids[123]. The ratio between these two absorbance intensities is indicative of RNA presence in the final material. Wild-type CPMV had a A260/A280 ratio of 1.573, which correlated with the literature value of 1.57[124], and suggested RNA encapsulation, as would be expected[125]. The A260/A280 ratio of lyo-CPMV increased to 2.090, which is a result of RNA unfolding and ejection from the capsid. The unusually high ratio is likely further skewed due to insoluble protein precipitate. Finally, the absorbance ratio of lyo-eCPMV dramatically dropped to 0.804, indicating that nearly all RNA was removed. This value is slightly higher than the literature value of eCPMV at 0.69[124], which likely indicates the presence of trace nucleic acids either in the supernatant or encapsulated within lyo-eCPMV[125]. Agarose gels only give comparative sizes based on the band position of known standards. Dynamic light scattering (DLS) and fast protein liquid chromatography (FPLC) were carried out to further

characterize lyo-CPMV and lyo-eCPMV size and purity, respectively (Figure 2.3). DLS measurements show that the lyophilization and "post-processing" method have minimal impact on particle size and aggregation (Figure 2.3A). The DLS data indicate no obvious aggregates or collapsed protein subunits for wild-type CPMV, with a hydrodynamic radius of 16.4 nm. The hydrodynamic radius of lyo-CPMV is approximately the same (Rh = 14.5 nm), indicating that minimal aggregation occurred during the freeze-drying step. The hydrodynamic radius of lyo-eCPMV (14.9 nm) also showed little difference compared to wild-type CPMV. FPLC was used to determine particle purity (Figure 2.3B). Wild-type CPMV displays a single Gaussian peak centered at ~19 mL elution volume on a Sephacryl 1000 SF 10/300 size exclusion column. In contrast, lyo-CPMV exhibited a single peak centered at a slightly higher elution volume (~21 mL), which is no longer symmetric. This change can be attributed to released RNA remaining in the sample, since the genomic RNA is of reduced hydrodynamic volume relative to the capsid. The FPLC column was unable to fully resolve the capsid and ejected RNA; however, the asymmetric peak can be fit to two Gaussian distributions (Figure S2.2), one that corresponds to an intact capsid and another that is presumably genomic RNA. Further confirmation of this is evidenced by the high A260/A280 ratio (>2.0), indicating a high concentration of nucleic acid. Once RNA was removed by nuclease treatment to form lyo-eCPMV, the A260/A280 ratio was reversed and a stark decrease in total absorbance was seen indicating the absence of nucleic acids. The decrease in total absorbance of lyo-eCPMV is attributed to the significantly lower extinction coefficient at 280 nm of coat protein versus pure RNA (approximately 20-fold less). Furthermore, the elution volume returned to ~19 mL and regained symmetry, indicating intact viral capsids, with a minimal shoulder at lower elution volumes perhaps indicating a small population of aggregated species.

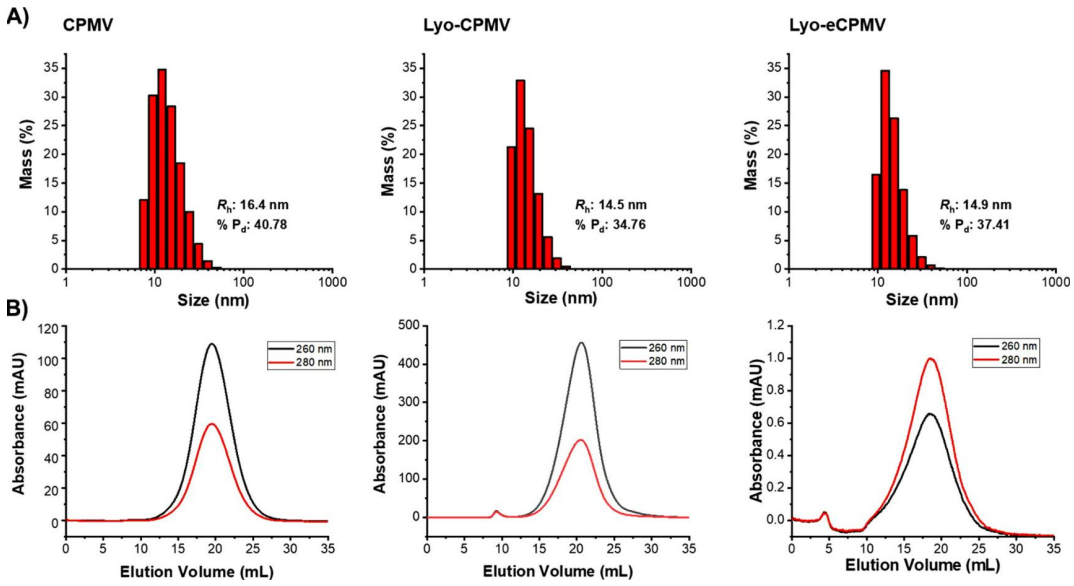

Figure 2.3 Characterization of particle integrity. (A) Dynamic light scattering (DLS). DLS confirms that particles are intact and of appropriate size. The hydrodynamic radius (R_h) and the coefficient of variation (% Pd) are given for wild-type CPMV, lyo-CPMV, and lyo-eCPMV. (B) Fast protein liquid chromatography (FPLC). FPLC chromatograms for all stages of purification. Lyo-CPMV no longer has a Gaussian peak shape, indicating ejected RNA. Peak symmetry is recovered upon removal of free RNA for lyo-eCPMV.

2.2.3 Cryo-EM examination of lyo-eCPMV

The structural integrity of lyo-eCPMV particles was examined by cryo-electron microscopy (cryo-EM). As expected cryo-electron micrographs of wild-type CPMV particles show dark interiors, indicative of the presence of encapsulated RNA (Figure 2.4A)[126]. In contrast, lyo-eCPMV particles have lighter interiors and appear to be empty (Figure 2.4B). The cryo-electron micrographs also suggest that the icosahedral capsids of lyo-eCPMV particles are largely well-formed and structurally intact. Single particle reconstruction was performed on a data set of ~16 600 lyo-eCPMV particle images collected on a 200 kV cryo-electron microscope with an energy filter and a DE20 direct electron detector. Classification with RELION[127] helped to select a relatively homogeneous subset of ~8000 particle images. Refinement of this subset produced a 17 Å resolution structure (Figure 2.5A). The lyo-eCPMV cryo-EM structure reproduces many of

the structural features observed in a cryo-EM structure of naturally occurring eCPMV filtered to the same resolution (Figure 2B) [126].

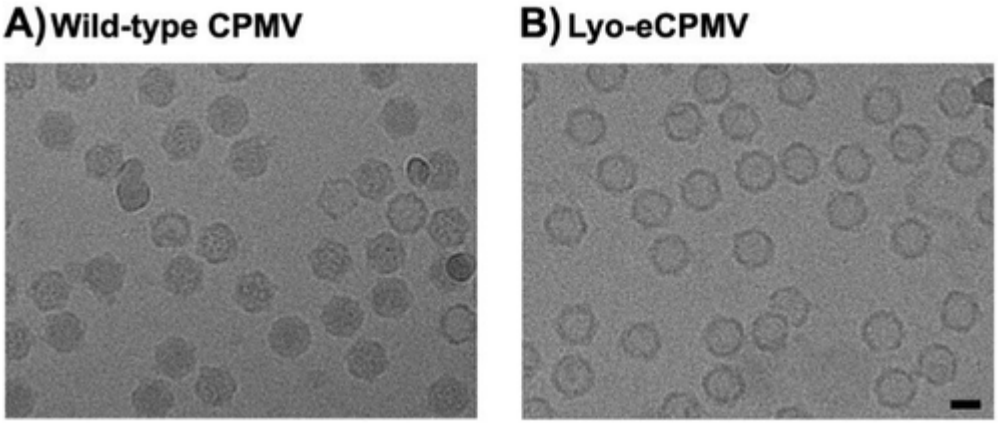

Figure 2.4 Cryo-electron micrographs of wild-type CPMV and Lyo-eCPMV. A) Wild-type CPMV particles appear dark in their interiors due to the presence of viral RNA. B) Lyo-eCPMV particles have lighter interiors and appear to be empty. Both particles appear largely intact and nonaggregated. Scale bar = 200 Å.

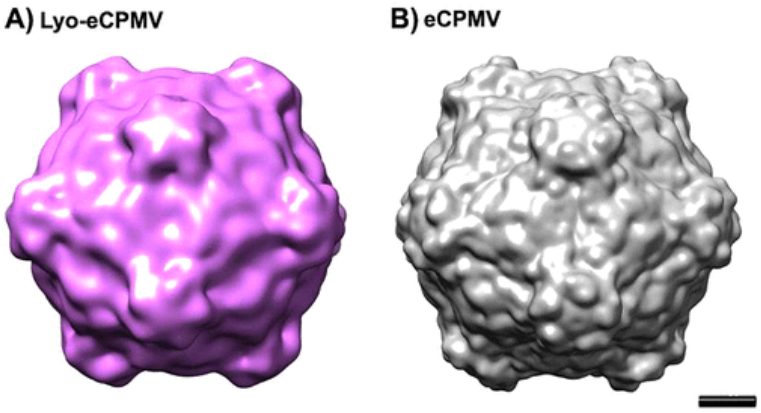

Figure 2.5 Cryo-EM structure of lyo-eCPMV compared to the structure of naturally occurring eCPMV. A) Cryo-EM structure of lyo-eCPMV at 17 Å resolution. B) Cryo-EM structure of naturally occurring eCPMV (EMD: 3562) [126] shown filtered to 17 Å resolution. Scale bar = 50 Å.

The cryo-EM reconstruction of lyo-eCPMV shows slight perturbances in the capsid structure. Few reports have investigated the effects of lyophilization on viral capsids;[128] however, potential reasons for particle disruption can be inferred from literature regarding protein freeze-drying. During the freezing and drying step, the solution concentration drastically increases, and this can

lead to changes in pH and osmolyte concentration[129]. During this process, acidic groups are typically protonated, disrupting salt bridges and leading to destabilization of biological structures. It is likely that this effect caused disruption between the genomic RNA and coat protein. Furthermore, as the osmolyte concentration increases, so too does the internal pressure within the viral capsid, potentially leading to swelling of the particle. It is likely these two effects both destabilize RNA binding and lead to ejection of the RNA from the capsid. Once rehydrated, the disrupted lyo-eCPMV capsid appears to bounce back into a structure that resembles that of naturally occurring eCPMV. Since CPMV does not have pores of sufficient size to allow the genomic RNA to be repackaged in solution, we hypothesize that the freeze-drying and rehydration act as a kinetic trap to exclude RNA from being repackaged.

2.2.4 *in situ* vaccination with lyo-eCPMV

The most critical part of our method to make lyo-eCPMV is its ability to remain as a potent in situ cancer vaccine. Given the structural similarity of lyo-eCPMV to naturally occurring eCPMV as observed by cryo-EM single particle reconstruction, we were optimistic that lyo-eCPMV would retain similar antitumor properties in the treatment of melanoma. To confirm efficacy, we used the same murine melanoma model, with which we had seen success with eCPMV[109]. C57BL/6J male mice were inoculated with B16F10 murine melanoma cells subcutaneously. Treatment was started once the tumor size reached 4–5 mm in the largest diameter. Tumors were injected directly with 100 μg of lyo-eCPMV at 0, 4, and 8 days. By day 4, significant differences were seen in tumor volume, and by day 8, the tumor volume of control mice was nearly an order of magnitude greater than lyo-eCPMV-treated animals. Mice treated with lyo-eCPMV particles had significantly delayed tumor progression, and survival was extended by ∼100% (Figure 2.6). This result was

similar to eCPMV treatment in previous studies, [109] which suggested lyo-eCPMV has comparable immunostimulatory capabilities as eCPMV produced by agroinfiltration.

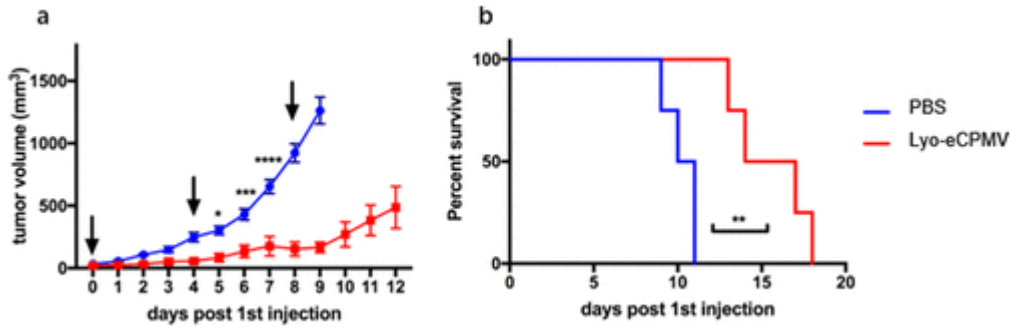

Figure 2.6 *In situ* injection of lyo-eCPMV (lyo-eCPMV) inhibited B16F10 melanoma growth. Lyo-eCPMV (100 μg) were injected intratumorally on days 0, 4, and 8 ($n = 4$). A) Tumor growth curves shown as a relative tumor volume. Data are means ± SEM. Statistical significance was calculated by two-way ANOVA with the Holm–Sidak test. *$p < 0.05$; ***$p < 0.0005$; ****$p < 0.0001$. Growth curves were stopped when the first animal of the corresponding group was sacrificed (tumor volume ≥ 1500 mm^3). B) Survival rates of treated and control mice. Statistical significance was calculated by the Log-rank test. **$p < 0.01$.

2.3 Experiment section

2.3.1 Materials

Ultrapure water (Milli-Q, Bedford, MA) was used for all experiments. Bovine serum albumin (BSA), monosodium phosphate anhydrate, disodium phosphate heptahydrate, sodium chloride, tris base for molecular biology, acetate acid, PEG 8000, RNase A, and SimplyBlue SafeStain were purchased from Fisher Scientific. Bradford reagent was purchased from VWR Life Science. Agarose I, EDTA tetrasodium salt anhydrous, and ethidium bromide were purchased from Amresco. Sucrose was purchased from Acros Organics.

2.3.2 Instrumentation

A VirTis Advantage EL-85 freeze-dryer (SP Scientific, Warminster, PA, USA) was used for lyophilization. Wyatt Möbiuζ was used to perform DLS. Samples were analyzed at 25 °C in plastic

disposable cuvettes with a path length of 10 mm. Fast protein liquid chromatography (FPLC) was performed using a AKTA-FPLC 900 chromatography system equipped with a Sephacryl 1000 SF 10/300 size exclusion column. The mobile phase used is 50 mM phosphate buffer, with 150 mM NaCl (pH 7.4) at a flow rate of 0.4 mL/min. Samples were injected at a concentration of approximately 0.7 mg/mL. Native gel electrophoresis was performed using 1.2% agarose gels in 1× Tris acetate/EDTA (TAE) buffer. TAE buffer (1×) was diluted from 50× TAE stock. (2 mol Tris-base, 0.9 mol acetate acid, and 0.05 mol EDTA in Milli-Q water made up 1 L of 50× TAE stock.) Running buffer is also 1× TAE buffer, and 10 μg of the sample was loaded.

2.3.3 CPMV production and purification

Black-eyed peas (Vigna unguiculata) were inoculated with 100 ng/μL CPMV in 0.1 M potassium phosphate buffer (pH 7.0) and propagated for 18–20 days using established procedures[129]. Briefly, infected leaves were homogenized in a commercial blender in 0.1 M potassium phosphate buffer, pH 7.0. The homogenized mixture was clarified by centrifugation (15 000g, 20 min), followed by a 1:1 chloroform/n-butanol extraction to remove hydrophobic debris. The aqueous layer was precipitated using PEG6000 (4% w/v) and NaCl (0.2M), and the pellet was collected by centrifugation. The resulting pellet was resuspended in 0.1 M potassium phosphate buffer and purified using a 10–40% sucrose density gradient.

2.3.4 Lyo-eCPMV production

CPMV was first filtered into deionized water using a 100 K Amicon Ultra-4 centrifugal filter at 6000 rpm (Eppendorf 5810 centrifuge) at least 6 times in order to remove salts and low molecular weight impurities from the product. The filtered CPMV stock was then adjusted to 1 mg/mL with deionized water and slowly frozen at −20 °C in a laboratory freezer for at least 4 days. The tray

freeze-dryer was used with a shelf temperature of 25 °C and an ultimate chamber pressure of 5 μbar. The final lyophilized particles exhibited a slightly yellow flocculent appearance.

Lyophilized particles were resuspended in 1 mL of 0.1 M potassium phosphate buffer (pH 7.0) overnight. Resuspended particles were more turbid compared to the original CPMV suspension, indicating incomplete suspension of the original material. Centrifugation (Eppendorf 5424) was performed at 1000 rpm for 5 min to precipitate the turbid material. The supernatant was collected and adjusted to ~1 mg/mL as determined by the Bradford assay. RNase A was then added to the resuspended lyo-CPMV at a concentration of 50 μg/mL. The samples were vortexed and incubated at room temperature for 15 min with gentle mixing by vortex at the level of 1.5. Following RNase treatment, 100 K Amicon Ultra-4 centrifugal filters were used to remove RNase A and degraded RNA (6000 rpm in an Eppendorf 5810R, 0.1 M KP, pH 7). Filtration was performed at least 6 times to completely remove degraded RNA fragments. Finally, the recovered particles were centrifuged at 10 000 rpm (Eppendorf 5424) for 5 min to remove any particulate aggregates.

2.3.5 Cryo specimen preparation and image collection

Three μL aliquots of lyophilized, RNase A-treated, and filtered CPMV (lyo-eCPMV) at 0.5 mg/mL were applied onto 300 mesh copper grids (Quantifoil R2/2) that were glow discharged for 20 s at 20 mA. Excess solution was blotted for 1 s with filter paper, and the grids were immediately plunged into liquid ethane using a ThermoFisher/FEI Vitrobot. Cryo-EM data was collected on a JEOL 2200 FS microscope (FEG, in-column energy filter) operated at 200 kV. Images were recorded on a Direct Electron DE 20 detector at a magnification of 60 000× corresponding to a pixel value of 1.12 Å. Each micrograph was generated by averaging 32 individual dose fractionated frames collected at a rate of 20 frames/s for 1.6 s with an accumulated total dose of 63.3

electrons/pixel. The frames were motion corrected and summed into a single micrograph and processed. The micrographs were collected with underfocus values in the range of 1.6–3.5 μm.

2.3.6 Image processing and 3D reconstruction

Particle selection was performed using the EMAN2 software suite[130]. A set of 16 628 particle images was selected from 181 cryo-electron micrographs. The defocus and astigmatism values for each of the micrographs were estimated using CTFFIND 4.1[131]. The RELION 2.1 software suite was used for further image processing[127]. After the RELION 2D classification step, particle images in 40 out of 82 2D classes were selected for further processing (14 059 particle images selected). The cryo-EM structure of naturally empty eCPMV at 4.25 Å resolution was obtained from the Electron Microscopy Data Bank (EMD-3562)[126] and was used as a reference map during 3D classification. The CPMV reference map was rotated to the I1 symmetry orientation and low-pass filtered to 10 Å resolution. After the RELION 3D classification step, particle images in 1 of 10 3D classes were selected for independent refinement with RELION 3D autorefine. This class contains 8 135 particle images (58% of the total data set) and refined to 17 Å resolution (at the Fourier Shell Correlation 0.143 threshold). Images were created with UCSF Chimera[132].

2.3.7 Cell culture and immunization of mice

Cell culture - B16F10 cells (ATCC) were cultured in Dulbecco's modified Eagle's media (DMEM, Life Technologies) at 37 °C in a 5% CO2 humidified atmosphere, supplemented with 10% (v/v) fetal bovine serum (FBS, Atlanta Biologicals) and 1% (v/v) penicillin–streptomycin (Life Technologies).

Immunization of mice - All experiments were conducted in accordance with Case Western Reserve University's IACUC. Also, 1.25 × 105 B16F10 cells/30 μL of PBS was introduced intradermally into the right flank of a C57BL/6J male (Jackson Laboratory). Animals were

observed closely, and tumor size was measured with digital calipers. Tumor volumes were calculated as V = 0.5 (a × b2); where a is the length and b is the width of the tumor. Once tumor size reached 4–5 mm in the largest diameter, mice were randomized to the experimental groups: PBS and lyo-eCPMV (n = 4). Then, 100 μg of lyo-eCPMV and sterile PBS were injected into tumors in a volume of 30 μL every 4 days for a total of 3 treatments. Animals were sacrificed when the tumors reached a volume > 1500 mm3.

2.4 Conclusion

eCPMV has seen enormous potential as an *in situ* cancer vaccine and has immunological traits that make it uniquely poised among viral nanoparticles to make a clinical impact. The methodology described within builds a bridge between those studying eCPMV for its curative properties and those that are interested in its downstream manufacturing. Freeze-drying is a standard method for preparing biopharmaceuticals, and particularly viral vaccines. Several reports have investigated the effects of freeze-drying on live viruses in the past and have observed varying levels of viral inactivation. This report, in contrast, shows complete inactivation and removal of genomic RNA from the capsid particle, rendering it noninfectious. Our methodology has the potential to replace agroinfiltration methods, thus eliminating potential bacterial contamination. In addition, our method starts with wild-type CPMV, which theoretically can be abundantly produced, and the postprocessing conditions utilize equipment that is standard to the pharmaceutical industry. Given our results, the potential exists that careful optimization of freeze-drying procedures would replicate these results for other viral vaccines and should be further investigated. In sum, our results represent a novel way to prepare genome-free virus-like particles from infectious virions while maintaining efficacy.

2.5 Supplemental Figures

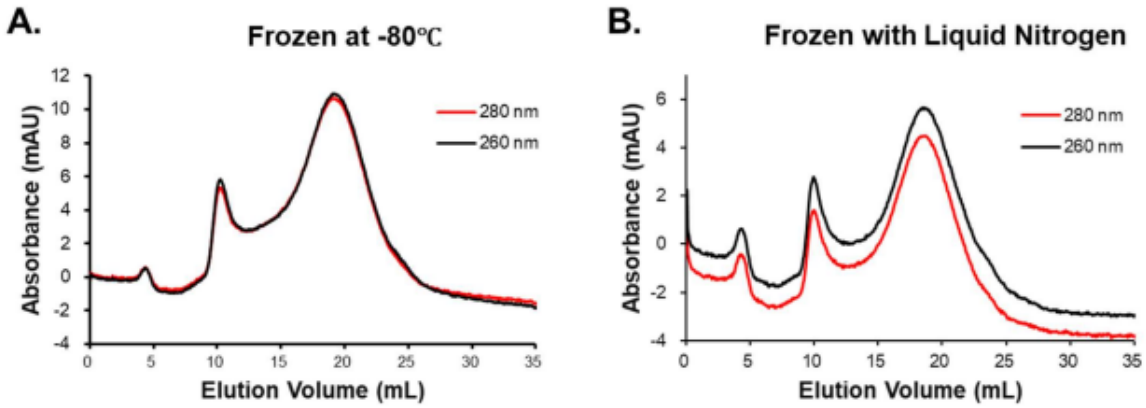

Figure S2.1Freezing temperature and CPMV concentration are crucial for the processing of lyoeCPMV. A) ~2 mg/mL of CPMV is frozen at -80°C. FPLC indicates substantial aggregation and incomplete removal of RNA. B) ~2 mg/mL of CPMV was frozen using liquid nitrogen. Again, substantial agreggation is seen as well is incomplete removal of RNA.

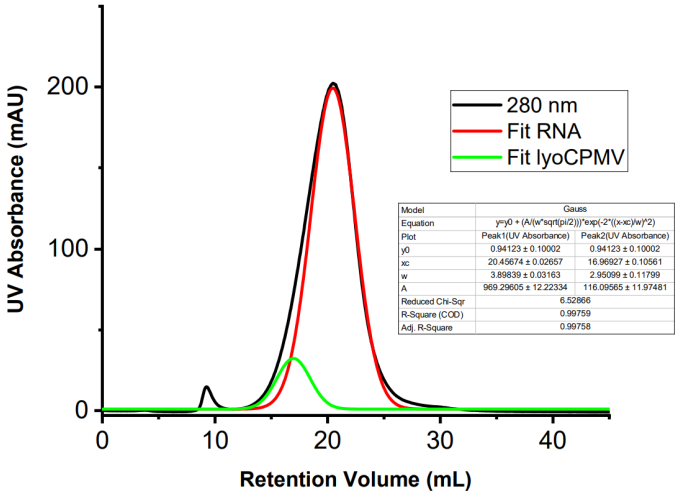

Figure S2.2 Gaussian peak fit of lyo-CPMV. The asymmetric peak is caused by the presence of two species in mixture, RNA and eCPMV.

Acknowledgements

Chapter 2, in full, is a reprint of the material as it appears in “Freeze-drying to produce efficacious CPMV virus-like particles." Nano letters 19.3 (2019): 2099-2105, by Yi Zheng, Parker W. Lee, Chao Wang, Linda D. Thomas, Phoebe L. Stewart, Nicole F. Steinmetz, and Jonathan K. Pokorski. The dissertation author was the primary investigator and first author.

CHAPTER 3 PROGRESS TOWARD A SINGLE DOSE SUSTAINED RELEASE IMMUNOTHERAPY

3.1 Introduction

Cancer immunotherapy has shifted the paradigm for the treatment of cancer. Instead of directly killing cancer cells as with chemotherapy, immunotherapy utilizes the patient's own immune response and leads to the benefits of fewer side effects, ability to be more personalized, and potentially being effective for the patient's entire life.[133,134] The potency of the therapy has been acknowledged by several types of Food and Drug Administration (FDA) approved immunotherapies, such as checkpoint inhibitors and chimeric antigen receptor T cell (CAR-T cell) therapies. An increasing number of immunotherapies that target other immunogenic routes are under pre-clinical and clinical investigation, with one such option being *in situ* cancer vaccination. This is an approach where the therapy is directly injected into the site of the tumor causing rapid cancer cell death and subsequent processing and presentation of the released tumor-associated antigens (TAAs) thereby generating an adaptive immune response and eliciting systemic anti-tumor memory responses.[104]

The cowpea mosaic virus (CPMV) has demonstrated potent efficacy as an *in situ* vaccine.[109,135–137] The multivalent capsid and endogenous RNA activate the innate immune system through activation of toll-like receptors, a class of pattern recognition receptors (PRRs).[138] The potency and versatility of CPMV are quite impressive, however, repeated administration via injection poses a potential risk to the efficacy of the treatment. For example, three weekly injections for melanoma and six weekly injections for ovarian cancer,[139,140] Skin reactions (including pain, swelling, and soreness) are common side effects related to intravenous injections,[41] and could reduce patient compliance. Limited accessibility to healthcare facilities caused by unexpected circumstances, such as COVID-19 lockdowns, may influence the treatment scheduling. Therefore, there is the need for a single dose sustained release immunotherapy implant.

An increasingly common method to fabricate implantable devices is hot melt extrusion (HME). HME was first invented by Joseph Brama at the end of the eighteenth century for use in lead pipe manufacturing. Owing to the advantage of high-throughput processing and the solvent-free method limiting solvent-induced toxicity, HME was introduced in pharmaceutical formulations in the early 1970s. Since then, a list of small molecule drug delivery devices have been developed with HME.[141] Recently, protein therapeutics delivery implants manufactured by HME have been reported[142–144], showing the great potential of HME in developing sustained protein therapeutics delivery. Here, we sought to investigate the potential of HME in developing a CPMV single dose sustained release immunotherapy. However, we found the infeasibility of HME in manufacturing CPMV sustained release immunotherapy due to the breakdown of the CPMV viral capsid and extensive aggregation.

In an alternative approach, we sought to develop a combination therapy, in which a small molecule immunomodulator was incorporated into an implant and CPMV was injected in solution. The primary advantage of the implantable device would be a sustained dose of small molecule in the tumor that would not be susceptible to wash out effects. The small molecule we chose is an agonist of the stimulator of interferon genes (STING) transmembrane protein and produces pro-inflammatory cytokines, such as type I interferons (IFNs), leading to the propagation of innate immune sensing.[145] Diamidobenzimidazole (diABZI) has been designed as a non-cyclic dinucleotide STING agonist and have shown astonishing efficacy in the suppression of a murine CT-26 colon cancer model.[146] Therefore, we planned to use the water-soluble diABZI STING Agonist-1 (hydrochloride) (diABZI will be used as the abbreviation in the following paragraphs) as a vaccine adjuvant to strengthen the cytotoxicity of injected CPMV. We used HME to encapsulate diABZi and report a single dose sustained diABZI release delivery vehicle, aimed at

providing constant diABZI treatment to offset the rapid clearance of the STING agonist.[147] We also incorporated CPMV weekly injection to strengthen the potency of the combination treatment.

3.2 Results and discussion

3.2.1 CPMV sustained release immunotherapy device fabricated by HME

Polymer substrate, active pharmaceutical ingredients (APIs) and plasticizer are the common composition in HME-fabricated sustained delivery devices. Here, we chose poly(lactic-co-glycolic acid) (PLGA) as the polymer substrate due to its great biocompatibility and desired biodegradable profile. The incorporated drug is release during the degradation of the PLGA substrate and is typically controlled based on the degradation rate. Compared to non-degradable implant, the PLGA-based degradable implant does not require extra surgery to remove the device.[148] PLGA 50:50 was used here because it owns the fastest degradation profile in about one months.[143,149] To accelerate the release profile of the implant as well as increase the processability of the composites, PEG was added as plasticizer in the system. As for APIs, purified CPMV was lyophilized to a white powder.

A table-top vortex mixer was used to homogeneously mix the powdered materials, then the blends were loaded into a pilot extruder,[150] incubated at 70 °C for 90s, and extruded at ~8 psi stretch-guided by a tweezer. In the study, a 600 μm nozzle was chosen to realize the non-invasive surgery procedure while maintaining the ease of processability of the implant. The fabricated implant owns a diameter of 588.22 ± 93.61 μm, which can fit into an 18-gauge needle with an inner diameter at 838 μm and enables a non-invasive surgical procedure (Figure 3.1). Energy di spersive X-ray spectroscopy coupled with scanning electron microscopy (EDS-SEM) was performed to explore the dispersion of CPMV within the polymer substrate (presented with oxygen

signal emission), and the homogeneously dispersed sulfur signal (S K series) from the EDS spectrum suggest the even dispersion of CPMV in the implant (Figure S3.1).

Die swelling happened in the process. It is a common phenomenon found in thermoplastic HME process that the polymer entangled chains experience shear-induced elongation when entering the

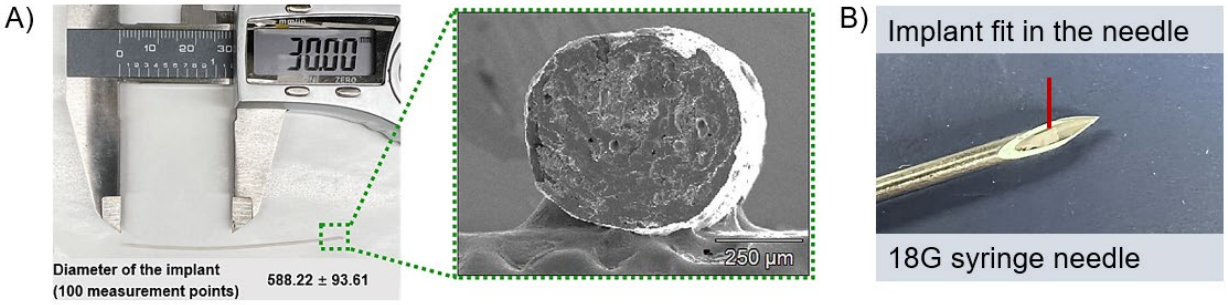

Figure 3.1 Illustration of the single dose sustained release immunotherapy fabricated by HME. A) Picture of the HME fabricated implant and cross-section structure of the implant characterized by SEM. The diameter of the implant was analyzed by ImageJ with a side-view implant SEM pictures. B) Implant extruded from 600 µm nozzle can fit in the needle.

die, and relax in elastic deformation by reentanglement and recoiling when exiting the die.[151] Therefore, stretch-guided extrusion provides axial extra force to further stretch the polymer chain to compromise die swelling,[152] though over- stretching could happen and resulted in recoiled defects and eventually break the extruded filament. (Figure 3.2)

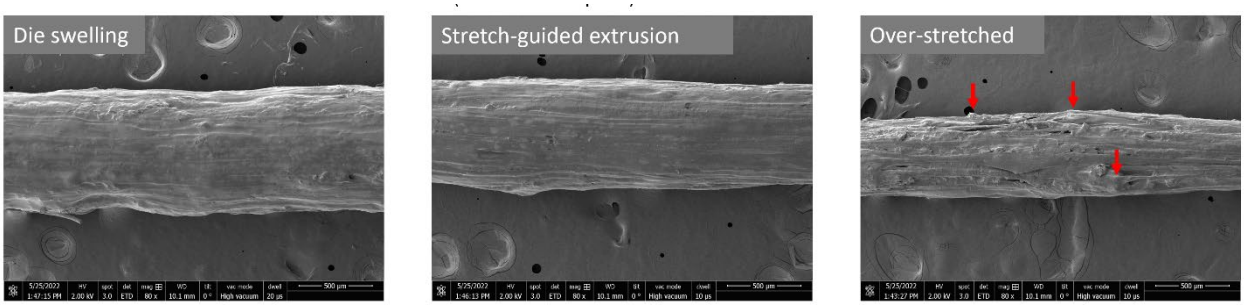

Figure 3.2 Die swelling phenomenon and stretch-guided extrusion observed by SEM. Red arrow pointed at recoiled defects.

3.2.1.1 Integrity of the recovered CPMV particles

To examine the integrity of the recovered CPMV particles from the implant, we performed an *in vitro* release study. To mimic the tumor microenvironment *in vivo*,[153] we used 10 mM PBS pH 6.8 as the *in vitro* release study buffer medium, and added slight agitation (150 rpm with an orbital shaker) to the *in vitro* release system. The released sample was taken out at different time points and replaced with the same amount of fresh buffer. Then, we mixed the released samples from different time points and performed a series of standard protein structural characterizations.

Wild-type CPMV has a single elution peak at 11 mL indicated by FPLC, while lyoCPMV and relCPMV display another peak at ~16mL. LyoCPMV and relCPMV also have an aggregated peak at ~9mL. Past studies have observed genomic RNA ejection from CPMV caused by lyophilization,[154] which may impact the elution of the CPMV. At 21 mL elution volume, we observed a rise for lyoCPMV and a peak for relCPMV, and this peak should belong to ejected genomic RNA. The ejection of the genomic RNA was further proven by the high ratio of UV

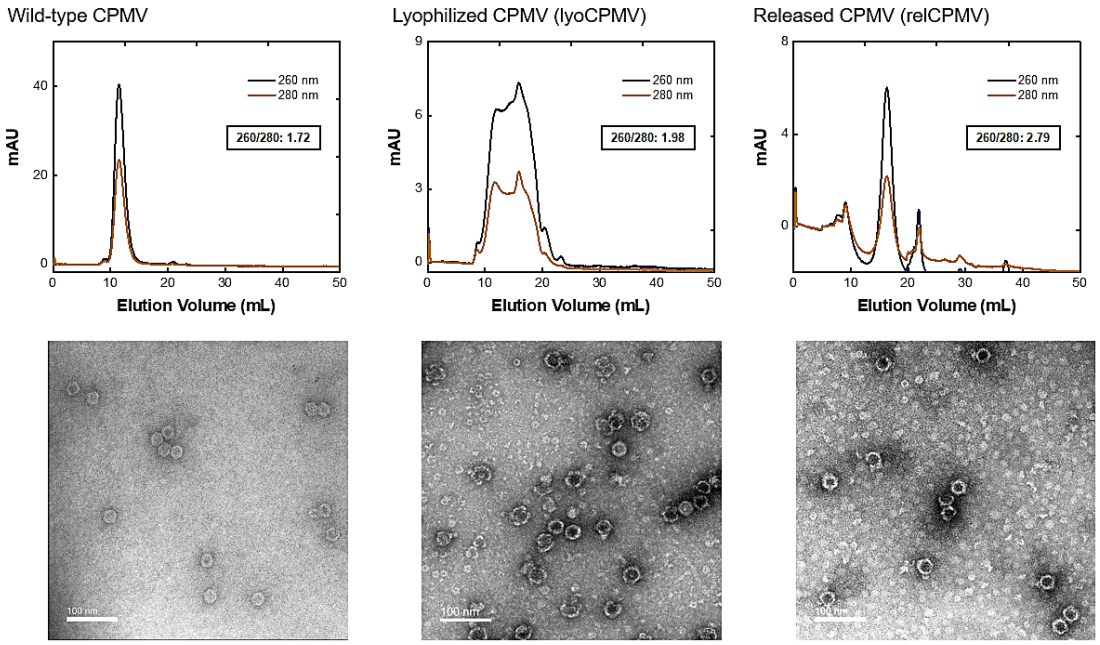

Figure 3.3 Characterizations of particle integrity. Up: Fast protein liquid chromatography (FPLC). Down: TEM images of the particles.

absorbance at 260nm and 280 nm (>2.0), indicating a high concentration of nucleic acid （Figure 3.3 Up）. Agarose gel electrophoresis (Figure S3.2) supported the ejection of genomic RNA caused by lyophilization and the integrity of the processed particles.

The structural integrity of the particles was examined by TEM. As expected, CPMV particles show dark interiors, indicative of the presence of encapsulated RNA. In contrast, lyoCPMV and relCPMV have lighter interiors and appear to be empty (Figure 2.3 Down). Dynamic light scattering (DLS) was performed to detect the sizes of the lyoCPMV and relCPMV, and they were in range with the size of native CPMV, and relCPMV has some aggregates at 100 nm (Figure 3.4).

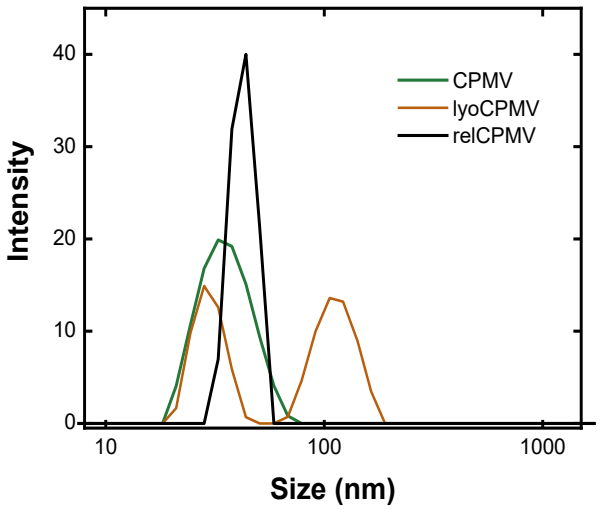

	Z-Average (d.nm)	PDI
CPMV	35.26	0.103
lyoCPMV	49.96	0.289
relCPMV	39.63	0.221

Figure 3.4 DLS confirms that particles are intact and of appropriate size. Slightly larger sizes are observed for lyoCPMV and relCPMV compared to CPMV.

3.2.1.2 *In vitro* release profile and formulation design

After the validation and analysis of the integrity of the processed particles, PEG plasticizer in different percentage and molecular weight were investigated to vary CPMV release profile *in vitro.* PEG was added in the formulation to lower the processing temperature and act as porogen for PLGA materials to accelerate release.[155] We first used PEG8K because it has been frequently reported in sustained protein delivery implant fabricated by HME.[143,144] To modify the release profile of the implant, we fixed the percentage of PEG 8K at 15%, and hypothesized that a faster release profile will associate with higher percentage of CPMV. As shown in Figure 3.5 A), linear release profiles were observed for three different formulations and 70%PLGA/ 15% PEG8K/ 15% CPMV shows the fastest initial burst release, however, 80%PLGA/ 15% PEG8K/ 15% CPMV reaches the highest equilibrium release (Figure 3.5). The low equilibrium release may be caused

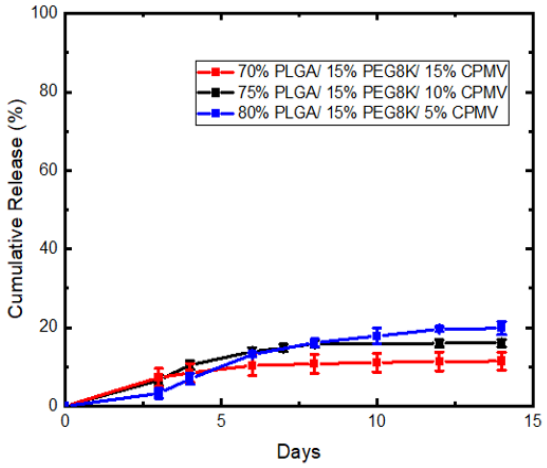

Figure 3.5 *In vitro* release profile of CPMV implant. PEG8K was fixed at 15%, and the percentage of CPMV was modified to achieve varied releasing profile.

by the aggregation of the particles. We further chose PEG 3350 to limit the PEG precipitation. What's more, the melting temperature of PEG 3350 is at the range of 53° C - 57° C,[159] while PEG 8000 is at the range of 55° C - 62° C,[160] leading to easier processability for the PEG3350

formulation than the PEG8000 formulation when at same processing temperature. We also found CPMV was unstable in PBS, but stable in KPB (Figure S3.3 and S3.4). Therefore, we switched to 10mM KPB as the release medium, however unfortunately, we observed little improvement for the equilibrium release of CPMV and less controllable release profile (Figure S3.5).

Compared to Qβ, a previously studied HME processable protein for drug delivery implants, CPMV is more fragile to external conditions, therefore, some part of the precipitated CPMV may experience aggregation and cause the low equilibrium release. To verify this hypothesis, organic extraction was used to dissolve the left implant after 30 days of *in vitro* release and the incorporated and unreleased CPMV was extracted.[144] The extracted sample was then resuspended in 10mM KPB overnight at 4° C, and SDS-PAGE electrophoresis was performed to analyze the integrity of the coat proteins of the resuspended CPMV. The bands at 42 kDa and 24kDa suggested intact CPMV subunits, however, the strong signal found in the well suggested CPMV aggregates, and the smeared band at below 17kDa suggested impurities and broken protein subunits (Figure S3.6). Therefore, CPMV may not suit HME fabricated sustained release immunotherapy.

3.2.2 diABZI sustained release immunotherapy device fabricated by HME

Due to the infeasibility of CPMV delivery implant fabricated by HME, we pivoted to an HME diABZI sustained release device. The implant aims to increase the efficacy of the immunotherapy by providing continuous diABZI treatment as opposed to the fast clearance of the STING agonist. CPMV was also administered weekly to supplement the diABZI implant treatment.

As mentioned beforehand, PEG3350 has a lower melting point and serves as a better plasticizer for HME compared to PEG8K, thus we fixed PEG3350 as the plasticizer for the diABZI delivery implant. 70%PLGA5050/ 20% PEG3350/ 10% diABZI was formulated to achieve the desired processability and release profile while maintaining the integrity of the implant when PEG3350

dissolves. A similar HME processing procedure was performed; the composites were incubated in the pilot extruder for 90s at 70° C, and stretched-guided extruded at ~ 8psi.

3.2.2.1 Qualitative and quantitative analysis of the released diABZI from the implant

~ 3 mg of implant was submerged in 10 mM PBS (pH 6.8) and incubated in an orbital shaker at 37° C with mild agitation at 150 rpm. Released samples were extracted at different times, and HPLC was performed to analyze the samples both qualitatively and quantitatively. For qualitative analysis, released samples collected at different times were mixed and concentrated, then we performed HPLC and collected the major peak that eluted with a maximum absorbance at 322 nm, the distinctive maximum absorbance of diABZI. LC-MS was followed to measure the mass of the concentrated eluted major peak. The peak mass of the sample was determined at 852.41Da, which aligned with the molecular weight of diABZI without the three hydrochloride molecules (Figure S3.7). For quantitative analysis, HPLC was carried out to first calibrate a standard curve with for diABZI samples with known concentrations, then the diABZI amount of the released samples was calculated based on the calibration curve. Linear release of the implant was observed over a two-month time period (Figure S3.8 and Figure 3.6).

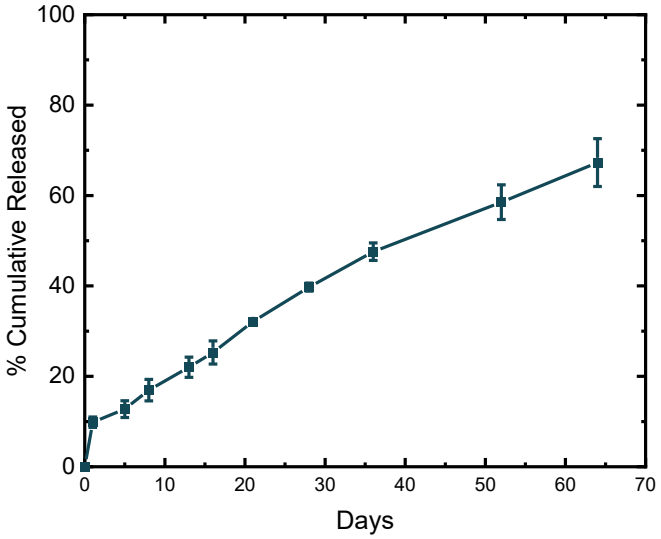

Figure 3.6 *In vitro* release profile of diABZI implant with the formulation of 70%PLGA5050/ 20% PEG 3350/ 10% diABZI.

3.2.2.2 diABZI pilot weekly injection treatment *in vivo*

Once the qualitative and quantitative analyses of the released diABZI from the implant were determined, we moved forward with *in vivo* murine models to test the efficacy of the implant treatment. For the treatment groups, we utilized diABZI and CPMV monotherapies, as well as combination (combo) therapy of diABZI and CPMV. We hypothesized that the combination of CPMV and diABZI would produce synergistic efficacy due to the activation of multiple immunostimulatory pathways – CPMV activates TLRs 2, 4, and 7 while diABZI activates STING. Before the implant study, we designed a pilot study to determine the appropriate dosage of diABZI in multiple tumor models. While diABZi has demonstrated potent efficacy in the CT26 model, it has not been studied in the B16F10 melanoma model. Additionally, diABZI is mainly administered intraperitoneally (IP) and not intratumorally (IT) as was done in our studies. We compared the

efficacy of diABZI at 5 and 10 μg using B16F10 melanoma intradermal (ID), CT26 IP, and CT26 subcutaneous (SC) models.

3.2.2.3 B16F10 melanoma intratumoral IT treatment

All animal studies were carried out in compliance with the guidelines set out by the Institutional Animal Care and Use Committee of UC San Diego. 6-7 week old C57BL/6J female mice were inoculated with 200,000 B16F10 melanoma cells ID. Treatments were started once the tumor reached 40 mm^3, and administered three times IT weekly. The different treatment groups were PBS, 5 μg diABZI, 10 μg diABZI, 100 μg CPMV, 100 μg CPMV + 5 μg diABZI, and 100 μg CPMV + 10 μg diABZI. The CPMV and diABZI combination treatments demonstrated significant cytotoxicity and achieved significant tumor growth delay compared to PBS (Figure 3.7). The mean survival of the CPMV + 5 μg diABZI and the CPMV + 10 μg diABZI improved from 19 days (PBS) to 31 and 41 days, respectively. At day 19 following tumor injection, the average tumor volume for the combination groups were 146.5 and 67.75 mm^3, respectively, compared to 1682 mm^3 for the PBS group. In contrast, the monotherapy treatments of CPMV and 5 μg diABZI were ineffective and did not increase the mean survival compared to PBS although tumor growth was inhibited slightly (Figure 3.7). However, increasing the dose of diABZI to 10 μg improved the efficacy significantly, and adding CPMV did not improve outcomes compared to the monotherapy. While somewhat puzzling, this could be explained by the fact that CPMV causes the production of type I IFN similarly to diABZI.[161] While the pathways to produce IFN are different between CPMV and diABZI, the overlapping cytokine production may be the reason for the lack of synergy. Even so, we did establish synergistic efficacy at the lower dose of 5 μg diABZI, which is the dose that was chosen for the future implant studies (see Section 3.2.3).

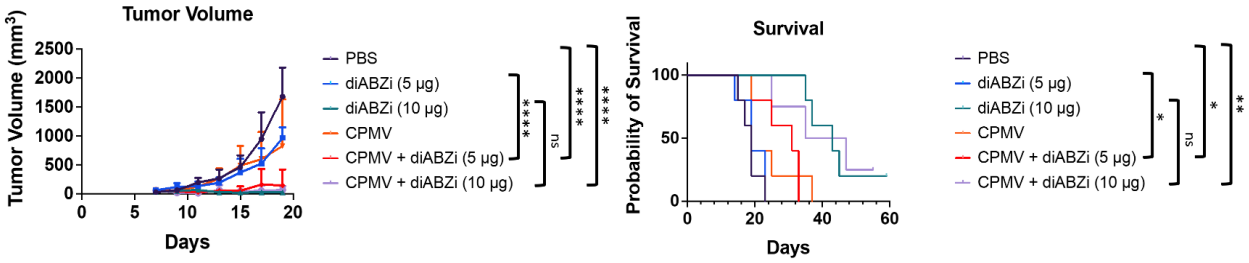

Figure 3.7 IT injection of the treatments in the B16F10 melanoma model. Tumor growth curves show mean tumor volume with the error bars representing the standard deviation. All experiments were accomplished with n = 5, and significance was deemed as $p < 0.05$. The tumor volume curve was analyzed with two-way ANOVA while the survival curve was analyzed using a Mantel-Cox test. * = $p < 0.05$, ** = $p < 0.01$, *** = $p < 0.001$, **** = $p < 0.0001$, ns = not significant.

3.2.2.4 CT26 colon cancer subcutaneous (SQ) and intraperitoneal (IP) treatments

We further investigated the combination treatments in a CT26 colon cancer model, both SQ and IP. For CT26 SQ treatment, BALB/C female mice were inoculated with 200,000 CT26 cells SC. Similarly with the B16F10, treatments were started once the tumor reached 40 mm^3, and administered three times IT weekly. The treatment groups remained the same, however, there was little difference between the treatment groups (Figure S3.9). While the PBS mice survived an average of 25 days, the 5 µg diABZI, CPMV, CPMV + 5 µg diABZI, and CPMV + 10 µg diABZI mice survived on average 37, 41, 45, and 39 days, respectively. In the 10 µg diABZI group, the average was undetermined as 3/5 mice survived the treatment. While all groups outside of the CPMV monotherapy elongated survival significantly compared to the PBS control, there were no significant differences between any of the other treatments. The lack of difference between the combination and the monotherapy groups may again be indicative of the IFN production by both CPMV and diABZI.

With the CT26 IP model, the BALB/C female mice were inoculated with 500,000 CT26 cells IP and were treated as before with 3x injections IP starting one week post tumor inoculation. The mice weight and body circumference were measured every 2 days as an indicator of ascites development and tumor growth. Similarly as with the SQ treatment, there were no significant differences between the treatment groups although all treatments other than the CPMV monotherapy extended survival and delayed tumor growth compared to PBS (Figure S3.10). For instance, by day 21, the mice circumference had increased by 44.2% in the PBS mice compared to 9.2, 12.9, 28.7, 7.8, and 14.7% for the 5 μg diABZI, 10 μg diABZI, CPMV, CPMV + 5 μg diABZI, and CPMV + 10 μg diABZI groups, respectively.

3.2.3 diABZI implant efficacy study *in vivo*

Guided by the initial pilot studies, we chose the B16F10 ID model and 5 μg diABZI as the dosage to investigate the efficacy of the implant. For the implant groups, implants incorporating 15 μg diABZI were used to dose match the 3x 5 μg IT injections – we additionally added a single-time 5 μg diABZI booster injected concomitantly with the implant to offset the delayed released of diABZI from the implant. A treatment group consisting of a single-time bolus injection of 20 μg of diABZI was also investigated. Lastly, we added a treatment group where the CPMV and diABZI were injected peri-tumorally to compare the difference between peri-tumoral administration and IT administration, as the implants were injected peri-tumorally. Therefore, the treatment groups were as follows: PBS, 5 μg diABZI (3x weekly), 20 μg diABZI (single bolus injection), 100 μg CPMV (3x weekly), 100 μg CPMV + 5 μg diABZI IT (3x weekly), 100 μg CPMV + 5 μg diABZI peri-tumorally (3x weekly), 100 μg CPMV (3x weekly) + 5 μg diABZI (single injection) + 15 μg diABZI implant, 5 μg diABZI (single injection) + 15 μg diABZI implant, and a plain implant consisting of 75% PLGA and 25% PEG3350 with no diABZI.

Mice were injected with the treatments one week post tumor inoculation, tumor volume was measured every 2 days, and mice were sacrificed at an endpoint volume of 1500 mm^3. Comparing 5 μg diABZI to the 5 μg diABZI + diABZI implant, we did not notice any significant differences in the tumor volume with no tumors developing in the monotherapy group and one mouse developing tumors in the implant group. Adding CPMV to the treatment did not diminish the effectiveness but could not improve upon the treatment as the diABZI monotherapy, which caused complete tumor regression up to day 35. Similarly, adding CPMV to the treatment regimen did not improve efficacy significantly although 5/5 mice remained disease free 35 days post tumor

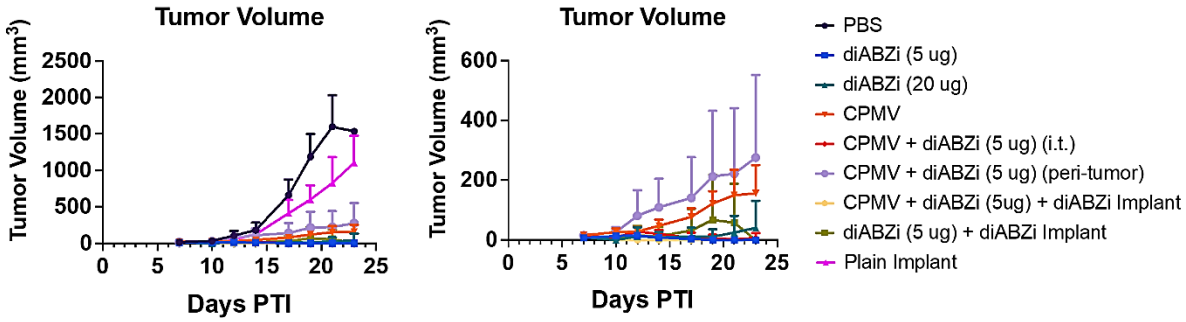

Figure 3.8 Implants and weekly injection treatments with B16F10 melanoma model. Tumor growth curves shown as a relative tumor volume. Right figure has a modified y-scale without the control groups of PBS and plain implant.

inoculation. The results with the 5 μg diABZI weekly treatment were considerably different from our initial B16F10 pilot study in which at the 5 μg dose, the tumors began to develop starting at day 9. This may be due to the difference in the injection schedule. In the pilot study, tumors were injected at a minimum volume of 40 mm^3 (~7-10 days), but with the implant studies, we injected all mice one week post tumor inoculation. Future studies could examine whether waiting for the tumors to develop further would help to delineate the therapeutic outcomes between treatment groups and additionally provide data on whether the implant is effective at larger tumor sizes, which may be more clinically representative. Regardless, the implants were comparable in

efficacy with the 3x weekly injected monotherapy and reducing the number of hospital visits with a single-dose injection could increase patient compliance within the clinic.

Additionally, the single bolus injection of 20 μg of diABZI led to delayed, but significant tumor growth in 4/5 mice at day 35 post tumor inoculation (Figure 3.9). The bolus injection led to an average tumor volume of 221.3 mm^3 at day 35 while the implant mice had an average tumor volume of 22.78 mm^3 ($p < 0.05$). This demonstrates that compared to a single injection of a larger dose, the implants lead to longer lasting tumor protection most likely due to the extended diABZI release profile afforded by the implant. It is also important to note that the implants were not injected IT, but peri-tumorally, which means that a proportion of the released diABZI may not travel into the tumor leading to a lower delivered dose. This was evidenced by the lack of efficacy

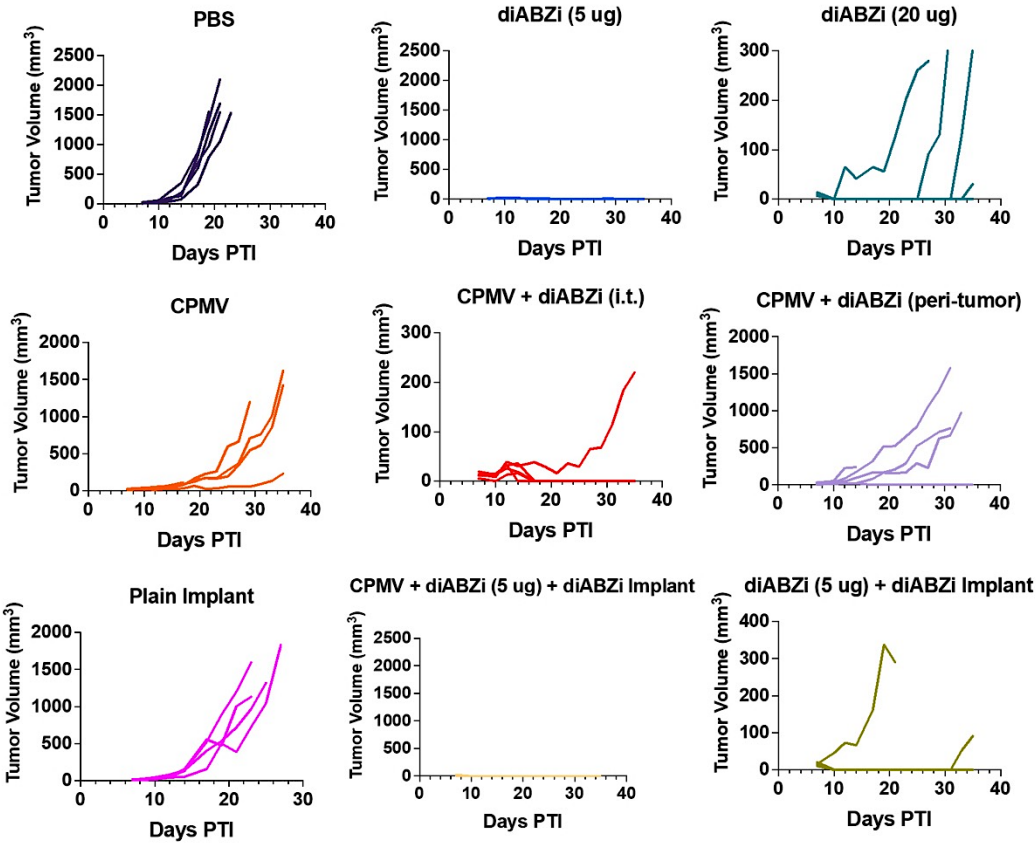

Figure 3.9 Tumor growth curves for the individual groups. Each line represents one mouse, and each group had n = 5. Lines that are not visible are because the tumor volume is 0 mm^3 and is on top of the x-axis.

in the CPMV + diABZI peri-tumor group. While the CPMV + diABZI IT and CPMV + diABZI implant groups demonstrated an average tumor volume of 23.14 and 0 mm^3, respectively, the CPMV + diABZI peri-tumor group had an average tumor volume of 750.5 mm^3 at day 31 post tumor inoculation. This led to a 20% survival at day 35 for the peri-tumor group and 100% survival in the other two groups. Therefore, it is surprising and impressive that even with the peri-tumoral implant injection, the treatment efficacy is able to match the efficacy afforded by the direct IT injections. Finally, the plain implant extended survival only 2 days compared to PBS, showcasing that the implant itself imparts no immunogenic function (Figure 3.9).

For future studies, we may need to redo the study waiting for the cancers to develop to > 40 mm^3 instead of injecting at a specific time point. With the current ongoing study, we plan to re-challenge the survivors using age-matched mice injected with PBS as an additional control group. This study would delineate whether the implant imparts an improved immune memory response compared to the weekly injections leading to better overall survival following re-challenge. Additionally, flow cytometry and cytokine ELISAs can be carried out to investigate the differences in cell activation/recruitment and release of inflammatory cytokines. Most notably, the expression of the type I IFNs should be investigated in a longitudinal manner to demonstrate that the implant leads to extended production of IFNs.

3.3 Experimental section

3.3.1 Materials and cell culture

Ultrapure water (Milli-Q, Bedford, MA) was used for all experiments. PLGA (Akina, AP041, 50:50 LG Ratio, MW 10-15 kDa) was ground in a mechanical blender (Magic Bullet™, Amazon #B012T634SM) and passed through a 45 mesh screen (Sigma, Z675415) prior to injection and/or processing. Polyethylene glycol 8K, monosodium phosphate anhydrate, disodium phosphate heptahydrate, dimethyl sulfoxide were purcharsed from Fisher Scientific. PEG 3350 was

purchased from Sigma-Aldrich. PBS 1x (pH=7.4) was purchased from gibco. DiABZI STING agonist -1 (trihydrochloride) was purchased from MedChemExpress (MCE). CPMV Production and Purification: Black-eyed peas (Vigna unguiculata) were inoculated with 100 ng/μL CPMV in 0.1 M potassium phosphate buffer (pH 7.0) and propagated for 18–20 days using established procedures.[129] Briefly, infected leaves were homogenized in a commercial blender in 0.1 M potassium phosphate buffer, pH 7.0. The homogenized mixture was clarified by centrifugation (15 000g, 20 min), followed by a 1:1 chloroform/n-butanol extraction to remove hydrophobic debris. The aqueous layer was precipitated using PEG6000 (4% w/v) and NaCl (0.2M), and the pellet was collected by centrifugation. The resulting pellet was resuspended in 0.1 M potassium phosphate buffer and purified using a 10–40% sucrose density gradient.

The B16F10 and CT26 cell lines were both purchased from ATCC. B16F10 was grown in DMEM supplemented with 10% (v/v) FBS and 1% (v/v) penicillin/streptomycin (P/S). CT26 was grown in RPMI-1640 supplemented with 10% (v/v) FBS and 1% (v/v) P/S. The cells were passaged once confluency reached > 80%, and they were maintained at 37°C and 5% CO_2.

3.3.2 Instrumentation and Equipment

HME was performed with a homemade pilot-scale extruder.[150] Scanning electron microscopy (SEM) images were collected with an FEI Quanta FEG 250 while energy-dispersive spectroscopy (EDS) data of oxygen and sulfur were collected by FEI Quanta FEG 250 as well. A freezone 2.5L freeze-dryer (Laboconco, Kansas, MO, USA) was used for lyophilization. A Zetasizer Nano ZSP/Zen5600 (Malvern Panalytical) was used to perform DLS. The particles were run at 25 °C with 3 measurements per sample. FPLC was performed by running the samples through a Superose 6 size-exclusion column (column dimensions of 10 × 300 mm with an exclusion limit of 4 × 107 Mr) at 0.5 mL min−1 for a total volume of 50 mL in an ÄKTA Explorer FPLC machine (GE

Healthcare LifeSciences). The elution profile was isocratic, and the UV detectors were fixed at 260 (nucleic acid) and 280 nm (protein). FEI Tecnai Spirit G2 BioTWIN was performed to collect TEM images. The samples were loaded onto Formvar carbon film coated TEM supports with 400-mesh hexagonal copper grids (VWR International) at concentrations ~0.5 mg mL−1 in DI H2O for 2 min. The grids were washed with DI H2O twice for 45 s and then stained with 2% uranyl acetate (Agar Scientific) for 30 s twice. The samples were imaged at 300 kV. For agarose gel electrophoresis sample preparation, 10 uL ~1 mg/mL CPMV was mixed with 2 uL 6x Gel Loading Purple dye (Biolabs) and 10uL mixed sample was loaded onto a 0.8% (w/v) agarose gel. The agarose gel was stained with 1 μL of GelRed nucleic acid gel stain (Gold Biotechnologies) and run for 30 min at 120 V and 400 mA. Immediately after the run, the gel was imaged using the AlphaImager system (Protein Simple) under UV light and then imaged again after staining with 0.25% (wt/vol) Coomassie Blue.

3.3.3 HME fabrication of sustained release devices

PLGA, PEG and CPMV/ diABZI were weighted by digital scale and put in a 0.6 mL Eppendorf tube. Then the composite was vigorously mixed by a vortex mixer (Fisher Scientific) at level 10 for 5 min. Then the mixed composite was loaded into the barrel of the pilot extruder through a homemade 3D-printed feeder. The loaded composite was then incubated at 70°C for 90s, followed by extrusion at ~8 psi. CPMV was desalted by six-time DI water wash with a 4mL centrifugal filter (100k, EMD Millipore) and the concentration was modified to ~1 mg/mL, followed by freezing in liquid nitrogen for 10 min and lyophilized for 3 days until complete water sublimation.

3.3.4 *in vitro* releasing (CPMV) quantification

~ 7mg CPMV implant sample was put in a 0.6mL Eppendorf tube and filled with 400uL releasing medium. 5 min 10,000rpm centrifugation was performed each time to extract supernatant release

sample, and 200 uL sample was taken out and refill with fresh releasing medium. Pierce BCA Protein Assay Kit (Thermo Fisher Scientific) was used to quantify the concentration of the samples.

3.3.5 Organic extraction of CPMV and denaturation analyzed by SDS-PAGE

The sample was centrifugated for 10 min at 10k rpm, and the aqueous supernatant was pipetted put. 2 mL ethyl acetate was added and incubated for 15 min, R.T., followed by 5 min 10K rpm centrifugation, and the organic solvent supernatant was pipetted out. This organic extraction step was repeated for two more times, and the residue pellet remained as extracted CPMV. Then 500 uL KPB was added to resuspend the pellet overnight with mild agitation at 4° C. In the following day, the mixture was taken out and the samples were prepared with Novex LDS Sample Buffer (4X) and denatured at 95° C for 5min, and loaded onto a GenScript ExpressPlus PAGE gels 4%–12% bis-tris protein gels (1.0 mm × 12 wells) (35 min, 140 V, 20× MES SDS running buffer). The gels were first destained in a mixture of deionized (DI) water, methanol, and acetic acid (50:40:10; v/v) for 30 min followed by staining in 0.25% (wt/vol) Coommassie Blue solution for 30 min before imaging with the AlphaImager system (Protein Simple).

3.3.6 *in vitro* releasing (diABZI) quantitative and qualitative analysis

The standard diABZI samples were weight by an ultra-high resolution digital scale(NewClassic MS, Mettler Toledo) and mixed with milli-Q water. Then the sample was run by HPLC with the method profile of 78% -85% ACN/H_2O, 0.5mL/min, 15min. The peak at 322nm absorbance was collected, and the area of the peak was analyzed by OriginLab. Then OriginLab was used to draw the calibration standard curve and served for the calculation of the releasing samples.

~ 3mg diABZI implant sample was put in a 2 mL Eppendorf tube and filled with 1mL PBS (pH=6.8). 5 min 10,000rpm centrifugation was performed each time to extract supernatant release

sample, and 500 uL sample was taken out and refill with fresh PBS. Then the sample was injected into HPLC, and analyzed by the same HPLC method as mentioned above. The eluted peak was collected and analyzed qualitatively with LC-MS and quantitatively by OriginLab with the calibration standard curve.

3.3.7 CPMV and diABZI B16F10 Combination Treatment

All animal studies were in compliance with the guidelines set out by the Institutional Animal Care and Use Committee of UC San Diego. 6-7 week old C57BL/6J female mice were purchased from the Jackson Laboratory and used for the B16F10 treatment studies. The animals were provided food and water *ad libitum*, and were kept at the Moores Cancer Center at UC San Diego. The day before inoculation, the left flanks of the mice were shaved. The next day, the cells were collected and resuspended at 6.67 x 10^6 cells/mL in sterile PBS, and 30 μL was injected ID (200,000 cells/mouse). Treatments were started once the tumors reached 40 mm^3, and administered three times IT weekly. Tumor volume was calculated as length x $width^2/2$, and the animals were sacrificed when the tumor volume reached an endpoint value of 1500 mm^3. The treatment groups consisted of PBS, 5 μg diABZI, 10 μg diABZI, 100 μg CPMV, 5 μg diABZI + 100 μg CPMV, and 10 μg diABZI + 100 μg CPMV. Due to the limited solubility of diABZI in aqueous solutions, the groups with diABZI were injected in 5% (v/v) DMSO in DI water while the other groups were diluted in PBS. The mice were measured every 2 days for a total of 60 days.

3.3.8 CPMV and diABZI CT26 Combination Treatment

For the CT26 studies, 6-7 week old BALB/C mice were purchased from the Jackson Laboratory. Two CT26 models were tested, one IP and the other SQ. For the IP studies, CT26 cells were diluted in PBS at a concentration of 2.5 x 10^6 cells/mL, and mice were injected IP with 200 μL (500,000 cells/mouse). The mice circumference and weight were measured every two days starting from the

4th day post tumor inoculation. Mice were sacrificed when their body weight reached 30 g or > 75% of their original body weight or when their circumference reached > 60% of their original circumference. The mice were treated with the same treatment groups and with the same treatment schedule (3x weekly) as with the B16F10 combination study except the injections were administered IP. At day 40, all the mice that showed absence of tumor growth were re-challenged with 500,000 cells/mouse to demonstrate immune memory induced by the treatment. The mice were again measured every 2 days until clinical endpoints were reached, and survivors of the re-challenge were measured for an additional 40 days.

For the CT26 SQ studies, the CT26 cells were resuspended in PBS at a concentration of 2 x 10^6 cells/mL and mixed in a 1:1 ratio with Matrigel (Corning). 200 μL of the cell-Matrigel mix was injected SQ in the shaved left flank of the mice (200,000 cells/ms). The injection schedule and treatment groups remained the same as before except the treatments were injected IT. The mice were measured every 2 days, and the clinical endpoints were designated at a tumor volume of 1500 mm^3.

3.3.9 CPMV and diABZI Implant Studies

The efficacy of CPMV and diABZI were then additionally investigated in the B16F10 ID model using the slow release diABZI implants. Here, 6-7 week old C57BL/6J mice were shaved on their left flanks the day before the injection of 200,000 cells/mouse as before. The treatment groups consisted of PBS, 5 μg diABZI, 20 μg diABZI single bolus injection, 100 μg CPMV, 100 μg CPMV + 5 μg diABZI IT, 100 μg CPMV + 5 μg diABZI peri-tumorally, 100 μg CPMV + 5 μg diABZI (single injection) + 15 μg diABZI implant, 5 μg diABZI (single injection) + diABZI implant, and a plain implant with no diABZI. In the 20 μg diABZI group, a single injection was administered equal to the total amount of diABZI in the implant treatment groups. With the implant

groups, one 5 μg injection of diABZI was given initially to offset the initial slow release of diABZI from the implant. The peri-tumor CPMV + diABZI group was also tested to investigate the differences in treatment efficacy between IT and peri-tumor administration, as the implants could not be injected IT and were therefore injected peri-tumorally. CPMV was administered 3x weekly as before. The tumors were measured every 2 days until the clinical endpoint of 1500 mm^3.

3.3.10 Statistical Analysis

All statistical analyses were carried out on GraphPad Prism. For the tumor volume, circumference, and body weight graphs, the treatment groups were compared using two-way ANOVA. The survival curves were analyzed using a Mantel-Cox test. Statistical significance was deemed as a p value < 0.05. All treatment groups were carried out at $n = 4$-5, and the data points represent the mean while the error bars represent the standard deviation.

3.4 Conclusion

A single dose sustained release immunotherapy is in high demand. In this chapter, we reported such a delivery platform fabricated by HME, which can be easily transitioned to a high-throughput manufacturing scheme. We began by using CPMV as a sustained delivery implant, however, we were not able to move forward to animal studies due to the breakdown of the CPMV capsid and extensive aggregation, making it less suitable for HME. Instead, diABZI was formulated and fabricated into a sustained small molecule delivery implant, which showed great efficacy in suppressing B16F10 tumors, suggesting the potential of using HME to fabricate single dose sustained release immunotherapy implants. This research finding could serve as a guide to the future development of HME-mediated drug delivery systems, which not only increase the safety and efficacy of the treatment but also the quality of life of patients.

3.5 Supplemental figures

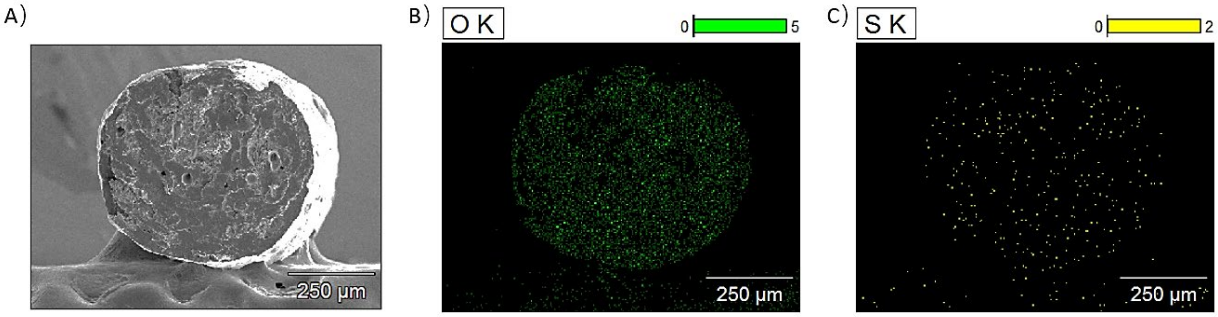

Figure S3.1 A) Full-scale SEM image of the cross-section of the implant. B) EDS spectrum oxygen K-series emission signal (O K series) map. C) EDS spectrum sulfur K-series emission signal (S K series) map.

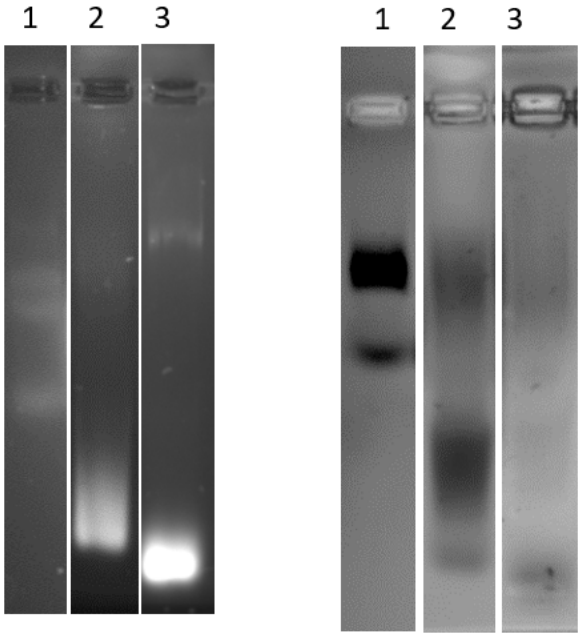

Figure S3.2 1% (w/v) Agarose gel stained with GelRed (left) and Coomassie brilliant blue (right). Lane 1 -3: wild-type CPMV, lyoCPMV and relCPMV.

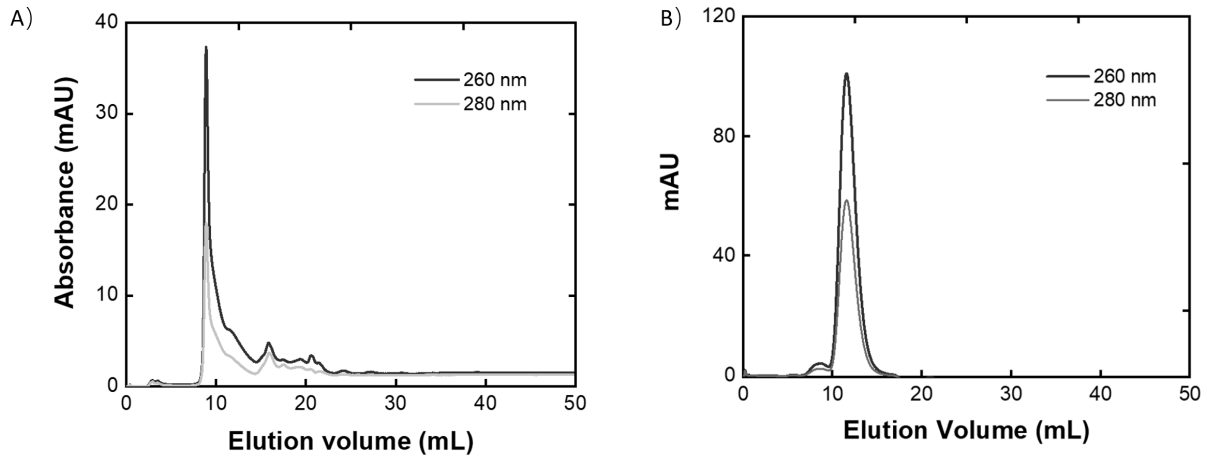

Figure S3.3 A) CPMV FPLC trace run with PBS buffer. B) CPMV FPLC trance run with KPB buffer.

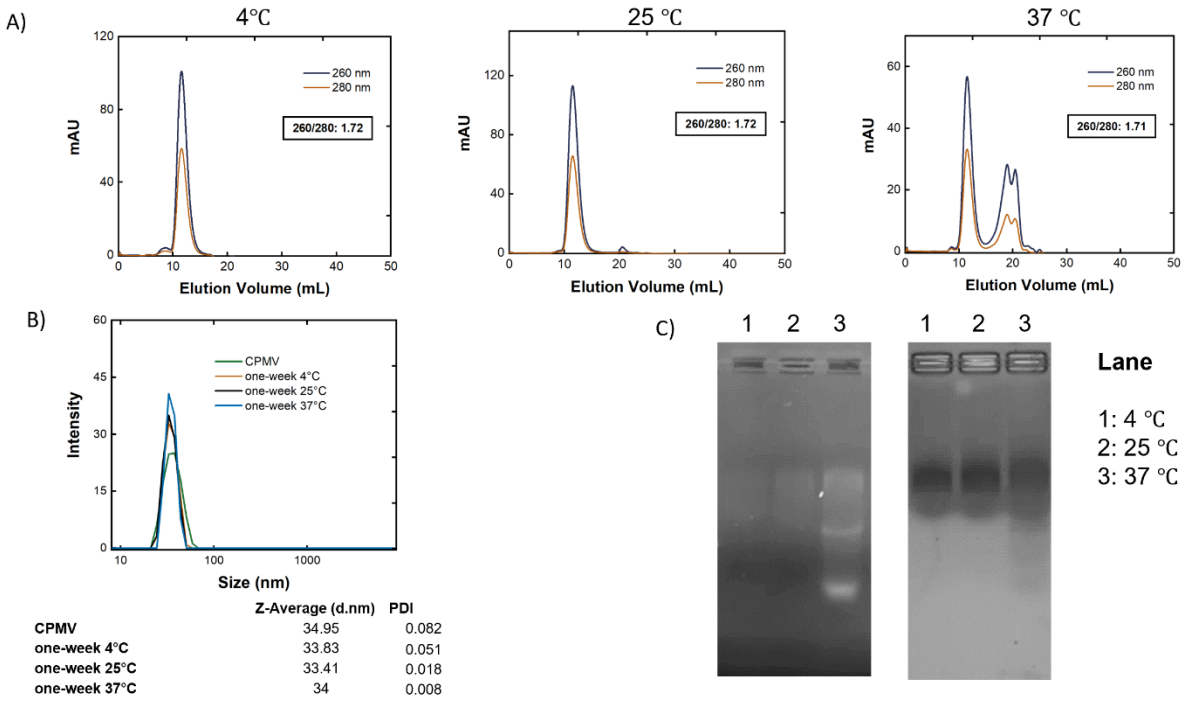

	Z-Average (d.nm)	PDI
CPMV	34.95	0.082
one-week 4°C	33.83	0.051
one-week 25°C	33.41	0.018
one-week 37°C	34	0.008

Figure S3.4 Stability of CPMV in KPB for one week incubated at 4°C, 25°C and 37°C. A) FPLC. B) DLS. C) Left: RelGel-stained agarose gel indicating the dispersion genomic RNA; right: Coomassie blue- stained agarose gel indicating the integrity of CPMV.

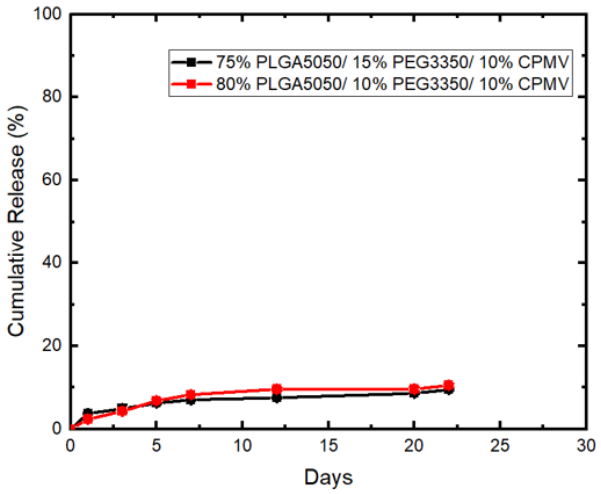

Figure S3.5 *In vitro* releasing profile. CPMV was fixed at 10%, and the percentage of PEG3350 was modified to achieve a varied releasing profile.

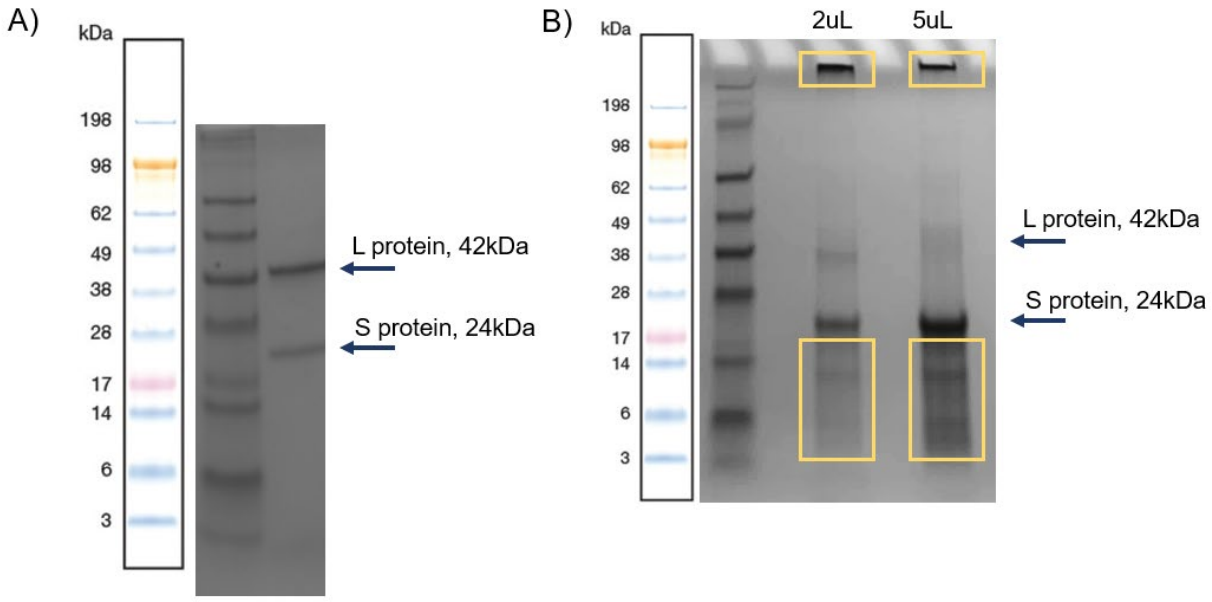

Figure S3.6 SDS-PAGE electrogenesis analysis. A) Wild-type CPMV. B) Resuspended organic extracted CPMV.

A)

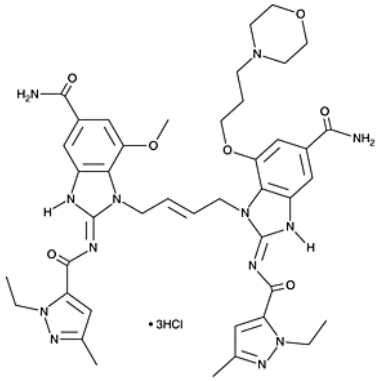

diABZI STING Agonist-1 (hydrochloride

Mw: 959.3 Da
Mw w/o 3HCl molecules: 852.95 Da

B)

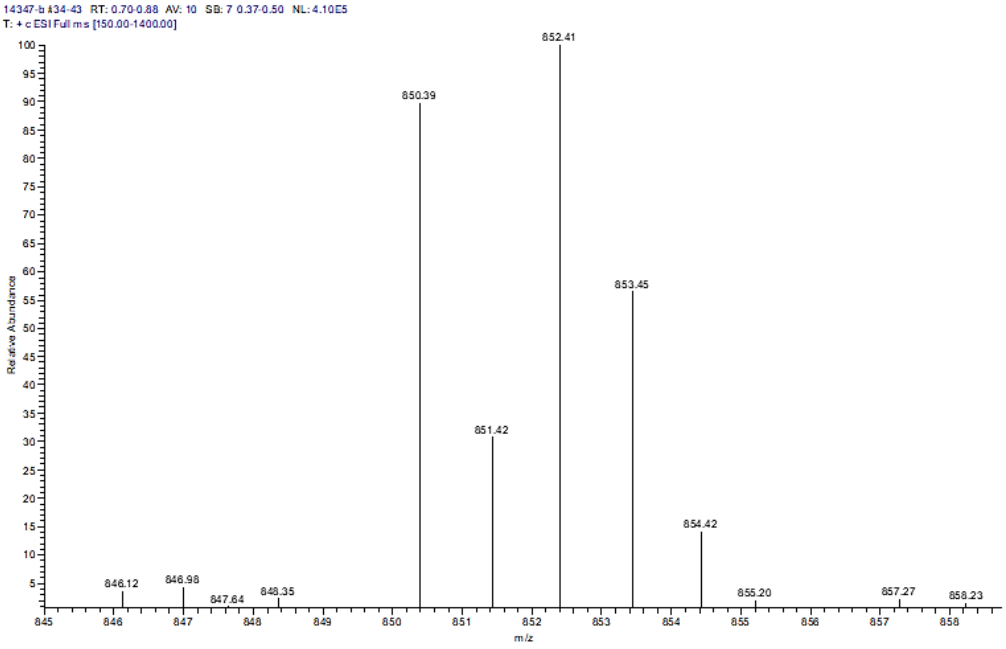

Figure S3.7 A) Molecular structure and molecular weight of diABZI STING Agonist (hydrochloride). B) LC-MS analysis result of the major peak eluted at 322nm.

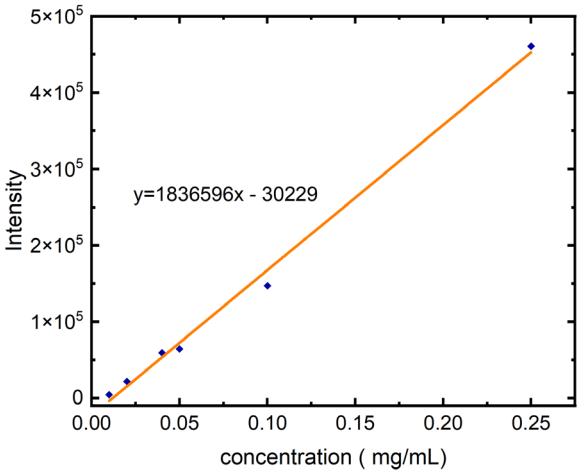

Figure S3.8 diABZI standard calculation curve was determined by standard diABZI samples with known concentrations

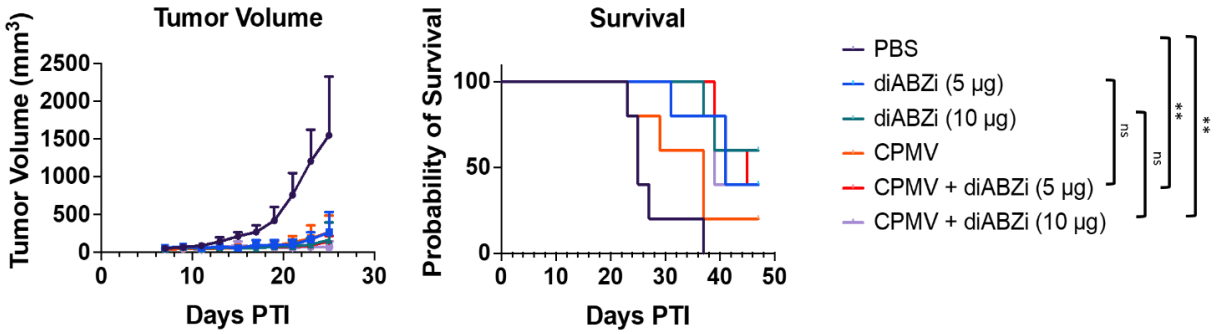

Figure S3.9 IT injection of the treatment with a CT26 SQ model. Tumor growth curves shown are the mean tumor volumes and error bars represent the standard deviation. All experiments were accomplished with n = 5, and significance was deemed as $p < 0.05$. The tumor volume curves were analyzed by two-wav ANOVA while the survival curve was analyzed using a Mantel-Cox test. * = $p < 0.05$, ** = $p< 0.01$, *** = $p < 0.001$, **** = $p < 0.0001$, ns = not significant.

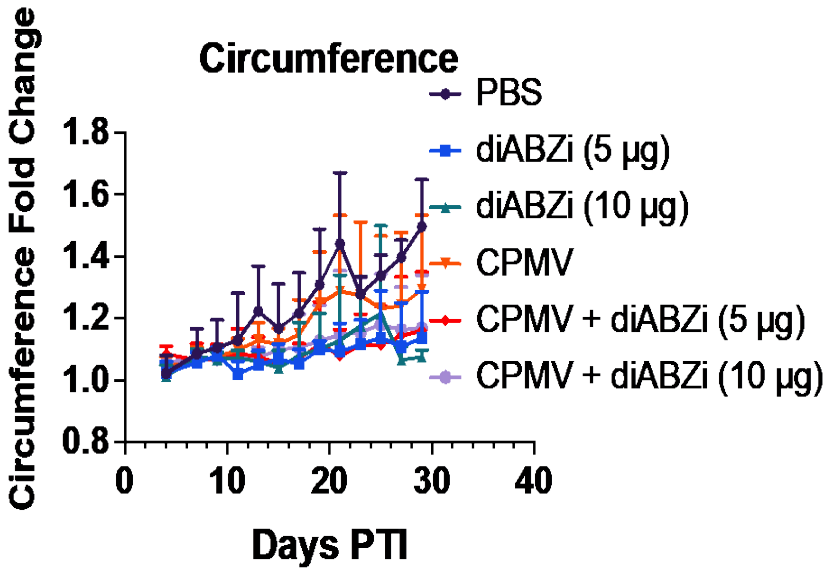

Figure S3.10 IP. injection of the treatment with a CT26 IP model. The graph is displaying the average fold change of the circumference compared to the original circumference of the mice before tumor inoculation. The error bars represent the standard deviation.

Acknowledgements

Chapter 3, in part, is a reprint of the material as it appears in "Hot melt extrusion: An emerging manufacturing method for slow and sustained protein delivery." Wiley Interdisciplinary Reviews: Nanomedicine and Nanobiotechnology 13.5 (2021): e1712, by Yi Zheng and Jonathan K. Pokorski. The dissertation author was the primary investigator and first author.

CHAPTER 4 3D PRINTABLE PEDOT FORMULATION AND ITS APPLICATION AS BMI PILOT DEMONSTRATION

4.1 Introduction

PEDOT:PSS is one of the most highly researched conducting polymers due to its combined high electronic and ionic conductivity, mechanical flexibility, thermal stability, and commercial availability[162,163]. In recent years it has been widely applied to applications in energy storage[164], flexible electronics[165], and recently bioelectronics[166] due to its high biocompatibility. Conventional manufacturing techniques such as ink-jet printing[167,168], lithography[169], electrochemical patterning[170,171], aerosol printing[172,173] and screen printing[174,175] are common methods used to fabricate PEDOT:PSS-based electronic devices[176]. However, these methods normally have high processing complexity and often require cleanroom fabrication, which results in high-cost[177]. In contrast to conventional techniques, 3D printing is low cost, versatile, and requires minimal human intervention during fabrication. However, only a few 3D-printable PEDOT:PSS formulations have been reported. These formulations rely on cross-linking biomolecules[178], anisotropic drop-by-drop patterning[179], and microreactive inkjet printing[180]. The reported methods suffer limitations in resolution, require complex experimental setups and tedious processing procedures, which scarcely differentiate them from conventional manufacturing techniques.

In our exploration of 3D printing methods for the fabrication of PEDOT:PSS, we found direct ink writing (DIW) printing as a process of interest because it has the highest material versatility, and has been applied for fabrication of energy materials (such as MXenes- and GO- based inks)[181] as well as versatile 3D structures[182]. However, designing printable PEDOT:PSS ink is limited by

the fundamental process of DIW printing. Recently, a lyophilized PEDOT:PSS ink was developed by Yuk et al. [177], and the prepared ink allowed for the fabrication of high-resolution (≈30 μm) PEDOT:PSS microstructures. This result, while a milestone for the fabrication of PEDOT:PSS still required specialized equipment and a final thermal annealing step. There were additional limitations in compatible substrate material and poor substrate adhesion (especially when exposed to moisture).

In chapter 4, we will describe a coagulation bath-assisted DIW technique for the fabrication of PEDOT:PSS at room temperature, without the use of organic solvents, and describe a simple postprocessing method for strong adhesion on various substrates. In this process, a PEDOT:PSS suspension is extruded from a DIW syringe into a coagulation bath, forming a PEDOT:PSS hydrogel in situ. The hydrogel exhibits kPa-scale Young's modulus, allowing devices to mechanically match biological tissue, and serve for long periods in vivo[183], while exhibiting high electrical conductivity (up to ≈35 S cm−1). Dry-annealing of the prepared PEDOT:PSS hydrogel improves the conductivity (up to ≈600 S cm−1) and Young's moduli of the printed structures (≈1–10 MPa). This liquid-gel transition technique allows for high-resolution patterning of PEDOT:PSS hydrogels (minimum feature size ≈ 20 μm), and also the fabrication of ultra-thin, highly conductive fibers (<10 μm in diameter). By modifying the coagulation bath, the mechanical properties of the hydrogel can be tuned via a one-step interpenetrating network (IPN) formation reaction. With a simple postprocessing treatment, this technique enables PEDOT:PSS to adhere to various substrates, including polyethylene terephthalate, polyimide, and aluminum foil under aqueous conditions. Lastly, we have used our technique to fabricate a cortex-wide neural interface for intracranial electrical stimulation and simultaneous optical monitoring of brain activity via calcium imaging and demonstrated long term biocompatibility and stability of the implanted device.

4.2 Results and discussion

4.2.1 Design of the coagulation-bath assisted DIW PEDOT:PSS

Previous work has demonstrated that injectable PEDOT:PSS hydrogels could be fabricated by mixing a PEDOT:PSS suspension with 4-dodecylbenzenesulfonic acid (DBSA), a surfactant dopant. The suspension undergoes a liquid-to-gel transition and could be molded into geometrically unique parts[184]. The authors' stated that the concentration of DBSA plays a vital role in gelation time (a higher concentration of DBSA, leads to a shorter gelation time); therefore, we hypothesized that patterned PEDOT:PSS hydrogels could be fabricated by extruding a PEDOT:PSS suspension into a coagulation bath containing an appropriate concentration of DBSA. Gratson et al.[185], first brought the idea of applying a coagulation reservoir to solidify fluid inks, realized through direct-write assembly. Here, we combined these two ideas to develop a coagulation-bath assisted DIW method for 3D printable PEDOT:PSS hydrogels using a liquid-gel transition mechanism.

In our printing methodology, concentrated PEDOT:PSS liquid ink is extruded via a DIW nozzle and coagulates immediately into a self-supporting coherent gel when printed into a DBSA coagulation bath. (Figure 1a). Therefore, the concentration of DBSA in the coagulation bath and concentration of PEDOT:PSS are two significant variables which needed to be tuned to achieve optimal printing. Increasing the concentration of DBSA reduces the gelation time of PEDOT:PSS in the coagulation bath; in contrast, insufficient DBSA in the bath results in unstable objects which re-suspend. However, excessive DBSA results in a highly viscous coagulation bath, which leads to dragging of the printed structures and lowers printing resolution. We found that a concentration of 10 wt% DBSA results in stable prints and this concentration was used for all future prints (Figure 1b). For the PEDOT:PSS inks, rheological characterization was used to measure the viscoelastic properties of the ink to ensure compatibility with DIW printers. An amplitude sweep

was used to determine whether a solid-liquid transition point existed to yield a printable ink; in the absence of this transition, a nonprintable ink would result in "spreading" during printing (Figure 4.1C). Once a printable PEDOT:PSS ink was prepared (typically with a weight concentration higher than 3 wt%), we were able to pattern the PEDOT:PSS hydrogel onto a glass slide (via a 100 μm nozzle) (Figure 4.1D). Microscopically, the PEDOT:PSS chains experience a shear-induced alignment during the extrusion caused by a differential shear rate gradient within the printing nozzle's annulus. After the ink was extruded into the coagulation bath, the electrostatic attraction between the aligned PEDOT+ and PSS− chains is weakened by the high ionic strength of the bath, and the exposed PEDOT+ chains re-arrange with DBSA micelles to form an inter-connected PEDOT:PSS network. This network is likely formed due to physical crosslinking promoted by π–π stacking and hydrophobic attractions (Figure 4.1A). Rheological measurements demonstrated a small decrease in the complex viscosity of the printed hydrogel as the shear rate was increased and a stable modulus of the hydrogel over a range of shear rates, which indicated physical cross-linking. (Figure S4.2) The absence of DBSA molecules in the washed PEDOT:PSS hydrogel, as determined by Fourier-transform infrared spectroscopy (FTIR) (Figure S4.3), suggests a noncovalent bonding of DBSA to the PEDOT:PSS. In a simple display of the conductivity achieved using our method of PEDOT:PSS deposition and patterning, two AA alkaline batteries (3 V) were connected via printed electrodes to a LED (white light, 1206) which illuminated brightly (Figure 1E).

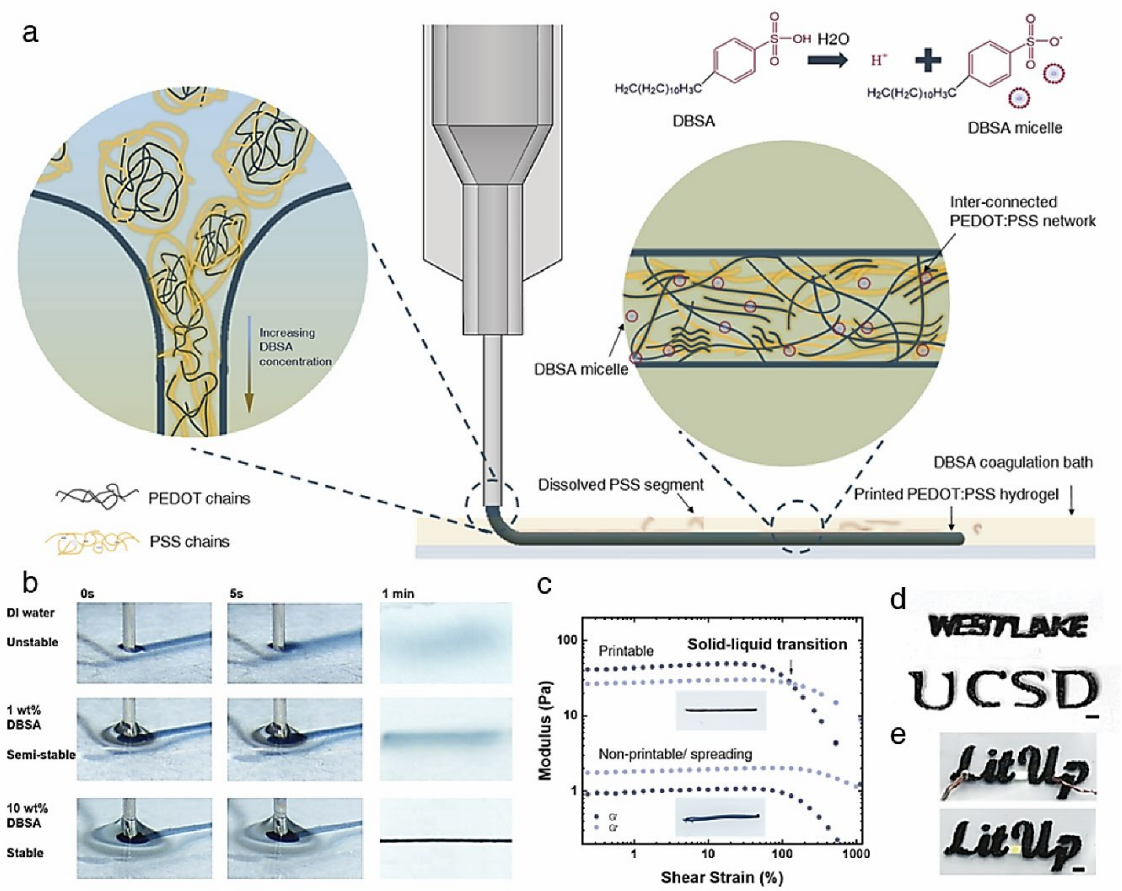

Figure 4.1 Design of coagulation-bath assisted DIW PEDOT:PSS. A) Schematic illustration of coagulation-bath assisted DIW for PEDOT:PSS hydrogel patterning and gelation mechanism of the printed PEDOT:PSS hydrogel during the 3D printing procedure. B) Concentration of DBSA bath is essential during the printing, insufficient concentrations of DBSA result in semi-stable PEDOT:PSS, which will resuspend in the solution after a time period. C) Rheology of printable and nonprintable PEDOT:PSS suspension, a solid-liquid transition point is observed for a printable PEDOT:PSS suspension. D, E) Images of PEDOT:PSS hydrogel patterned by coagulation-bath assisted DIW. E) LED acting as conductive interconnect to bridge letter "lit" and "up" sections of printed geometry and used to exhibit the conductivity of the printed PEDOT:PSS hydrogel. Top: after 3 V DC applied, Bottom: before 3 V DC applied. Scale bar: 3 mm.

4.2.2 DIW provides a new angle for material design

Printing speed and nozzle pressure are two main factors which contribute to the properties of the resultant hydrogel filaments (Figure 4.2A, B, Figure S4.4). With a fixed nozzle diameter of 100 μm, we tested the influence of printing speed and pressure on the extruded filament diameter. As expected, lower printing speed (with a constant printing pressure at ≈28 psi) and higher printing

pressure (with a constant printing speed at ≈140 mm min−1) resulted in larger filament diameters, and vice versa. In the printable range, smooth and consistent printed filament was achieved. However, when printing speed was too slow (lower than ≈90 mm min−1, with a constant printing pressure at ≈28 psi), "spreading" happened; if the printing speed was set too high (higher than 400 mm min−1, with a constant printing pressure at ≈28 psi), "hard-stretching" (the phenomenon of a formed PEDOT:PSS hydrogel being stretched by the fast-moving nozzle) occurred. When printing pressure was set too low (lower than ≈22 psi, with a constant printing speed at ≈140 mm min−1), "under-extrusion" occurred. Likewise, if the printing pressure was set too high (higher than ≈38 psi, with a constant printing speed at ≈140 mm min−1), "over-extrusion" resulted (Figure 4.2C). When filaments are characterized using scanning electron microscopy (SEM), we found that "good prints" showed smooth, consistent, and shear-induced aligned microstructural features. Filaments that showed printing deficiencies of "spreading" and "over extrusion" shared similar porous and nonaligned structure. For print parameters that resulted in "hard-stretching", an aligned coalesced structure was observed (Figure 4.2D). The "hard-stretching" parameters led to ultra-thin PEDOT:PSS fibers (with a diameter less than 10 μm after the prints are washed by DI water and air-dried), while having an anomalously high electrical conductivity of ≈530 S cm−1, suggesting an alternative method to fabricate highly conductive ultra-thin highly conductive fibers (Figure 4.2A).

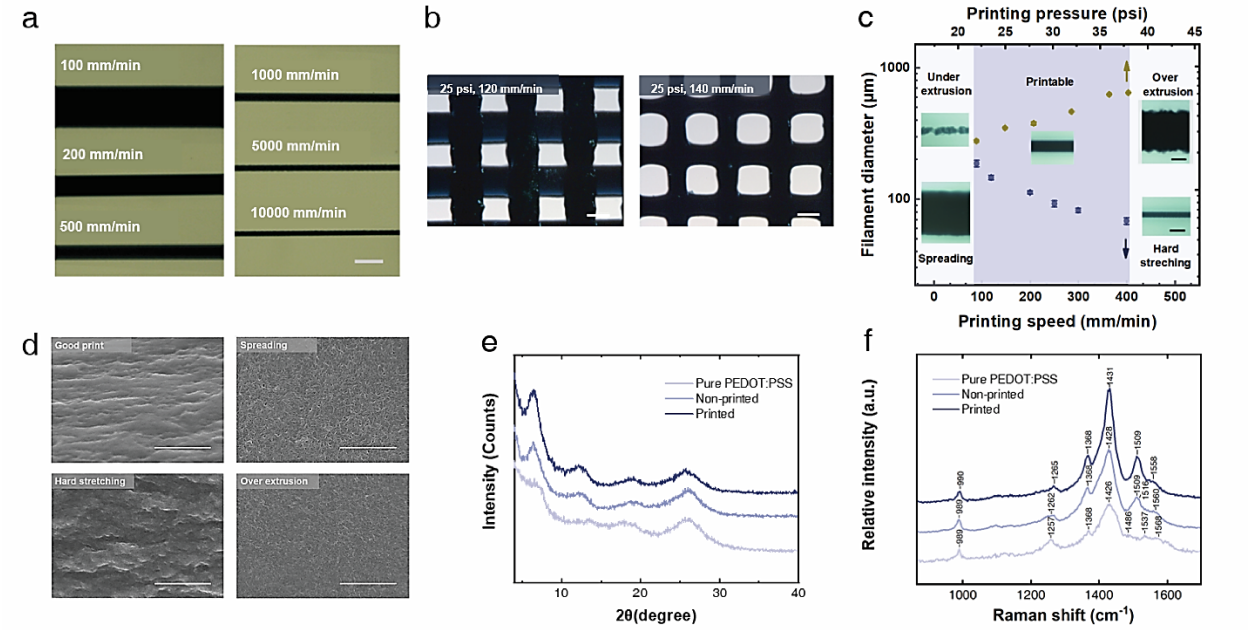

Figure 4.2 Microstructure study of printed PEDOT:PSS. A) PEDOT:PSS hydrogel filaments printed at different printing speeds. (Images collected by optical microscopy). Scale bar = 100 μm. B) woodpile structures formed by the printed PEDOT:PSS with different printing parameters. Scale bar: 150 μm. C) Relation between printing speed and pressure versus filament diameter. Scale bar: 100 μm. Error bars indicate SD; $n = 3$ for each group. D) SEM micrographs of the microstructure of the prints with four printing parameters: "good print", "spreading", "hard stretching," and "over extrusion". Scale bar: 1 μm. E) XRD spectra of pure PEDOT:PSS, nonprinted and printed PEDOT:PSS hydrogel. F) Raman spectra of pure PEDOT:PSS, nonprinted and printed PEDOT:PSS hydrogel.

The coagulation bath technique is able to fabricate a printed PEDOT:PSS hydrogel with a high electrical conductivity of up to ≈35 S cm−1 (see following section on properties of printed material), significantly higher than that of as-produced PEDOT:PSS which only has a conductivity of 10−1 S cm−1[184]. We sought to explain the origins of this high conductivity through microstructural characterization and provide a hypothesis as to the reasons for improved electrical properties.

We hypothesized that the shear and strain-induced rearrangement of PEDOT:PSS chains in combination with the addition of DBSA as a secondary dopant in the coagulation bath gives rise

to the high electrical conductivity we observed from our printed material. Upon printing, the PEDOT:PSS hydrogel immediately adhered to the substrate via hydrogen bonding. As the nozzle moves, it induces a stretching action between the nozzle and the adhered print geometry. We theorize that this stretching action results in strain-induced microstructural rearrangement of PEDOT:PSS chains. In order to evaluate this hypothesis, a printed hydrogel (air-dried), a nonprinted hydrogel (air-dried) and a room-temperature-dried PEDOT:PSS film cast from the ink suspension were prepared for characterization. X-Ray Diffraction (XRD) is first used to evaluate the strain-induced rearrangement within the samples. XRD patterns of PEDOT:PSS have three characteristic peaks: $2\theta = 6.6°$ (d = 13.4 Å), 17.7° (d = 5.0 Å), and 25.6° (d = 3.5 Å), where the lattice spacing (d) is calculated using Bragg's law[186]. The low angle reflections at $2\theta = 6.6°$ corresponds to the lamella stacking distance d(100) of PEDOT and PSS[187,188], whereas the two high angle reflections at $2\theta = 17.7°$ and 25.6° are indexed to the amorphous halo of PSS and the interchain planar ring-stacking distance of d(010) of PEDOT, respectively[188,189]. The XRD patterns of the nonprinted hydrogel and printed hydrogel have several differences from that of pure PEDOT:PSS (Figure 4.2E).

1. After treatment with 10% DBSA, the peak at 6.6° shifts to a lower angle with an increased intensity, also a second-order reflection peaks d(200) at $2\theta = 13.3°$ appears, which indicates increased lamella stacking distance and enhanced crystallinity[189].
2. The peaks of the printed hydrogel have an even higher intensity and the peak at 6.6° shifts to an even lower angle compared to the nonprinted hydrogel, which indicates the printing procedure further increases lamella stacking distance and crystallinity. Single crystal

XRD further supported the strain-induced rearrangement (Figure S4.5).

To further understand the conformational changes within the samples, we investigate the Raman spectra using green light excitation with a wavelength of 532 nm. (Figure 4.2F) In the Raman spectra of pure PEDOT:PSS, the most intense band at 1426 cm−1 is attributed to PEDOT and it corresponds to the Cα = Cβ symmetric stretching vibration of the five-membered thiophene ring originating from neutral parts existing between the localized elementary excitations[189,190]. The band becomes narrower and blue shifted at 1428 and 1431 cm−1 for the nonprinted hydrogel and printed hydrogel, respectively. Peak shifting to higher wavenumbers can be associated with an increase in the sample doping level due to the incorporation of DBSA anions during printing. This effect is related to the degree of backbone deformation during oxidation to polarons and bi-polarons and the associated transitions between quinoid and benzoid structure[191]. A decrease in bandwidth can be seen as additional evidence of further transformation of the PEDOT structure from an irregular coil benzoid structure to a linear or expanded-coil quinoid structure. Another obvious difference between the pure PEDOT:PSS and the DBSA-treated PEDOT:PSS hydrogel is the disappearance of bands at 1486 and 1537 cm−1 and the appearance of a new intense band at 1510 cm−1, this phenomenon may be caused by rearrangement of the PEDOT[191–194]. Moreover, the bands at 1124 and 1098 cm−1 correspond to the vibrational modes of the PSS component of pure PEDOT:PSS, while the intensity of these bands is much lower for the DBSA-treated hydrogels, suggesting that a large portion of the remaining PSS-rich regions are removed during the DBSA treatment[195]. In all, we suspect that the combined effects of increased doping level, chain expansion, removal of PSS insulating polymers, and resultant morphological change together result in the strongly enhanced conductivity of PEDOT:PSS hydrogel when printed in a

DBSA coagulation bath. More pronounced differences are observed in the printed hydrogel, showing the effects of the DIW method in the resultant object's properties.

4.2.3 Characterization of printed PEDOT:PSS

Print pressure and print speed result in microstructural changes of printed materials, which is reflected in the electrical conductivity of parts printed with different parameters. PEDOT:PSS hydrogels, when printed at ≈150 mm min^{-1} and ≈28 psi, showed a conductivity of ≈34 S cm^{-1}, which further increased to ≈280 S cm^{-1} after drying. When print pressure is increased to ≈32 psi, the conductivity decreased to ≈22 S cm^{-1} for the hydrogel and ≈125 S cm^{-1} upon drying. The macroscopic properties of high-pressure prints suggest “over extrusion”, which was correlated to microscopic properties, as described above. When increasing print speed to ≈180 mm min^{-1}, the material had even lower conductivity at≈18 and ≈70 S cm^{-1}, suggesting both “over extrusion” and “hard stretching” happened during printing. However, when print pressure is at ≈36 psi, and print speed as high as ≈240 mm min^{-1}, the conductivity of the printed material showed increased conductivity at ≈22 and ≈110 S cm^{-1} before and after drying, respectively. These results suggested print pressure and print speed need to be optimized in order to achieve fabrication of highly conductive PEDOT:PSS (Figure 4.3A).

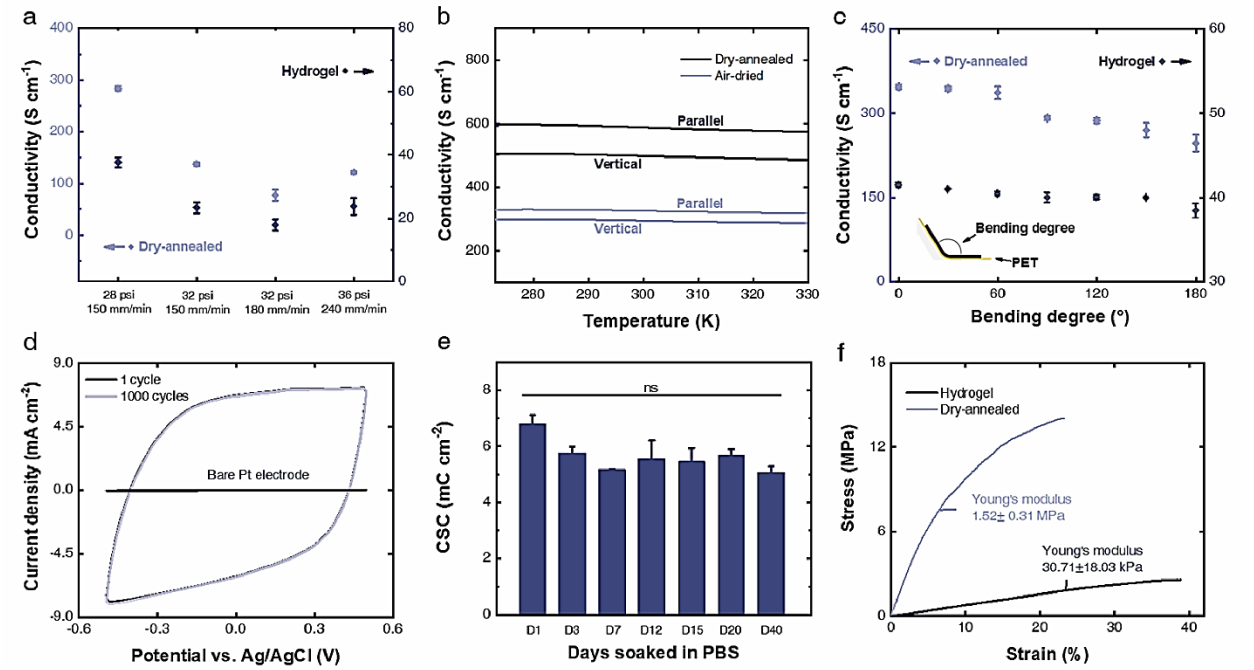

Figure 4.3 Mechanical and electronic properties of the printed PEDOT:PSS. A) conductivity of the printed PEDOT:PSS printed with various printing parameters for both the hydrogel and dry-annealed material. Error bars indicate SD; $n = 3$ for each group. B) Relationship between temperature and conductivity of dry printed PEDOT:PSS and dry-annealed printed PEDOT:PSS. C) conductivity as a function of bend angle for printed PEDOT:PSS hydrogel as well as its dry state. Error bars indicate SD; $n = 3$ for each group. D) CV characterization for printed PEDOT:PSS on Pt substrate. E) characterization of the CSC of the printed PEDOT:PSS hydrogel incubated in PBS over 20 days. Error bars indicate SD; $n = 3$ for each group. F) tensile test results of printed PEDOT:PSS hydrogel and its dry state. NS, not significant

The microstructure of printed PEDOT:PSS show a quasi-uniaxial arrangement of surface grain when examined under SEM. At the same time, the conductivity of the polymer along the print direction exhibits a 15% increase than in the orthogonal direction (indicated as 'vertical' in Figure 4.3B) when in the dry-annealed state and 8% difference when in the air-dried state, suggesting an anisotropic structural arrangement. The stable conductivity of the samples over temperature range from 273 to 330 K, shows potential to be applied for bioelectronics (Figure 4.3B). Consistent conductivity of the material during flexure is an essential property for biocompatible electronics. Therefore, to investigate the effect of mechanical bending on the electric properties of our printed PEDOT:PSS, we measured the electrical conductivity of a line

printed with a 100-μm nozzle from PEDOT:PSS on a flexible polyethylene terephthalate (PET) substrate and plotted this conductivity as a function of the bend angle. The printed PEDOT:PSS sample showed less than 5% change in electrical conductivity across a wide range of bend angles in the hydrated states, while ≈25% difference in the dry-annealed state, this might be caused by more tightly packed conductive PEDOT-rich cores (Figure 4.3C). Another property which is important to versatile bioelectronics is the conductive material's electrochemical stability. To investigate the electrochemical properties of the printed PEDOT:PSS hydrogel and its long-term stability in physiological conditions, we performed cyclic voltammetry (CV) of the saturated hydrogel in a phosphate-buffered saline (PBS) solution. The CV response demonstrates a high charge storage capability (CSC) of the printed PEDOT:PSS hydrogel (100-μm nozzle, 1 layer on Pt clamp) when compared to a typical metallic electrode material, such as Pt, with exceptional stability (less than 2% reduction in CSC after 1000 cycles) (Figure 3d). The printed PEDOT:PSS maintained its high CSC value (with less than 5% change) even after 40 days of incubation (Figure 4.3E). The CV of the printed PEDOT:PSS further shows broad and stable anodic and cathodic peaks under varying potential scan rates, suggesting nondiffusional redox processes and electrochemical stability of the printed PEDOT:PSS (Figure S4.6).

Lastly, it was important to characterize the mechanical properties of the PEDOT:PSS hydrogel to evaluate its potential to match the modulus of biological tissue, and to assess its mechanical durability. The mechanical properties of the printed PEDOT:PSS were investigated through tensile testing of a rectangular shaped sample (single layer, 100 μm printing nozzle, 30 × 5 mm). We found that the printed PEDOT:PSS displayed a Young's modulus of 1.52 ± 0.31 MPa in the dry-annealed state, and of 30.71 ± 18.03 kPa in the hydrated state. (Figure 4.3F) The superior softness and high conductivity of the printed PEDOT:PSS suggests favorable long-term biomechanical

interactions with tissue, which could bear tremendous potential in bioelectronics devices and implants, especially in neuromodulation therapies[55,196].

4.2.4 Highlights of the coagulation-bath assisted DIW technique

The coagulation bath technique demonstrated exceptional precision and yielded parts with excellent electronic properties. We anticipated that this technique could provide two additional features to improve upon 3D-printed PEDOT:PSS bioelectronics. PEDOT:PSS materials typically have poor mechanical properties and exhibit poor substrate adhesion for device fabrication. Both concerns are addressed by either a single step-modification within the coagulation bath to further reinforce printed materials, or a simple substrate treatment to improve adhesion.

4.2.4.1 Mechanical property improvement

The coagulation bath offers the possibility to control the composition of the resulting PEDOT:PSS parts by altering the composition of the bath. For example, one opportunity is the formation of IPNs to improve upon the mechanical properties of the gels. Infiltration with precursors of a secondary hydrogel is a common method to modify the mechanical properties of pre-formed PEDOT:PSS hydrogels[179,194]. Here, instead of infiltrating the preformed first network with a second network of monomers/precursors, the coagulation bath allows for a one-step formation of IPNs by adding the precursors of a secondary hydrogel into the coagulation bath along with DBSA. We selected polyacrylamide (PAAm) as the secondary network to enhance the Young's modulus of the PEDOT:PSS hydrogel and we suspected it would not impact the electrochemical properties. To synthesize the IPN, acrylamide, a cross-linker (N,N′-methylenebisacrylamide (MBAA)), and a thermal radical polymerization initiator (2,2′-azobis(2-methylpropionamidine) dihydrochloride (VA-044)), were added into the coagulation

bath along with DBSA. The IPN was cured via radical polymerization at 50 °C for three hours, after which we observed an almost six-fold increase in Young's modulus, with no substantial change in conductivity. (Figure 4.4A)

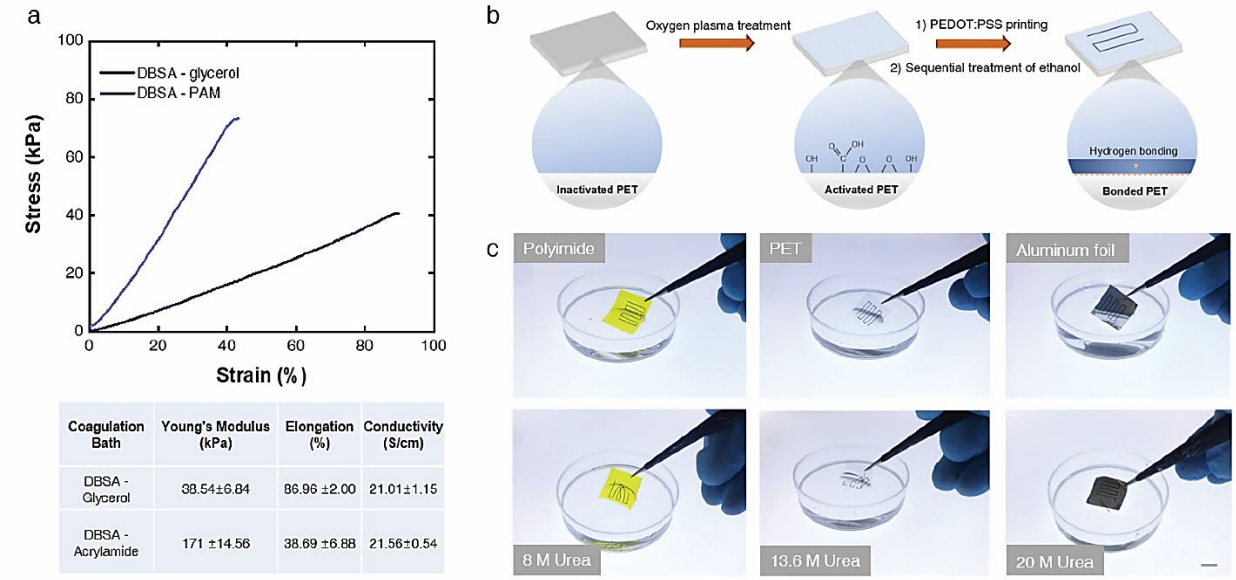

Coagulation Bath	Young's Modulus (kPa)	Elongation (%)	Conductivity (S/cm)
DBSA - Glycerol	38.54±6.84	86.96 ±2.00	21.01±1.15
DBSA - Acrylamide	171 ±14.56	38.69 ±6.88	21.56±0.54

Figure 4.4 Highlights of the coagulation-bath assisted DIW technique. A) Mechanical properties of PEDOT:PSS hydrogel printed into solvent additive treated coagulation bath and infiltrated w/ secondary PAAm. Error bars indicate SD; $n = 3$ for each group. B) Simple substrate activation and postprocessing help to stabilize adhesion of printed PEDOT:PSS on substrate. C) top, Printed PEDOT:PSS structures on various treated substrate submerged in DI water overnight; bottom, Printed PEDOT:PSS structures fell apart from various substrate under different urea concentration. Scale bar = 1 cm.

Solvent additive treatment can be a processing method of solvent addition and solvent-thermal post-treatment[195,196]. This treatment can not only enhance the conductivity of PEDOT:PSS, but also the thermoelectric properties and mechanical stretchability[55]. For example, Liu., et al.[197]mixed glycerol with PEDOT:PSS to manufacture morphing electronics. Here the addition of 20 wt% glycerol to the coagulation bath, resulted in PEDOT:PSS hydrogel samples with nearly 300% higher elongation than the unmodified samples, with little difference in conductivity. (Figure 4.4A)

4.2.4.2 Strong adhesion to various substrates

Weak and unstable adhesion of PEDOT:PSS on substrates is a significant problem that has proven a hindrance to the application of PEDOT:PSS in bioelectronics[197]. Even though several surface modification methods have been studied[197–202], none have proved suitable for long term biocompatibility of a 3D-printed PEDOT:PSS hydrogel. The main reason for weak adhesion between PEDOT:PSS and the substrate in a physiological environment is due to the strong hydrogen bonding between the PSS and water which causes the prints to release from the substrate because they are drawn away from the hydrophobic polymer substrate and towards the more favored aqueous environment. Therefore, reducing the amount of hydrogen bonding between PSS and water, and increasing the amount of hydrogen bonding between PSS and the substrate could be one avenue for obtaining strong adhesion. Here, with simple substrate treatment and postprocessing, we achieve strong adhesion of PEDOT:PSS to several substrates. Polyethylene terephthalate (PET) was used as the starting substrate, as it is one of the least expensive transparent substrates that is commonly used for flexible electronics (Figure 4.4B)[203].

Fortuitously, the hydrophilic sulfonate group of PSS can hydrogen-bond with the oxygen in PET, adhering the two materials[204]. However, if treated with water, the bonding between PSS and PET is largely reduced and results in prints releasing from the substrate. Therefore, to strengthen this bond between the PEDOT:PSS and the substrate, there are two problems which must be solved: 1) increasing the amount of hydrogen bonding between the prints and substrate, and 2) removing excess DBSA from the prints without causing them to release from the substrate. We investigated a route to strengthen the hydrogen bonding between the PEDOT:PSS and the substrate. First, oxygen plasma treatment is applied to clean and activate the substrate, increasing its hydrophilicity and assisting in the formation of hydrogen bonds between the prints and

substrate. To remove the DBSA, prints were tilted slightly and allowed to drain for at least half an hour. After this procedure, anhydrous ethanol was gently added dropwise onto the prints to wash away remaining water molecules and dissolve any remaining DBSA, without causing loss of adhesion. The prints were then placed on a hot plate for two minutes at 40 °C to evaporate the ethanol. This gentle evaporation of ethanol guides the formation of hydrogen bonds between PET and PSS, resulting in the enhancement of adhesion of the prints on the substrate. The ethanol treatment step should be repeated at least three times to fully remove the DBSA and ensure complete hydrogen bonding between PEDOT:PSS and the substrate. This process can also be applied to polyimide (PI) films, another type of insulating film widely used in the electronics industry and aluminum foil, which could be used for radiation and electromagnetic shielding. To test the adhesive ability, we soaked the printed sample in deionized water overnight and found that the prints have stable adhesion to these substrates, which broadly increases the applications of this technology (Figure 4c, top). Finally, to demonstrate hydrogen bonding is the main force to adhere PEDOT:PSS on these substrates, we introduced urea to disrupt hydrogen bonds[205]. After soaking in 8M urea solution for one hour, the prints fell off from PI, though not from PET nor aluminum foil. The prints fell off from PET when the urea concentration was increased to 13.6 M, however, only a portion of the prints fell from the aluminum foil at a urea concentration at 20 m under vigorous agitation, showing a strong hydrogen bonding strength (Figure 4.4C, bottom).

4.2.5 3D printing of PEDOE:PSS bioelectronics

This coagulation bath-based DIW technique opens a plethora of new avenues for rapid innovation of high resolution and multi-material flexible electronics, and bioelectronics. Furthermore, strong adhesion on PET under aqueous condition enables a multi-material fabrication of a functional bioelectronic device. To demonstrate this, we printed a micro-Electrocorticography (μECoG) type cortex-wide neural interface (entire processing time of conducting electrodes less

than 20 min) allowing intracranial electrical stimulation and simultaneous calcium imaging of brain activity in mice (Figure 4.5A). The μECoG electrodes are placed epidurally on the surface of the brain and offer a high signal-to-noise ratio (SNR) as well as a localized cortical signal without complications such as infection, biological rejection, and signal instability that intracortical neural probe commonly have[206–208].

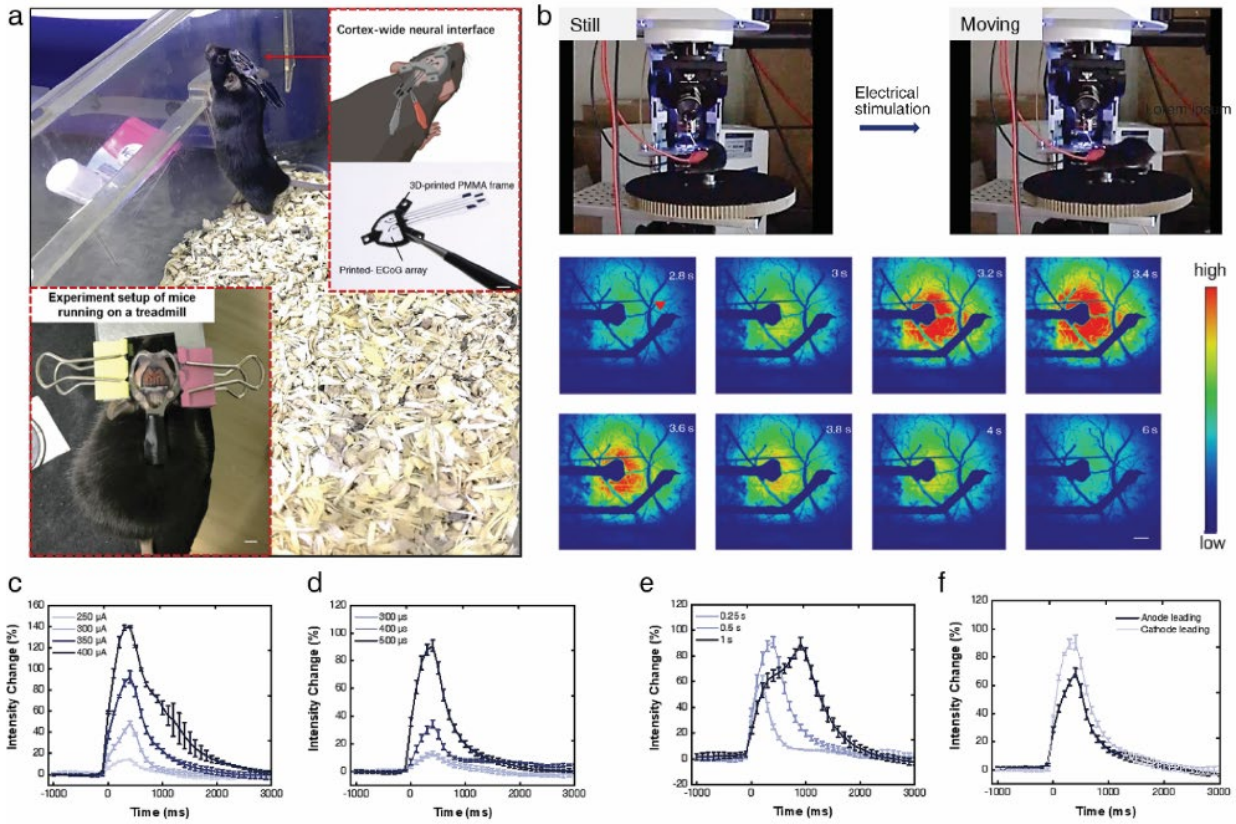

Figure 4.5 Cortex-wide neural interface with printed PEDOT: PSS electrodes. A) A mouse bearing four-channels cortex-wide neural interface with printed PEDOT:PSS electrodes post three-weeks implantation. The electrodes have a diameter of 200 μm on the sensing tip. Scale bar: 5 mm. Images of the implanted neural interfacing (left) and a freely moving mouse with the implanted neural interfacing (right). B) top: Image of the mouse on the treadmill w/ and w/o electrical stimulation; bottom: visualization of the intensity of neural response to 400 μA electrical stimulation at times 2.8–6 s in a pulse cycle. Region of interest (ROI) used for fluorescence analysis was marked with a red triangle. Scale bar: 200 μm. C) Fluorescence intensity change of the ROI over time as a function of various pulse amplitude. D–F) With a constant current of 350 μA, fluorescence intensity change of the ROI over time as a function of various pulse width, pulse duration and anode/cathode leading, respectively.

GCaMP6f is a fast and highly sensitive calcium indicator which fluoresces when bound to Ca^{2+} ions such as those encountered in mouse neural pathways[209,210]. Therefore, it is an excellent tool for imaging real-time neuronal activity in vivo. Cortex-wide neural interfacing enables simultaneous monitoring and modulation of neural activity from multiple cortical regions over a long period of time (>300 days)[211]. As a feasibility study, we fabricated a four-channel μECoG array with a feature size of 200 μm which yielded a high charge injection capacity of 6.366 mC cm^{-2} and a low impedance of 2.00 ± 0.23 kΩ at 1 kHz, suitable for in vivo stimulation[210]. We applied electrical stimulation with a current that varied from 100 to 400 μA to the electrodes which were placed directly above the mouse's motor cortex and observed the motor reaction upon E-stimulation when current was higher than 250 μA. (Figure 4.5B, top). Wide-field microscopy visually demonstrated the fluorescence changes evoked by neural activity (Figure **4.5B**, bottom). We further studied the effect of different pulse parameters on the mouse's neuronal activity. As expected, an increase of neural activation in response to higher stimulation amplitude, larger pulse width and duration were observed (Figure 4.5C, D). However, long pulse duration (1s) showed inhibition of the neural response and resulted in slower and less intense responses (Figure 4.5E). Finally, we observe a faster and larger neuronal activity in the cathode leading stimulation compared with the anode leading stimulation, which was noted in previous studies (Figure 4.5F)[212].

After three-weeks postimplantation, the impedance between the leftmost and rightmost electrodes is 14.9 ± 0.54 kΩ in vivo, and the electrodes on the cortex are still intact three-months postimplantation suggesting the electrode array experienced minimal degradation in the physiological environment and demonstrating the case for long-term stability at the neural interface (Figure S4.8).

4.3 Experiment section

4.3.1 Preparation of PEDOT:PSS ink

PEDOT:PSS (CleviosTM PH1000) was stirred vigorously for 1 h at room temperature, and roughly 11 g of PEDOT:PSS was charged into a 50 mL round bottomed flask. A rotary evaporator was used to concentrate the PEDOT:PSS suspension in the flask at 50 °C until it became highly viscous. The gel-like mixture was vigorously stirred, via magnetic stir bar, overnight at room temperature. Next, a 10 μm syringe filter was used to filter off large aggregates from the gel, followed twice by a 1 μm syringe filter to yield PEDOT:PSS ink. The ink was characterized using rheology (see below rheological characterization for detailed information) to ensure a solid-to-liquid transition point under applied shear. After filtration, the PEDOT:PSS ink was placed in a falcon tube (50 mL) and degassed by centrifugation at 1200 rpm (2x for 3 min), in order to fully remove the trapped air. The prepared ink was kept at 4 °C prior to use and was brought to room temperature for at least 30 min prior to use.

4.3.2 3D printing procedure and PEDOT:PSS printed structure preparation

The coagulation bath based DIW PEDOT:PSS printing was carried out using a custom-made 3-axis micropositioning stage, consisting of a z axis on which one 3 cc syringe was loaded with the PEDOT:PSS ink connected to a fluid dispenser (Performus V, EFD Inc, East Providence, RI, USA). For ink extrusion, nozzles (100- and 60- μm nozzles from TaoBao) were attached to the syringe barrels. Prior to printing, the nozzle was briefly immersed in the coagulation bath. G-code was generated either by hand or using Bio-Architect (Renenovo). All 3D printing processes were performed under ambient conditions with a relative humidity of 20- 40% and a temperature of 22–27 °C.

Two postprocessing steps were completed to make the following materials. 1) Hydrogel preparation: The printed PEDOT:PSS together with the substrate was placed into a petri dish filled with deionized water. The water was discarded and refilled at least three times to remove DBSA to form PEDOT:PSS hydrogels. 2) Air-dried or Heat-annealed PEDOT:PSS: An absorbent tissue (Kimwipe) was used to remove as much remaining water from the hydrogel as possible. For the air-dried structure preparation, the PEDOT:PSS hydrogel was placed in a chemical fume hood overnight to evaporate remaining water. For heat-annealed structure preparation, The PEDOT:PSS hydrogel was placed onto a hot plate, and heated at 40 °C for 30 min to remove residual water, followed by 30 min dry-annealing at 130 °C.

4.3.3 Rheological characterization

Rheology (DHR-3, TA Instruments) was used to determine the flow properties of the ink and the printed PEDOT:PSS hydrogel. Samples were measured using a 25 mm diameter plane plate with a 500 μm gap between the parallel plates at 25 °C. The viscosities of inks were measured using a shear sweep increasing from 0.01 to 100 s−1. The shear modulus of the printed hydrogel was tested as a function of oscillation frequency from 0.1 to 100 s−1 at a shear strain at 1%. All rheological characterizations were conducted at 25 °C with preliminary equilibration time of 1 min.

4.3.4 Experimental of the microstructure study of the printed PEDOT:PSS

Fourier transformation infrared (FTIR) spectroscopy (Nicolet iS50, ThermoFisher Scientific Co., Ltd, US), Powder X-Ray diffractometer (D8 40 Advance, Bruker Co., Ltd). DUO microsourced single crystal X-Ray diffractometer (D8 Venture, Bruker Co., Ltd, Germany), and Raman spectroscopy (Alpha300R, WITec).

4.3.5 Physical properties characterization

Optical imaging and electron microscope imaging – Micrographs of the printed PEDOT:PSS parts were taken using optical (AXIO Zoom.V16, Zeiss) and scanning electron microscopy (SEM). Scanning electron micrographs of the microstructure of printed PEDOT:PSS were obtained with a Regulus 8230m (HITACHI) at 5.0 kV with 5 nm gold sputtering to enhance image contrasts.

Electrical conductivity measurements – The conductivity of the printed PEDOT:PSS was tested with a four-point probe method using Physical Property Measurement System (PPMS-16T, Quantum Design). A customized measuring system (Keithley 6221 and Keithley 2182 Source Meter, Keithley) was used to test the bending-conductivity by a four-point probe method at room temperature. The width and length of the samples were measured by caliper; ultra-thin fibers were measured with the assistance of SEM.

Electrochemical measurements – Cyclic voltammetry (CV) was performed using an electrochemical workstation (Zennium pro, Zahner) with a range of scan rates (10–130 mV s−1). Pt wire (diameter, 1 mm) was employed as a counter electrode (CE), Ag/AgCl electrode was used as the reference electrode (RE), and the printed PEDOT:PSS was employed as the working electrode (WE). 1x PBS was used as the supporting electrolyte. For the long-term electrochemical stability test, the samples were kept in 1x PBS during the test.

Mechanical testing - The mechanical properties of the samples were tested using universal mechanical testing equipment (CTM 6000, Xieqiang Instrument Manufacturing Shanghai Co., LTD) with a 5 N load cell at a rate of 5 mm min−1. Test samples were printed into rectangular shapes (single layer, 100 μm printing nozzle, 30 × 5 mm), and calipers were used to measure cross-sectional areas.

4.3.6 Sample preparation of the materials presented in highlights

One-step interpenetrating network (IPN) hydrogel – The coagulation bath was modified as followed for the one-step IPN formation: 0.0243 mol, 1.727 g acrylamide (Sigma Aldrich, CAS Number 79-06-1), 0.00012 mol, 0.0388 g 2,2′-azobis(2-methylpropionamidine) dihydrochloride (VA-044) (J&K, CAS Number 27776-21-2) and 0.000016 mol, 0.0025 g N,N′-Methylenebisacrylamide (MBAA) (damas-beta, CAS Number 110-26-9) were dissolved in 10 mL 10% DBSA. After printing, the prints were incubated in the coagulation bath for 15 min, then a pipette was used to remove excess coagulation bath. The printed part was heated to 50 °C for 3 h to activate radical polymerization. Following polymerization, the hydrogel was washed with deionized water to remove DBSA and small molecules.

Solvent additive treatment – The coagulation bath was modified as followed for the solvent additive treated hydrogel: 10 wt% of DBSA and 20 wt% of glycerol (Sigma Aldrich, CAS Number 56-81-5) were dissolved in deionized water using a stirring bar at room temperature. After printing, the prints were incubated in the coagulation bath for 15 min, then a pipette was used to remove excess coagulation bath, followed by washing with distilled water (3x).

Treatments for substrate adhesion - The substrate (PET, PI and aluminum foil) was first placed in a plasma cleaner (PCE-6, MTI Corporation) for 3 min at high power (RF power at 30W) to clean and activate the substrate. After printing on the activated substrate, the prints were slightly tilted to drain at room temperature for at least half an hour, then gently immersed in ethanol (Anhydrous, ≥99.7%) and the solution was discarded. The print is then placed on a hot plate for 2 min at 40 ° C. The ethanol treatment and heating were repeated twice.

4.3.7 Substrate Adhesion Test

Substrate adhesion testing was performed in a modified previous method by soaking the sample in 15 mL of deionized water in a petri dish (P139797C, Titan) overnight[204]. Each sample was then held by tweezers and vigorously swirled by hand in the petri dish for one minute.

4.3.8 Fabrication of Cortex-Wide Neural Interfacing

The cortex-wide neural interfacing fabrication includes two parts of PET film preparation and neural interface assembly.

4.3.9 PET Film Preparation

A four-channel electrode array was printed on to an oxygen plasma-treated PET film using the ethanol treatment procedure to secure bonding between the printed electrodes and PET. Thermal release tape (REVALPHA, Nitto Denko) was used to cover the tip of the electrode array and the attachment pad at the end, and a small amount of PDMS (SYLGARD 184 at 10:1 base: curing agent) was used to cover the tip of the electrode array. The electrode array was then placed vertically to coat the entire electrode surface with a thin layer of PDMS using a flow coating method. The PDMS was cured by placing the prints over a hotplate for 3 h at 50 °C. Finally, the temperature was raised to 120 °C to detach the tape and remove it to obtain the prepared PET film electrode.

4.3.10 Neural Interface Assembly

Frames used in this study were as Ghanbari et al. described[211]. The frames were 3D-printed out of acrylate resin (RS-GPBK-03, Formlabs Inc.) using a stereolithography (SLA) printer (Form3, Formlabs Inc.). Three holes in the frame were tapped using a #0-80 hand tap. An outline matching the frame was drawn on the PET film, with electrodes in the center of the outline. A pair of scissors

was used to cut the PET film using the printed outline as a reference. The film was then aligned to the PMMA frame and bonded using a clear, two-part quick setting epoxy adhesive (Scotch-Weld™ DP100 Plus Clear, 3M Inc.). The customized titanium headplate was also as Ghanbari et al. described[211].

4.3.11 Charge Injection Capacity (CIC)

CIC of the four-channel ECoG array was measured by published methods[210,213]. The three-electrode system described above was used, and charge-balanced constant current pulse trains (cathode leading, 500 us phase, 100 Hz) generated by a Master-8 Programmable Stimulator (A.M.P.I) were applied through WE and CE. The current varied from 100 μA to 4 mA. The voltage between WE and RE was monitored by an oscilloscope. And the voltage of 50 μs following the falling edge of the cathode phase was regarded as the maximum negative polarization potential (Emc). We used the potential of −0.5 V as the threshold to determine the maximum CIC.

4.3.12 Animals

Male C57BL/6J mice (8–12 weeks of ages, Laboratory Animal Resource Center at Westlake University) were used. Both virus injection and in vivo surgical implantation can be found in SI. All animal studies and experimental procedures were approved by the Institutional Animal Care and Use Committee (IACUC) at Westlake University, and in accordance with the US National Institutes of Health Guide for the Care and Use of Laboratory Animals.

4.3.13 Wide Field Imaging

No randomization or blinding were used for animal studies throughout. All attempts at replication were successful. Mice with no detectable green fluorescence after surgery were excluded from the study. We did not perform a power analysis for animal study, since our goal was to invent and

validate a new technology; as noted in[214], and recommended by the NIH, “In experiments based on the success or failure of a desired goal, the number of animals required is difficult to estimate…” As noted in the aforementioned paper, “The number of animals required is usually estimated by experience instead of by any formal statistical calculation, although the procedures will be terminated [when the goal is achieved].” These numbers reflect our past experience in developing neurotechnologies. All mice were allowed to recover from surgery for ⩾7 days before imaging experiments were attempted.

All optical recordings were acquired on a wide-field BX51WIF fluorescence microscope (Olympus) equipped with an ORCA-Fusion Digital CMOS camera (Hamamatsu Photonics K.K., Japan), 10× NA0.25 LMPlanFI air objective (Olympus), 470-nm LED (ThorLabs, M470L3), a green filter set with a 470/25-nm bandpass excitation filter, a 495-nm dichroic, and a 525/50-nm bandpass emission filter. Optical recordings were acquired at 10 Hz with HCImage Live (Hamamatsu Photonics, Japan).

Under mild anesthetization, mice were head-fixed under the wide field microscope in a custom-designed disk treadmill. HC Image Live data were stored as DCAM image files (DCIMG), and further analyzed offline in Fiji/ImageJ.

4.3.14 In Vivo Impedance Measurement

In vivo impedance of 1 kHz was measured by a handheld LCR meter (TH2821A, Changzhou Tonghui Electronic Co. Ltd.) using two-electrode system.

4.3.15 In Vivo Stimulation

The Pulse Pal (Open Ephys) was used to trigger CMOS camera and generate electrical stimulation via ISO-Flex (A.M.P.I.). Two ISO-Flex isolators were connected to the Pulse Pal. One was used to drive the positive phase of the bipolar pulse, and the other to drive the negative phase. Two flat copper alligator clips were connected to the electrodes to introduce stimulation.

Each stimulation block consisted of ten trials with an interval of 20 s. Per trial was delivered at 100 Hz with pulse width of 300/400/500μs, and the train duration was 0.25/0.50/1.00 s, respectively. Various levels of electrical stimulation (250, 300, 350, and 400 μA) applied through one site of the PEDOT:PSS electrodes, and returned from the other site. The current amplitudes were justified based on the previous studies that applied transcranial electrical stimulation[215–217]. The corresponding charge densities with pulse width of 500 μs were 397.89, 477.46, 557.04, and 636.62 μC cm-2, respectively. And the voltage course was monitored throughout the experiment to ensure it stayed in the biological safe range.

Shannon's developed an equation for the maximum safe level for stimulation according to the empirical data:

$$\log\left(\frac{Q}{A}\right) = k - \log(Q)$$

, where Q is charge per phase (μC per phase), Q/A is charge density per phase (μC cm−2 per phase), and $1.50 < k < 2.00$[218]. For the electrode site's diameter of 200 μm and maximum stimulus parameters of 400 μA, 500 μs per phrase, the calculated k was 2.10, which was slightly more than the given threshold 2.00. For the rest parameters, the k value was less than 2.00. However, we measured the CIC to ensure that current applied on the electrodes would not let the voltage go

beyond the water window. What's more, the current was increased gradually from a low current to ensure biosecurity during experiments. And in the experiments, no obvious tissue damage or vascular rupture were observed, and the Ca2+ response was stable and repeatable, reflecting the tissue and electrode remained intact[219]. Therefore, we believe the stimulus parameters are biosafe.

4.4 Conclusion

In summary, we have developed a coagulation-bath assisted DIW technique to fabricate high-resolution, high conductivity and stable electrochemical PEDOT:PSS structures. This technique comes with several advantages that include a simple experimental setup and inexpensive printing hardware. The reported printing technique allows for several modifications to the resultant PEDOT:PSS material by simple modification of the bath chemistry. With a simple postprocessing method, the prints demonstrated excellent substrate adhesion, and further postprocessing (such as flow coating, multi-material 3D printing, chemical modification, etc.) can be applied to the prints to further broaden the use of the material, especially in the field of bioelectronics. As a demonstration, we fabricated a cortex-wide neural interface, and recorded the optical and physical response of electrical stimulation as well as simultaneous full-field monitoring with a printed PEDOT:PSS electrode array. Finally. this work establishes a new 3D printing technique for polymer processing, demonstrating the capability and versatility of DIW as a simultaneous physical and chemical patterning method to achieve favorable macro- and microstructural features laying the road for future development of DIW in the field of material design and synthesis.

4.5 Supplemental Figures

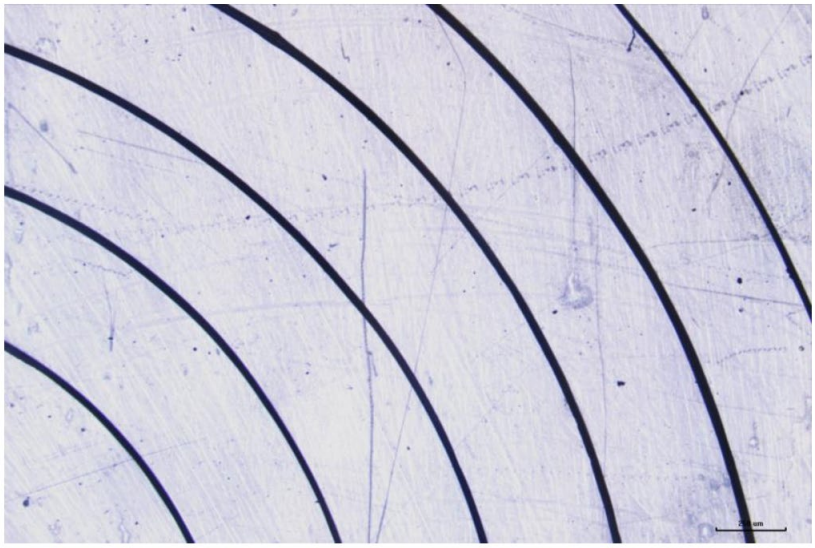

Figure S4.1 High resolution electroconductive hydrogel (image collected by optical microscopy). Scale bar = 250 μm

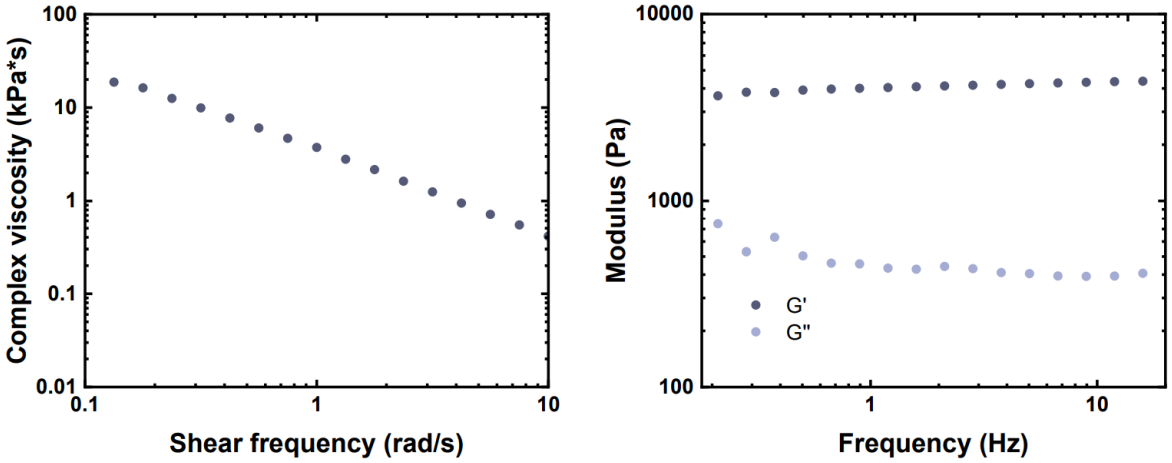

Figure S4.2 Rheological behavior of the printed PEDOT:PSS hydrogel. Left: Complex viscosity of printed PEDOT:PSS hydrogel as a function of shear frequency. Right: Shear modulus of printed PEDOT:PSS hydrogel as a function of oscillation frequency.

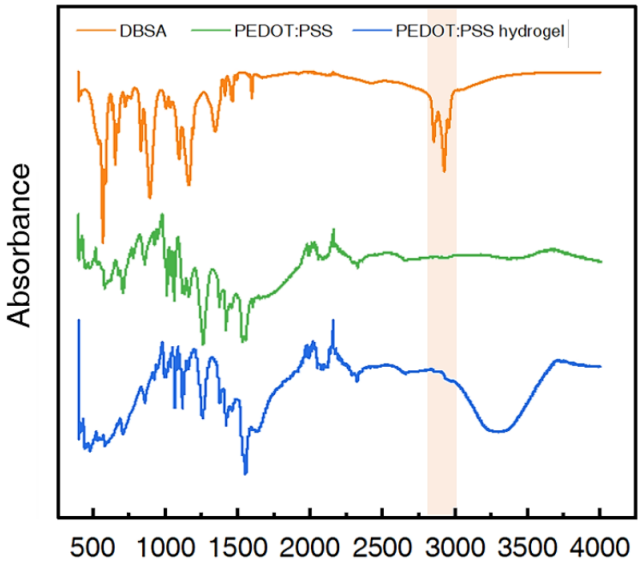

Figure S4.3 FT-IR spectra of pure DBSA, air-dried PEDOT:PSS and printed PEDOT:PSS hydrogel. The peaks from 2800 to 2950 cm-1 are the characteristic peaks of DBSA, which are attributed to (C-H) stretching vibration in benzene ring and aliphatic chain. No obvious peak from this region is observed in PEDOT:PSS hydrogel, suggesting the absence of DBSA in the final PEDOT:PSS hydrogel.

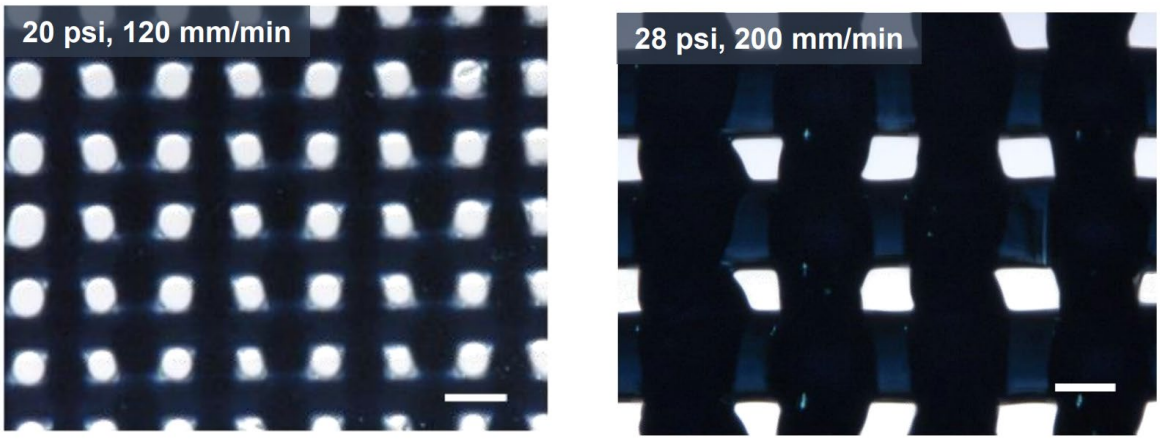

Figure S4.4 Distorted structure caused by unmatched printing parameters. Woodpile structures formed by the printed PEDOT:PSS with varied printing parameters. Scale bar: 150 μm.

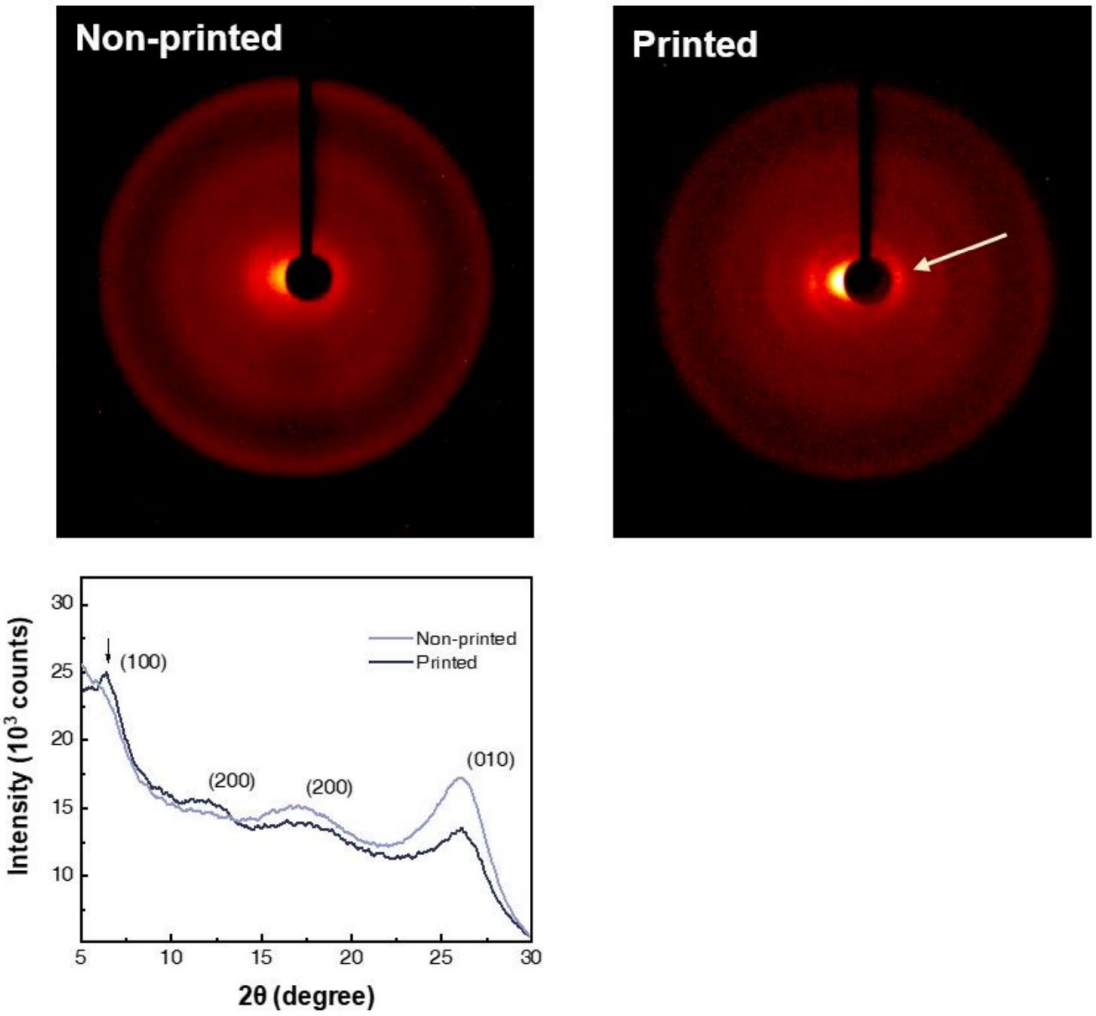

Figure S4.5 Single crystal X-ray diffraction precession image of PEDOT:PSS hydrogels. Printinginduced alignment of PEDOT:PSS in the direction of 2θ = 6.6° and 12.2°, and induced the crystallization of lamella stacking of d (100) compared to non-printed PEDOT:PSS hydrogel. The higher angle of 17.4° and 25.6° represented the amorphous halo of PSS and the inter-chain planar ring-stacking distance d (010) of PEDOT:PSS.

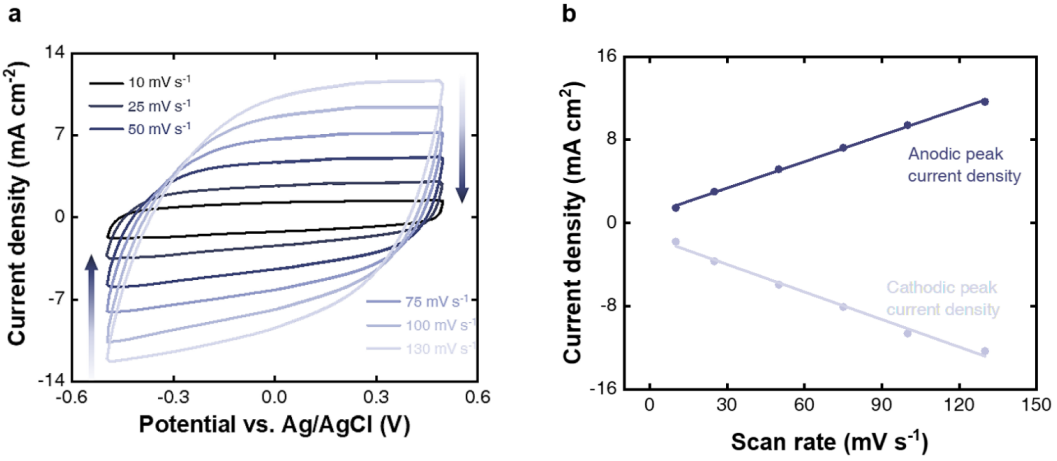

Figure S4.6 CV characterization of printed PEDOT:PSS hydrogel at varying scan rate. A) CV characterizations of the printed PEDOT:PSS hydrogel on PT substrate at varying potential scan rates from 130 to 10 mV s-1 . B), Anodic and cathodic peak current densities as a function of potential scan rates during the CV characterizations.

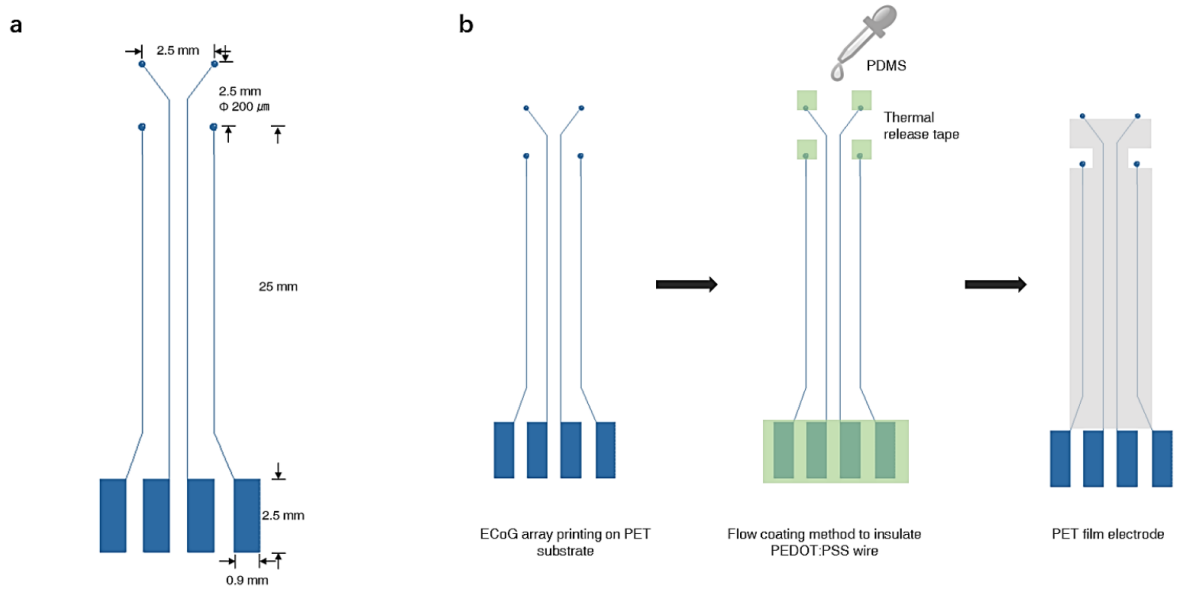

Figure S4.7 PET film preparation of cortex-wide neural interfacing fabrication. a, Design and dimensions of the ECoG array. b, Process of PET film preparation.

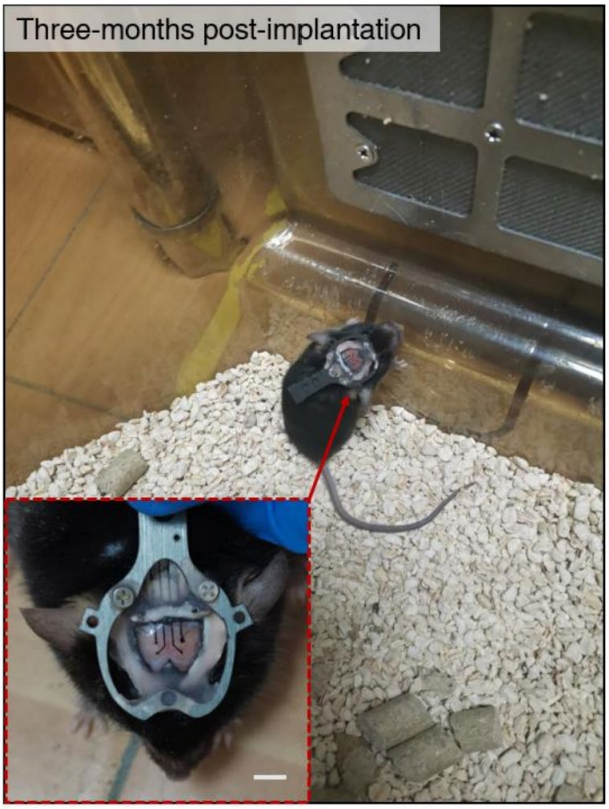

Figure S4.8 Cortex-wide neural interface with printed PEDOT:PSS electrodes three-months postimplantation. Scale bar = 5 mm.

Acknowledgements

Chapter 4, in full, is a reprint of the material as it appears in “Coagulation Bath‐Assisted 3D Printing of PEDOT: PSS with High Resolution and Strong Substrate Adhesion for Bioelectronic Devices." Advanced Materials Technologies (2022): 2101514, by Yi Zheng, Yangdong Wang, Fan Zhang, Shaomin Zhang, Kiryl D. Piatkevich, Nanjia Zhou, Jonathan K. Pokorski. The dissertation author was the primary investigator and first author.

. CHAPTER 5 CONCLUSION

5.1 Summary of the Dissertation

Polymer is a highly versatile material, which can be chemically modified and mechanically processed into different physical status in various structures performing desired properties. Due to the inclusiveness of polymer science, it has become a multidisciplinary subject. In this dissertation, polymer science is applied as the cornerstone, and presenting its tremendous potential in the biomedical fields with the cross-sectional knowledge input from molecular biology, chemistry, and materials science.

In Chapter 1, RAFT living polymerization was utilized to synthesize a PEGMEA/ TMGMV nanocomposite hydrogel. TMGMV provides the robust strength to the soft PEGMEA hydrogel, and it increase the storage modulus of PEGMEA hydrogel composite to four-fold with only 0.1% addition of TMGMV. Not only with hydrogel system, but we also investigated its mechanical strengthen property in PVA film system. Estimate 67% tensile strength was observed with 1.6 wt% TMGMV addition. TMGMV as a reinforcing agent can be produced in large quantities with molecular farming, and its manufacture is a positive contributor to the environment, rather than non-biological nanofillers. In the context of biocompatibility and safety, TMGMV also possess outstanding merits over non-biological nanofillers. This study serves evidence to the development of hydrophilic nanofillers made from viral particles.

In Chapter 2, we investigated the potential of HME for sustained delivery route manufacturing. In this study, we studied its capabilities for both protein therapeutics and small molecule drugs. Unfortunately, its application for protein therapeutics might still limited by the types of proteins, and further studies should be implemented to address this concern. For small molecule drugs, HME shows great potential in manufacturing sustained delivery devices. We performed a non-invasive

surgery for the device implantation on the murine B16F10 model, and the device shows outstanding efficacy compared with weekly injections (3x). This pioneer research finding provides solid evidence for sustained anti-tumor drug delivery, and feasibility of HME in different drug delivery route fabrication.

In Chapter 3, we described a streamlined method to produce eCPMV from native CPMV with a simple experimental setup and low demands for equipment and materials. A simple freeze-drying procedure ejected the RNA from the capsid, and RNase treatment was able to degrade the remaining nucleic acids to produce lyo-eCPMV. A series of characterization methods were carried out to show that the empty capsids maintained an intact capsid conformation. Furthermore, in situ injection of lyo-eCPMV was observed to have similar efficacy in tumor suppression as bacterially derived eCPMV. In sum, we present a straightforward method for the rapid production of eCPMV from native infectious CPMV. From this study, we propose to further utilize this physical method to develop the next generation vaccination derived directly from the wild type viruses.

In Chapter 4, we introduced a coagulation-bath assisted DIW technique to fabricate high-resolution, high conductivity and stable electrochemical PEDOT:PSS structures. This technique comes with several advantages that include a simple experimental setup and inexpensive printing hardware. The reported printing technique allows for several modifications to the resultant PEDOT:PSS material by simple modification of the bath chemistry. With a simple postprocessing method, the prints demonstrated excellent substrate adhesion, and further postprocessing (such as flow coating, multi-material 3D printing, chemical modification, etc.) can be applied to the prints to further broaden the use of the material, especially in the field of bioelectronics. As a demonstration, we fabricated a cortex-wide neural interface, and recorded the optical and physical response of electrical stimulation as well as simultaneous full-field monitoring with a printed

PEDOT:PSS electrode array. Furthermore. this work establishes a new 3D printing technique for polymer processing, demonstrating the capability and versatility of DIW as a simultaneous physical and chemical patterning method to achieve favorable macro- and microstructural features laying the road for future development of DIW in the field of material design and synthesis.

5.2 Outlook for future work

Polymers have great versatility and flexibility in a broad range of application scenarios. We here have demonstrated several innovations from the fundamental level of polymer selection and design to meet desired materials' properties, to the application level of processing and fabrication of the selected polymers and formulation design to manufacturing biomedical devices. We have shown the potential of polymer engineering methods to bridge materials science and biology.

5.2.1 Intersection at VNPs polymer composite and bioelectronics

In the thesis, we incorporated viral nanoparticles in the polymeric substrate and fabricated a sustained CPMV release device and TMGMV-strengthened hydrogel system. In a word, we developed the interface between materials science and molecular biology (VNPs) and resulting in a stable polymeric system to embed viral nanoparticles and realize desired functionalities. In my third- and fourth-year study at Zhou lab as a visiting student, I developed my knowledge of bioelectronics. Therefore, a bioelectronic system based on the stable polymeric system empowered by viral nanoparticles can be further developed to present my understanding of the multidisciplinary study from my special Ph.D. experience.

One such bioelectronic system could be a wireless theragnostic contact lens for cancer immunotherapy with VNPs controlled release system. Nature Publishing Group[220,221] has reported the cutting-edge wireless theragnostic contact lens recently; APIs for eye diseases can be preloaded in the lenses and the built-in circuit system will control the slow release profile of the loaded APIs. Particularly, the nanosystem-APIs are desired, because nanosystems will increase the drug

retention time on the ocular surface and improve the drug penetration against the corneal barrier and pre-corneal factors.[222] The APIs pre-loaded contact lenses are preferred over eye drops because they are single-treatment and eliminate the side effects of glaucoma, cataracts, and poor patient compliance caused by repeated treatment of eye drops. [223] A VNPs- empowered wireless contact lenses can be potentially developed to realize self-applied cancer treatment by patients themselves. VNP-associated cancer treatments have been extensively studied by the Steinmetz group[224] in the form of anti-tumor molecules delivery nanoparticles, immunotherapy realized by the VNPs themselves, and targeting treatment by surface-modified VNPs. The delivery of VNPs from contact lenses to the bloodstream may be realized by the transportation of vitreous humor via the blood-retinal barrier.[225] The goal of the proposed idea is the elimination of in-person doctor appointments for cancer treatment. Due to the simplicity of contact lenses wearing, and smart-phone enabled wireless management, the scheduled treatments can be monitored by patients through the smartphone as administered by the doctor. Similarly, VNPs can also be incorporated into skin-inspired bioelectronics for a range of applications, such as wirelessly controllable skin patch treatments for melanoma and other types of skin diseases, such as psoriasis.[226]

5.2.2 Thoughts on lyophilization-induced genomic material elimination for a new type of vaccine

Another important research finding worth considering further development is the genomic material elimination by lyophilization. This finding might serve for the development of a new type of vaccination based on the immunization mechanism of coat protein-associated immunity recognitions.[227] Due to the removal of genomic material, this type of vaccination has little safety concern while the coat protein from wild-type viruses may elicit strong immunological memory. Lyophilization of the vaccination will also provide the advantage of sustainable transportation due to the need for a cold chain.

5.2.3 Efforts on sustained protein delivery manufactured by HME

Although the great finding of lyophilization-induced virus-like particles manufacturing, efforts are needed to protect VNPs from the damage caused by lyophilization. In chapter 3, we discussed the feasibility of HME in producing sustained CPMV delivery implants, but unfortunately, we found the particles experienced severe segregation and aggregation during the process. To fully study the potential of HME in developing sustained protein delivery implants, developments contributing to insulating the proteins from external conditions may be a good research topic.[20] The simplicity of the method and the processability of the resultant material are important factors to consider. Another effort could be the self-assembling properties of the VNPs. Molecules that can stimulate the self-assembly of the VNPs[228] can be incorporated into the implant system and the released protein subunits may undergo self-assembly *in vivo*.

This thesis focuses mainly on the processing of polymers and formulation science on the development of sustained protein delivery manufactured by HME; however, the development of low-melting processable polymers can also be a focus to enable the potential of HME in manufacturing sustained protein delivery implants.

5.2.3.1 Baroplastics as low-temperature polymer substrates

Baroplastics as mentioned beforehand are a type of pressure-sensitive polymer and can be processed under low temperatures when under applied pressure. Baroplastics consist of low-glass-transition-temperature (T_g) and high-glass-transition-temperature (T_g) components in the form of core-shell polymer or block copolymer or nanoblends.[229] Recently, a novel type of biodegradable baroplastic comprising polyphosphoester and poly(l-lactide) (PLLA), PIPPx-b-PLLAy block copolymers have been investigated, and proteinase K was incorporated in the system. Full enzymatic activity of proteinase K was obtained after processing under ambient temperature with

a pressure of 5076 psi[230] (Figure 5b). Another work done by Z. Lv et al.[231] synthesized a poly(n-butyl acrylate)@polystyrene (PBA@PS) core–shell polymer and reinforced the baroplastic by mixing with poly(acrylic acid) and poly(ethylene oxide) through hydrogen-bonded interaction. The resultant polymer is processable by compression molding under 1450 psi at room temperature for 10 min. This pressure is roughly in the range of the pressure inside the extruder barrel during the extrusion process, which generally ranges between 1000 and 5000 psi[232], indicating a great potential for the use of baroplastics in the low-temperature HME process.

5.2.3.2 Proteins non-covalently bond with fluoropolymers

Fluoropolymers, a type of interesting polymer, could bring tremendous opportunities for unmet biomedical applications. Fluoropolymers have long been known for their strong chemical resistance, low surface energy, excellent mechanical properties, and high stability. Examples of the most common fluoropolymers are poly(vinyl fluoride) (PVF), poly(tetrafluoroethylene) (PTFE), poly(vinylidene fluoride) (PVDF), poly(chlorotrifluoroethylene) (PCTFE), they have been widely used in automotive, chemical, electrical, semiconductor industry, and medical industry.[233] However, the clinical application in the medical industry is limited to cardiovascular grafts based on PTFE and Dacron®.[234] The application of fluoropolymers in the drug delivery field is still relatively new, however, fluoropolymers can contribute to several advantages because of their superior assembly ability, serum tolerance, cellular uptake efficiency, endosomal escape efficiency, and reduced cytotoxicity, and have arisen increasing attention. Fluoropolymers showed great promise in biomacromolecule delivery, and improved gene delivery by increased gene transfection efficiency is achieved by fluoropolymers assemblies nanoparticles.[235,236] For protein/peptide delivery, fluoropolymers have played a vital role in the formation of nanoparticles with proteins/ peptides, avoiding protein denaturation, and maintaining bioactivity for protein

delivery.[237,238] Furthermore, the length of the fluorous chains and the fluoridation rate can regulate the delivery efficacy of the protein therapy.[239] The main hindrance of fluoropolymers in drug delivery is the incapability of the degradation and metabolism of fluoropolymers *in vivo* due to the inexistence of natural fluorine metabolic enzymes, however, stimulus-responsive bonds such as disulfide bonds, [236] are introduced into the back chain; polypeptides,[240] and PLA[241] can be used as the main chain to branch with fluoropolymers, and realize biodegradable fluoropolymers.

Based on the advantages of the fluoropolymers, I propose a biodegradable fluoropolymer that non-covalently binds with protein to shield it from the stress caused by HME. Together with the protein APIs, gene therapy can also be incorporated into the fluoropolymer chains and act as an adjuvant for the protein treatment.

5.2.4 Innovations related to hydrogels

Hydrogels are a group of powerful materials used in biomedical applications as we discussed in Chapter 1 and Chapter 4. For the future investigation of hydrogels, "living" materials can be a promising direction. As reported by Liu et al.,[86] genetically targeted chemical assembly of conductive polymers are synthesized in living cells and the 3D printed living responsive materials and devices[27] suggests hydrogels are necessary substrates to culture the living cells, and also they can bridge the living cells and human body. Not only merely as a substrate, hydrogels can also be modified in structure to react to external stimuli, such as polymer blocks having a mechanical response. An interesting application could be a stem cell-incorporated mechanically responsive hydrogel used for tissue regeneration. The hydrogel first acts as an extracellular matrix (ECM) to maintain cell growth and supply essential components to cells, and also serves as the substitute for damaged large-size tissue.[242] Later, the hydrogel will gradually degrade activated by the

mechanically responsive blocks caused by the regeneration of tissues, and lead to complete tissue regeneration.

5.2.5 Polymer processing techniques- enabled materials development

In the thesis, polymer processing techniques, such as HME and 3D printing, were utilized to fabricate drug delivery devices and bioelectronics. However, they can be a part of the materials design and modify and even synthesize the processed/ designed materials. As we suggested in Chapter 4, a DBSA coagulation was added to the system and realized an *in situ* formation of 3D printable PEDOT. Reactive melt extrusion has been reported to improve the dissolution performance and physical stability of naproxen ASDs[243]. Therefore, an interesting project could be a reactive material system processed with strain-induced alignment from HME and followed by coagulation bath-assisted material modification.

In conclusion, polymer science in biomedical applications is a highly multidisciplinary subject. It requires input from various fields to present cutting-edge polymeric integrations. More importantly, the communication between academic research and clinical professionals and biotech corporations is essential to inspire innovations as well as to accelerate translational research to realize enhanced research and development efficiency and reach the goal of increased human health and improved living quality.

REFERENCES

(1) *polymer | Description, Examples, Types, Material, Uses, & Facts | Britannica*. https://www.britannica.com/science/polymer (accessed 2022-08-25).

(2) Ekebafe, L. O.; Ogbeifun, D. E.; Okieimen, F. E. Polymer Applications in Agriculture. *Biokemistri* **2011**, *23* (2). https://doi.org/10.4314/biokem.v23i2.

(3) *Polymer Applications*. https://www.intertek.com/polymers/applications/ (accessed 2022-08-25).

(4) *Biomedical Research Funding*. https://www.endocrine.org/advocacy/position-statements/biomedical-research-funding (accessed 2022-08-25).

(5) Nietzel, M. T. *The 19 U.S. Universities Spending $1 Billion Or More On R And D*. Forbes. https://www.forbes.com/sites/michaeltnietzel/2021/02/08/the-19-us-universities-spending-one-billion-or-more-on-r-and-d/ (accessed 2022-08-25).

(6) Premkumar, J.; SonicaSree, K.; Sudhakar, T. Polymers in Biomedical Use. In *Handbook of Polymer and Ceramic Nanotechnology*; Hussain, C. M., Thomas, S., Eds.; Springer International Publishing: Cham, 2020; pp 1–28. https://doi.org/10.1007/978-3-030-10614-0_74-1.

(7) Liechty, W. B.; Kryscio, D. R.; Slaughter, B. V.; Peppas, N. A. Polymers for Drug Delivery Systems. *Annu. Rev. Chem. Biomol. Eng.* **2010**, *1*, 149–173. https://doi.org/10.1146/annurev-chembioeng-073009-100847.

(8) Wang, S.; Oh, J. Y.; Xu, J.; Tran, H.; Bao, Z. Skin-Inspired Electronics: An Emerging Paradigm. *Acc. Chem. Res.* **2018**, *51* (5), 1033–1045. https://doi.org/10.1021/acs.accounts.8b00015.

(9) Saha, S.; Mamun, K. A.; Ahmed, K.; Mostafa, R.; Naik, G. R.; Darvishi, S.; Khandoker, A. H.; Baumert, M. Progress in Brain Computer Interface: Challenges and Opportunities. *Front. Syst. Neurosci.* **2021**, *15*.

(10) The Soft Touch of Robots. *Nat. Rev. Mater.* **2018**, *3* (6), 71–71. https://doi.org/10.1038/s41578-018-0017-8.

(11) Pagga, U. Biodegradability and Compostability of Polymeric Materials in the Context of the European Packaging Regulation. *Polym. Degrad. Stab.* **1998**, *59* (1), 371–376. https://doi.org/10.1016/S0141-3910(97)00192-4.

(12) Ulery, B. D.; Nair, L. S.; Laurencin, C. T. Biomedical Applications of Biodegradable Polymers. *J. Polym. Sci. Part B Polym. Phys.* **2011**, *49* (12), 832–864. https://doi.org/10.1002/polb.22259.

(13) *Poly(lactic acid): Synthesis, Structures, Properties, Processing, Applications, and End of Life, 2nd Edition | Wiley*. https://www.wiley.com/en-us/Poly(lactic+acid):+Synthesis,+Structures,+Properties,+Processing,+Applications,+and+End+of+Life,+2nd+Edition-p-9781119767442 (accessed 2022-12-03).

(14) Gunatillake, P. A.; Adhikari, R. 2 - Nondegradable Synthetic Polymers for Medical Devices and Implants. In *Biosynthetic Polymers for Medical Applications*; Poole-Warren, L., Martens, P., Green, R., Eds.; Woodhead Publishing Series in Biomaterials; Woodhead Publishing, 2016; pp 33–62. https://doi.org/10.1016/B978-1-78242-105-4.00002-X.

(15) Allyn, M. M.; Luo, R. H.; Hellwarth, E. B.; Swindle-Reilly, K. E. Considerations for Polymers Used in Ocular Drug Delivery. *Front. Med.* **2022**, *8*.

(16) Rasmussen, S. C. 2000 Nobel Prize in Chemistry. In *Acetylene and Its Polymers: 150+ Years of History*; Rasmussen, S. C., Ed.; SpringerBriefs in Molecular Science; Springer

International Publishing: Cham, 2018; pp 125–132. https://doi.org/10.1007/978-3-319-95489-9_7.
(17) Nezakati, T.; Seifalian, A.; Tan, A.; Seifalian, A. M. Conductive Polymers: Opportunities and Challenges in Biomedical Applications. *Chem. Rev.* **2018**, *118* (14), 6766–6843. https://doi.org/10.1021/acs.chemrev.6b00275.
(18) Wang, Y.; Zhu, C.; Pfattner, R.; Yan, H.; Jin, L.; Chen, S.; Molina-Lopez, F.; Lissel, F.; Liu, J.; Rabiah, N. I.; Chen, Z.; Chung, J. W.; Linder, C.; Toney, M. F.; Murmann, B.; Bao, Z. A Highly Stretchable, Transparent, and Conductive Polymer. *Sci. Adv.* **2017**, *3* (3), e1602076. https://doi.org/10.1126/sciadv.1602076.
(19) Zia, K. M.; Akram, N.; Tabasum, S.; Noreen, A.; Akbar, M. U. 6 - Processing of Bio-Based Polymers for Industrial and Medical Applications. In *Processing Technology for Bio-Based Polymers*; Zia, K. M., Akram, N., Tabasum, S., Noreen, A., Akbar, M. U., Eds.; Elsevier, 2021; pp 191–238. https://doi.org/10.1016/B978-0-323-85772-7.00006-9.
(20) Zheng, Y.; Pokorski, J. K. Hot Melt Extrusion: An Emerging Manufacturing Method for Slow and Sustained Protein Delivery. *WIREs Nanomedicine Nanobiotechnology* **2021**, *13* (5), e1712. https://doi.org/10.1002/wnan.1712.
(21) Ligon, S. C.; Liska, R.; Stampfl, J.; Gurr, M.; Mülhaupt, R. Polymers for 3D Printing and Customized Additive Manufacturing. *Chem. Rev.* **2017**, *117* (15), 10212–10290. https://doi.org/10.1021/acs.chemrev.7b00074.
(22) Zhu, W.; Qu, X.; Zhu, J.; Ma, X.; Patel, S.; Liu, J.; Wang, P.; Lai, C. S. E.; Gou, M.; Xu, Y.; Zhang, K.; Chen, S. Direct 3D Bioprinting of Prevascularized Tissue Constructs with Complex Microarchitecture. *Biomaterials* **2017**, *124*, 106–115. https://doi.org/10.1016/j.biomaterials.2017.01.042.
(23) Gauvin, R.; Chen, Y.-C.; Lee, J. W.; Soman, P.; Zorlutuna, P.; Nichol, J. W.; Bae, H.; Chen, S.; Khademhosseini, A. Microfabrication of Complex Porous Tissue Engineering Scaffolds Using 3D Projection Stereolithography. *Biomaterials* **2012**, *33* (15), 3824–3834. https://doi.org/10.1016/j.biomaterials.2012.01.048.
(24) Guan, J.; You, S.; Xiang, Y.; Schimelman, J.; Alido, J.; Ma, X.; Tang, M.; Chen, S. Compensating the Cell-Induced Light Scattering Effect in Light-Based Bioprinting Using Deep Learning. *Biofabrication* **2021**, *14* (1), 015011. https://doi.org/10.1088/1758-5090/ac3b92.
(25) Bozkurt, Y.; Karayel, E. 3D Printing Technology; Methods, Biomedical Applications, Future Opportunities and Trends. *J. Mater. Res. Technol.* **2021**, *14*, 1430–1450. https://doi.org/10.1016/j.jmrt.2021.07.050.
(26) Mannoor, M. S.; Jiang, Z.; James, T.; Kong, Y. L.; Malatesta, K. A.; Soboyejo, W. O.; Verma, N.; Gracias, D. H.; McAlpine, M. C. 3D Printed Bionic Ears. *Nano Lett.* **2013**, *13* (6), 2634–2639. https://doi.org/10.1021/nl4007744.
(27) Liu, X.; Yuk, H.; Lin, S.; Parada, G. A.; Tang, T.-C.; Tham, E.; de la Fuente-Nunez, C.; Lu, T. K.; Zhao, X. 3D Printing of Living Responsive Materials and Devices. *Adv. Mater.* **2018**, *30* (4), 1704821. https://doi.org/10.1002/adma.201704821.
(28) He, Q.; Wang, Z.; Song, Z.; Cai, S. Bioinspired Design of Vascular Artificial Muscle. *Adv. Mater. Technol.* **2019**, *4* (1), 1800244. https://doi.org/10.1002/admt.201800244.
(29) Perrone, G. S.; Leisk, G. G.; Lo, T. J.; Moreau, J. E.; Haas, D. S.; Papenburg, B. J.; Golden, E. B.; Partlow, B. P.; Fox, S. E.; Ibrahim, A. M. S.; Lin, S. J.; Kaplan, D. L. The Use of Silk-Based Devices for Fracture Fixation. *Nat. Commun.* **2014**, *5* (1), 3385. https://doi.org/10.1038/ncomms4385.

(30) Childs, A.; Li, H.; Lewittes, D. M.; Dong, B.; Liu, W.; Shu, X.; Sun, C.; Zhang, H. F. Fabricating Customized Hydrogel Contact Lens. *Sci. Rep.* **2016**, *6* (1), 34905. https://doi.org/10.1038/srep34905.
(31) Crunkhorn, S. Star-Shaped Pill Sustains Drug Release. *Nat. Rev. Drug Discov.* **2017**, *16* (1), 16–16. https://doi.org/10.1038/nrd.2016.273.
(32) Hopmann, C.; Adamy, M.; Cohnen, A. Introduction to Reactive Extrusion. In *Reactive Extrusion*; John Wiley & Sons, Ltd, 2017; pp 1–10. https://doi.org/10.1002/9783527801541.ch1.
(33) Erratum. *Nat. Mater.* **2003**, *2* (5), 347–347. https://doi.org/10.1038/nmat881.
(34) Chai, Q.; Jiao, Y.; Yu, X. Hydrogels for Biomedical Applications: Their Characteristics and the Mechanisms behind Them. *Gels* **2017**, *3* (1), 6. https://doi.org/10.3390/gels3010006.
(35) Ji, D.; Kim, J. Recent Strategies for Strengthening and Stiffening Tough Hydrogels. *Adv. NanoBiomed Res.* **2021**, *1* (8), 2100026. https://doi.org/10.1002/anbr.202100026.
(36) Zaragoza, J.; Fukuoka, S.; Kraus, M.; Thomin, J.; Asuri, P. Exploring the Role of Nanoparticles in Enhancing Mechanical Properties of Hydrogel Nanocomposites. *Nanomaterials* **2018**, *8* (11), 882. https://doi.org/10.3390/nano8110882.
(37) Stando, G.; Łukawski, D.; Lisiecki, F.; Janas, D. Intrinsic Hydrophilic Character of Carbon Nanotube Networks. *Appl. Surf. Sci.* **2019**, *463*, 227–233. https://doi.org/10.1016/j.apsusc.2018.08.206.
(38) Sung, Y. K.; Kim, S. W. Recent Advances in Polymeric Drug Delivery Systems. *Biomater. Res.* **2020**, *24* (1), 12. https://doi.org/10.1186/s40824-020-00190-7.
(39) Church, D. C.; Pokorski, J. K. Cell Engineering with Functional Poly(Oxanorbornene) Block Copolymers. *Angew. Chem.* **2020**, *132* (28), 11475–11479. https://doi.org/10.1002/ange.202005148.
(40) Lôbo, G. C. N. B.; Paiva, K. L. R.; Silva, A. L. G.; Simões, M. M.; Radicchi, M. A.; Báo, S. N. Nanocarriers Used in Drug Delivery to Enhance Immune System in Cancer Therapy. *Pharmaceutics* **2021**, *13* (8), 1167. https://doi.org/10.3390/pharmaceutics13081167.
(41) *Investigating the Side Effects of Cancer Immunotherapy - NCI*. https://www.cancer.gov/news-events/cancer-currents-blog/2019/cancer-immunotherapy-investigating-side-effects (accessed 2022-11-28).
(42) Dychter, S. S.; Gold, D. A.; Carson, D.; Haller, M. Intravenous Therapy: A Review of Complications and Economic Considerations of Peripheral Access. *J. Infus. Nurs.* **2012**, *35* (2), 84–91. https://doi.org/10.1097/NAN.0b013e31824237ce.
(43) *Trypanophobia (Fear of Needles): Symptoms & Treatment*. https://my.clevelandclinic.org/health/diseases/22731-trypanophobia-fear-of-needles (accessed 2022-12-03).
(44) Stewart, S. A.; Domínguez-Robles, J.; Donnelly, R. F.; Larrañeta, E. Implantable Polymeric Drug Delivery Devices: Classification, Manufacture, Materials, and Clinical Applications. *Polymers* **2018**, *10* (12), 1379. https://doi.org/10.3390/polym10121379.
(45) Orive, G.; Taebnia, N.; Dolatshahi-Pirouz, A. A New Era for Cyborg Science Is Emerging: The Promise of Cyborganic Beings. *Adv. Healthc. Mater.* **2020**, *9* (1), 1901023. https://doi.org/10.1002/adhm.201901023.
(46) Malliaras, G.; McCulloch, I. Introduction: Organic Bioelectronics. *Chem. Rev.* **2022**, *122* (4), 4323–4324. https://doi.org/10.1021/acs.chemrev.2c00026.

(47) *Bioelectronics Engineering » Electrical and Computer Engineering*. https://ece.ncsu.edu/research/bee/ (accessed 2022-12-03).
(48) Yuk, H.; Wu, J.; Zhao, X. Hydrogel Interfaces for Merging Humans and Machines. *Nat. Rev. Mater.* **2022**, *7* (12), 935–952. https://doi.org/10.1038/s41578-022-00483-4.
(49) Wang, M.; Yang, Y.; Min, J.; Song, Y.; Tu, J.; Mukasa, D.; Ye, C.; Xu, C.; Heflin, N.; McCune, J. S.; Hsiai, T. K.; Li, Z.; Gao, W. A Wearable Electrochemical Biosensor for the Monitoring of Metabolites and Nutrients. *Nat. Biomed. Eng.* **2022**, *6* (11), 1225–1235. https://doi.org/10.1038/s41551-022-00916-z.
(50) Song, E.; Xie, Z.; Bai, W.; Luan, H.; Ji, B.; Ning, X.; Xia, Y.; Baek, J. M.; Lee, Y.; Avila, R.; Chen, H.-Y.; Kim, J.-H.; Madhvapathy, S.; Yao, K.; Li, D.; Zhou, J.; Han, M.; Won, S. M.; Zhang, X.; Myers, D. J.; Mei, Y.; Guo, X.; Xu, S.; Chang, J.-K.; Yu, X.; Huang, Y.; Rogers, J. A. Miniaturized Electromechanical Devices for the Characterization of the Biomechanics of Deep Tissue. *Nat. Biomed. Eng.* **2021**, *5* (7), 759–771. https://doi.org/10.1038/s41551-021-00723-y.
(51) Armstrong, A. G.; Lam, C. C.; Sabesan, S.; Lesica, N. A. Compression and Amplification Algorithms in Hearing Aids Impair the Selectivity of Neural Responses to Speech. *Nat. Biomed. Eng.* **2022**, *6* (6), 717–730. https://doi.org/10.1038/s41551-021-00707-y.
(52) Han, M.; Chen, L.; Aras, K.; Liang, C.; Chen, X.; Zhao, H.; Li, K.; Faye, N. R.; Sun, B.; Kim, J.-H.; Bai, W.; Yang, Q.; Ma, Y.; Lu, W.; Song, E.; Baek, J. M.; Lee, Y.; Liu, C.; Model, J. B.; Yang, G.; Ghaffari, R.; Huang, Y.; Efimov, I. R.; Rogers, J. A. Catheter-Integrated Soft Multilayer Electronic Arrays for Multiplexed Sensing and Actuation during Cardiac Surgery. *Nat. Biomed. Eng.* **2020**, *4* (10), 997–1009. https://doi.org/10.1038/s41551-020-00604-w.
(53) Tian, L.; Zimmerman, B.; Akhtar, A.; Yu, K. J.; Moore, M.; Wu, J.; Larsen, R. J.; Lee, J. W.; Li, J.; Liu, Y.; Metzger, B.; Qu, S.; Guo, X.; Mathewson, K. E.; Fan, J. A.; Cornman, J.; Fatina, M.; Xie, Z.; Ma, Y.; Zhang, J.; Zhang, Y.; Dolcos, F.; Fabiani, M.; Gratton, G.; Bretl, T.; Hargrove, L. J.; Braun, P. V.; Huang, Y.; Rogers, J. A. Large-Area MRI-Compatible Epidermal Electronic Interfaces for Prosthetic Control and Cognitive Monitoring. *Nat. Biomed. Eng.* **2019**, *3* (3), 194–205. https://doi.org/10.1038/s41551-019-0347-x.
(54) Liu, Y.; Liu, J.; Chen, S.; Lei, T.; Kim, Y.; Niu, S.; Wang, H.; Wang, X.; Foudeh, A. M.; Tok, J. B.-H.; Bao, Z. Soft and Elastic Hydrogel-Based Microelectronics for Localized Low-Voltage Neuromodulation. *Nat. Biomed. Eng.* **2019**, *3* (1), 58–68. https://doi.org/10.1038/s41551-018-0335-6.
(55) Yuk, H.; Lu, B.; Zhao, X. Hydrogel Bioelectronics. *Chem. Soc. Rev.* **2019**, *48* (6), 1642–1667. https://doi.org/10.1039/C8CS00595H.
(56) Gaharwar, A. K.; Peppas, N. A.; Khademhosseini, A. Nanocomposite Hydrogels for Biomedical Applications. *Biotechnol. Bioeng.* **2014**, *111* (3), 441–453. https://doi.org/10.1002/bit.25160.
(57) Peppas, N. A.; Hilt, J. Z.; Khademhosseini, A.; Langer, R. Hydrogels in Biology and Medicine: From Molecular Principles to Bionanotechnology. *Adv. Mater.* **2006**, *18* (11), 1345–1360. https://doi.org/10.1002/adma.200501612.
(58) Jhon, M. S.; Andrade, J. D. Water and Hydrogels. *J. Biomed. Mater. Res.* **1973**, *7* (6), 509–522. https://doi.org/10.1002/jbm.820070604.
(59) Peppas, N. A.; Bures, P.; Leobandung, W.; Ichikawa, H. Hydrogels in Pharmaceutical Formulations. *Eur. J. Pharm. Biopharm. Off. J. Arbeitsgemeinschaft Pharm.*

Verfahrenstechnik EV **2000**, *50* (1), 27–46. https://doi.org/10.1016/s0939-6411(00)00090-4.
(60) Li, X.; Yang, Y.; Fan, Y.; Feng, Q.; Cui, F.; Watari, F. Biocomposites Reinforced by Fibers or Tubes as Scaffolds for Tissue Engineering or Regenerative Medicine. *J. Biomed. Mater. Res. A* **2014**, *102* (5), 1580–1594. https://doi.org/10.1002/jbm.a.34801.
(61) Hernández, R. M.; Orive, G.; Murua, A.; Pedraz, J. L. Microcapsules and Microcarriers for in Situ Cell Delivery. *Adv. Drug Deliv. Rev.* **2010**, *62* (7), 711–730. https://doi.org/10.1016/j.addr.2010.02.004.
(62) Peak, C. W.; Wilker, J. J.; Schmidt, G. A Review on Tough and Sticky Hydrogels. *Colloid Polym. Sci.* **2013**, *291* (9), 2031–2047. https://doi.org/10.1007/s00396-013-3021-y.
(63) Maldonado-Codina, C.; Efron, N. Impact of Manufacturing Technology and Material Composition on the Mechanical Properties of Hydrogel Contact Lenses. *Ophthalmic Physiol. Opt. J. Br. Coll. Ophthalmic Opt. Optom.* **2004**, *24* (6), 551–561. https://doi.org/10.1111/j.1475-1313.2004.00236.x.
(64) Tanaka, Y.; Gong, J. P.; Osada, Y. Novel hydrogels with excellent mechanical performance. *Prog. Polym. Sci.* **2005**, *30* (1), 1–9. https://doi.org/10.1016/j.progpolymsci.2004.11.003.
(65) McCullen, S. D.; Haslauer, C. M.; Loboa, E. G. Fiber-Reinforced Scaffolds for Tissue Engineering and Regenerative Medicine: Use of Traditional Textile Substrates to Nanofibrous Arrays. *J. Mater. Chem.* **2010**, *20* (40), 8776–8788. https://doi.org/10.1039/C0JM01443E.
(66) Butcher, A. L.; Offeddu, G. S.; Oyen, M. L. Nanofibrous Hydrogel Composites as Mechanically Robust Tissue Engineering Scaffolds. *Trends Biotechnol.* **2014**, *32* (11), 564–570. https://doi.org/10.1016/j.tibtech.2014.09.001.
(67) Schadler, L. S.; Giannaris, S. C.; Ajayan, P. M. Load Transfer in Carbon Nanotube Epoxy Composites. *Appl. Phys. Lett.* **1998**, *73* (26), 3842–3844. https://doi.org/10.1063/1.122911.
(68) Treacy, M. M. J.; Ebbesen, T. W.; Gibson, J. M. Exceptionally High Young's Modulus Observed for Individual Carbon Nanotubes. *Nature* **1996**, *381* (6584), 678–680. https://doi.org/10.1038/381678a0.
(69) Xie, X.-L.; Mai, Y.-W.; Zhou, X.-P. Dispersion and Alignment of Carbon Nanotubes in Polymer Matrix: A Review. *Mater. Sci. Eng. R Rep.* **2005**, *49* (4), 89–112. https://doi.org/10.1016/j.mser.2005.04.002.
(70) Lu, J. P. Elastic Properties of Carbon Nanotubes and Nanoropes. *Phys. Rev. Lett.* **1997**, *79* (7), 1297–1300. https://doi.org/10.1103/PhysRevLett.79.1297.
(71) Buyukozturk, O.; Hearing, B. Crack Propagation in Concrete Composites Influenced by Interface Fracture Parameters. *Int. J. Solids Struct.* **1998**, *35* (31), 4055–4066. https://doi.org/10.1016/S0020-7683(97)00300-4.
(72) Thostenson, E. T.; Ren, Z.; Chou, T.-W. Advances in the Science and Technology of Carbon Nanotubes and Their Composites: A Review. *Compos. Sci. Technol.* **2001**, *61* (13), 1899–1912. https://doi.org/10.1016/S0266-3538(01)00094-X.
(73) Subramaniam, K.; Das, A.; Heinrich, G. Development of Conducting Polychloroprene Rubber Using Imidazolium Based Ionic Liquid Modified Multi-Walled Carbon Nanotubes. *Compos. Sci. Technol.* **2011**, *71* (11), 1441–1449. https://doi.org/10.1016/j.compscitech.2011.05.018.

(74) Tuncel, D. Non-Covalent Interactions between Carbon Nanotubes and Conjugated Polymers. *Nanoscale* **2011**, *3* (9), 3545–3554. https://doi.org/10.1039/C1NR10338E.
(75) Bahr, J. L.; Tour, J. M. Covalent Chemistry of Single-Wall Carbon Nanotubes. *J. Mater. Chem.* **2002**, *12* (7), 1952–1958. https://doi.org/10.1039/B201013P.
(76) Habibi, Y.; Lucia, L. A.; Rojas, O. J. Cellulose Nanocrystals: Chemistry, Self-Assembly, and Applications. *Chem. Rev.* **2010**, *110* (6), 3479–3500. https://doi.org/10.1021/cr900339w.
(77) Eyholzer, Ch.; Lopez-Suevos, F.; Tingaut, P.; Zimmermann, T.; Oksman, K. Reinforcing Effect of Carboxymethylated Nanofibrillated Cellulose Powder on Hydroxypropyl Cellulose. *Cellulose* **2010**, *17* (4), 793–802. https://doi.org/10.1007/s10570-010-9423-9.
(78) Fraile, A.; García-Arenal, F. 1990. A Classification of the Tobamoviruses Based on Comparisons among Their 126K Proteins. *J. Gen. Virol. 71* (10), 2223–2228. https://doi.org/10.1099/0022-1317-71-10-2223.
(79) Chariou, P. L.; Steinmetz, N. F. Delivery of Pesticides to Plant Parasitic Nematodes Using Tobacco Mild Green Mosaic Virus as a Nanocarrier. *ACS Nano* **2017**, *11* (5), 4719–4730. https://doi.org/10.1021/acsnano.7b00823.
(80) Baker, C. A.; Zettler, F. W. Viruses Infecting Wild and Cultivated Species of the Commelinaceae. *Plant Dis. USA* **1988**.
(81) Regenmortel, M. H. V. V.; Fraenkel-Conrat, H. *The Plant Viruses: The Rod-Shaped Plant Viruses*; Springer Science & Business Media, 2013.
(82) Falvo, M. R.; Washburn, S.; Superfine, R.; Finch, M.; Brooks, F. P.; Chi, V.; Taylor, R. M. Manipulation of Individual Viruses: Friction and Mechanical Properties. *Biophys. J.* **1997**, *72* (3), 1396–1403. https://doi.org/10.1016/S0006-3495(97)78786-1.
(83) Zhao, Y.; Ge, Z.; Fang, J. Elastic Modulus of Viral Nanotubes. *Phys. Rev. E Stat. Nonlin. Soft Matter Phys.* **2008**, *78* (3 Pt 1), 031914. https://doi.org/10.1103/PhysRevE.78.031914.
(84) Pokorski, J. K.; Breitenkamp, K.; Liepold, L. O.; Qazi, S.; Finn, M. G. Functional Virus-Based Polymer–Protein Nanoparticles by Atom Transfer Radical Polymerization. *J. Am. Chem. Soc.* **2011**, *133* (24), 9242–9245. https://doi.org/10.1021/ja203286n.
(85) Chen, L.; Zhao, X.; Lin, Y.; Su, Z.; Wang, Q. Dual Stimuli-Responsive Supramolecular Hydrogel of Bionanoparticles and Hyaluronan. *Polym. Chem.* **2014**, *5* (23), 6754–6760. https://doi.org/10.1039/C4PY00819G.
(86) Liu, J.; Kim, Y. S.; Richardson, C. E.; Tom, A.; Ramakrishnan, C.; Birey, F.; Katsumata, T.; Chen, S.; Wang, C.; Wang, X.; Joubert, L.-M.; Jiang, Y.; Wang, H.; Fenno, L. E.; Tok, J. B.-H.; Paşca, S. P.; Shen, K.; Bao, Z.; Deisseroth, K. Genetically Targeted Chemical Assembly of Functional Materials in Living Cells, Tissues, and Animals. *Science* **2020**, *367* (6484), 1372–1376. https://doi.org/10.1126/science.aay4866.
(87) Luckanagul, J. A.; Lee, L. A.; You, S.; Yang, X.; Wang, Q. Plant Virus Incorporated Hydrogels as Scaffolds for Tissue Engineering Possess Low Immunogenicity in Vivo. *J. Biomed. Mater. Res. A* **2015**, *103* (3), 887–895. https://doi.org/10.1002/jbm.a.35227.
(88) Luckanagul, J.; Lee, L. A.; Nguyen, Q. L.; Sitasuwan, P.; Yang, X.; Shazly, T.; Wang, Q. Porous Alginate Hydrogel Functionalized with Virus as Three-Dimensional Scaffolds for Bone Differentiation. *Biomacromolecules* **2012**, *13* (12), 3949–3958. https://doi.org/10.1021/bm301180c.
(89) Luckanagul, J. A.; Metavarayuth, K.; Feng, S.; Maneesaay, P.; Clark, A. Y.; Yang, X.; García, A. J.; Wang, Q. Tobacco Mosaic Virus Functionalized Alginate Hydrogel

Scaffolds for Bone Regeneration in Rats with Cranial Defect. *ACS Biomater. Sci. Eng.* **2016**, *2* (4), 606–615. https://doi.org/10.1021/acsbiomaterials.5b00561.
(90) Lin, C.-C.; Anseth, K. S. PEG Hydrogels for the Controlled Release of Biomolecules in Regenerative Medicine. *Pharm. Res.* **2009**, *26* (3), 631–643. https://doi.org/10.1007/s11095-008-9801-2.
(91) Lin, C.-C.; Metters, A. T. Hydrogels in Controlled Release Formulations: Network Design and Mathematical Modeling. *Adv. Drug Deliv. Rev.* **2006**, *58* (12), 1379–1408. https://doi.org/10.1016/j.addr.2006.09.004.
(92) Boyer, C.; Bulmus, V.; Davis, T. P.; Ladmiral, V.; Liu, J.; Perrier, S. Bioapplications of RAFT Polymerization. *Chem. Rev.* **2009**, *109* (11), 5402–5436. https://doi.org/10.1021/cr9001403.
(93) *Viral Nanoparticles: Tools for Material Science and Biomedicine*. Routledge & CRC Press. https://www.routledge.com/Viral-Nanoparticles-Tools-for-Material-Science-and-Biomedicine/Steinmetz-Manchester/p/book/9789814267458 (accessed 2022-12-05).
(94) Shenton, W.; Douglas, T.; Young, M.; Stubbs, G.; Mann, S. Inorganic–Organic Nanotube Composites from Template Mineralization of Tobacco Mosaic Virus. *Adv. Mater.* **1999**, *11* (3), 253–256. https://doi.org/10.1002/(SICI)1521-4095(199903)11:3<253::AID-ADMA253>3.0.CO;2-7.
(95) Fujii, K.; Mochizuki, T.; Imoto, S.; Ukida, J.; Matsumoto, M. Investigation of the Stereoregularity of Poly(Vinyl Alcohol). *J. Polym. Sci. A* **1964**, *2* (5), 2327–2347. https://doi.org/10.1002/pol.1964.100020523.
(96) Cadek, M.; Coleman, J. N.; Ryan, K. P.; Nicolosi, V.; Bister, G.; Fonseca, A.; Nagy, J. B.; Szostak, K.; Béguin, F.; Blau, W. J. Reinforcement of Polymers with Carbon Nanotubes: The Role of Nanotube Surface Area. *Nano Lett.* **2004**, *4* (2), 353–356. https://doi.org/10.1021/nl035009o.
(97) Zhou, W. Y.; Guo, B.; Liu, M.; Liao, R.; Rabie, A. B. M.; Jia, D. Poly(Vinyl Alcohol)/Halloysite Nanotubes Bionanocomposite Films: Properties and in Vitro Osteoblasts and Fibroblasts Response. *J. Biomed. Mater. Res. A* **2010**, *93* (4), 1574–1587. https://doi.org/10.1002/jbm.a.32656.
(98) Kushnir, N.; Streatfield, S. J.; Yusibov, V. Virus-like Particles as a Highly Efficient Vaccine Platform: Diversity of Targets and Production Systems and Advances in Clinical Development. *Vaccine* **2012**, *31* (1), 58–83. https://doi.org/10.1016/j.vaccine.2012.10.083.
(99) Bogani, G.; Leone Roberti Maggiore, U.; Signorelli, M.; Martinelli, F.; Ditto, A.; Sabatucci, I.; Mosca, L.; Lorusso, D.; Raspagliesi, F. The Role of Human Papillomavirus Vaccines in Cervical Cancer: Prevention and Treatment. *Crit. Rev. Oncol. Hematol.* **2018**, *122*, 92–97. https://doi.org/10.1016/j.critrevonc.2017.12.017.
(100) Ogholikhan, S.; Schwarz, K. B. Hepatitis Vaccines. *Vaccines* **2016**, *4* (1), 6. https://doi.org/10.3390/vaccines4010006.
(101) Balke, I.; Zeltins, A. Use of Plant Viruses and Virus-like Particles for the Creation of Novel Vaccines. *Adv. Drug Deliv. Rev.* **2019**, *145*, 119–129. https://doi.org/10.1016/j.addr.2018.08.007.
(102) Bachmann, M. F.; Jennings, G. T. Vaccine Delivery: A Matter of Size, Geometry, Kinetics and Molecular Patterns. *Nat. Rev. Immunol.* **2010**, *10* (11), 787–796. https://doi.org/10.1038/nri2868.
(103) Clarke, B. E.; Newton, S. E.; Carroll, A. R.; Francis, M. J.; Appleyard, G.; Syred, A. D.; Highfield, P. E.; Rowlands, D. J.; Brown, F. Improved Immunogenicity of a Peptide

Epitope after Fusion to Hepatitis B Core Protein. *Nature* **1987**, *330* (6146), 381–384. https://doi.org/10.1038/330381a0.
(104) Hammerich, L.; Binder, A.; Brody, J. D. In Situ Vaccination: Cancer Immunotherapy Both Personalized and Off-the-shelf. *Mol. Oncol.* **2015**, *9* (10), 1966–1981. https://doi.org/10.1016/j.molonc.2015.10.016.
(105) Harrington, K. J.; Puzanov, I.; Hecht, J. R.; Hodi, F. S.; Szabo, Z.; Murugappan, S.; Kaufman, H. L. Clinical Development of Talimogene Laherparepvec (T-VEC): A Modified Herpes Simplex Virus Type-1–Derived Oncolytic Immunotherapy. *Expert Rev. Anticancer Ther.* **2015**, *15* (12), 1389–1403. https://doi.org/10.1586/14737140.2015.1115725.
(106) Bartlett, D. L.; Liu, Z.; Sathaiah, M.; Ravindranathan, R.; Guo, Z.; He, Y.; Guo, Z. S. Oncolytic Viruses as Therapeutic Cancer Vaccines. *Mol. Cancer* **2013**, *12* (1), 103. https://doi.org/10.1186/1476-4598-12-103.
(107) Chernajovsky, Y.; Layward, L.; Lemoine, N. Fighting Cancer with Oncolytic Viruses. *BMJ* **2006**, *332* (7534), 170–172. https://doi.org/10.1136/bmj.332.7534.170.
(108) Lebel, M.-È.; Chartrand, K.; Tarrab, E.; Savard, P.; Leclerc, D.; Lamarre, A. Potentiating Cancer Immunotherapy Using Papaya Mosaic Virus-Derived Nanoparticles. *Nano Lett.* **2016**, *16* (3), 1826–1832. https://doi.org/10.1021/acs.nanolett.5b04877.
(109) Lizotte, P. H.; Wen, A. M.; Sheen, M. R.; Fields, J.; Rojanasopondist, P.; Steinmetz, N. F.; Fiering, S. In Situ Vaccination with Cowpea Mosaic Virus Nanoparticles Suppresses Metastatic Cancer. *Nat. Nanotechnol.* **2016**, *11* (3), 295–303. https://doi.org/10.1038/nnano.2015.292.
(110) Murray, A. A.; Wang, C.; Fiering, S.; Steinmetz, N. F. In Situ Vaccination with Cowpea vs Tobacco Mosaic Virus against Melanoma. *Mol. Pharm.* **2018**, *15* (9), 3700–3716. https://doi.org/10.1021/acs.molpharmaceut.8b00316.
(111) Hoopes, P. J.; Wagner, R. J.; Duval, K.; Kang, K.; Gladstone, D. J.; Moodie, K. L.; Crary-Burney, M.; Ariaspulido, H.; Veliz, F. A.; Steinmetz, N. F.; Fiering, S. N. Treatment of Canine Oral Melanoma with Nanotechnology-Based Immunotherapy and Radiation. *Mol. Pharm.* **2018**, *15* (9), 3717–3722. https://doi.org/10.1021/acs.molpharmaceut.8b00126.
(112) Czapar, A. E.; Tiu, B. D. B.; Veliz, F. A.; Pokorski, J. K.; Steinmetz, N. F. Slow-Release Formulation of Cowpea Mosaic Virus for In Situ Vaccine Delivery to Treat Ovarian Cancer. *Adv. Sci.* **2018**, *5* (5), 1700991. https://doi.org/10.1002/advs.201700991.
(113) Sainsbury, F.; Saxena, P.; Aljabali, A. A. A.; Saunders, K.; Evans, D. J.; Lomonossoff, G. P. Genetic Engineering and Characterization of Cowpea Mosaic Virus Empty Virus-Like Particles. In *Virus Hybrids as Nanomaterials: Methods and Protocols*; Lin, B., Ratna, B., Eds.; Methods in Molecular Biology; Humana Press: Totowa, NJ, 2014; pp 139–153. https://doi.org/10.1007/978-1-62703-751-8_11.
(114) Liu, P.-F.; Wang, Y.; Ulrich, R. G.; Simmons, C. W.; VanderGheynst, J. S.; Gallo, R. L.; Huang, C.-M. Leaf-Encapsulated Vaccines: Agroinfiltration and Transient Expression of the Antigen *Staphylococcal Endotoxin* B in Radish Leaves. *J. Immunol. Res.* **2018**, *2018*, e3710961. https://doi.org/10.1155/2018/3710961.
(115) De Castro, C.; Molinaro, A.; Lanzetta, R.; Silipo, A.; Parrilli, M. Lipopolysaccharide Structures from Agrobacterium and Rhizobiaceae Species. *Carbohydr. Res.* **2008**, *343* (12), 1924–1933. https://doi.org/10.1016/j.carres.2008.01.036.
(116) Fuenmayor, J.; Gòdia, F.; Cervera, L. Production of Virus-like Particles for Vaccines. *New Biotechnol.* **2017**, *39*, 174–180. https://doi.org/10.1016/j.nbt.2017.07.010.

(117) Ochoa, W. F.; Chatterji, A.; Lin, T.; Johnson, J. E. Generation and Structural Analysis of Reactive Empty Particles Derived from an Icosahedral Virus. *Chem. Biol.* **2006**, *13* (7), 771–778. https://doi.org/10.1016/j.chembiol.2006.05.014.
(118) Machida, K.; Imataka, H. Production Methods for Viral Particles. *Biotechnol. Lett.* **2015**, *37* (4), 753–760. https://doi.org/10.1007/s10529-014-1741-9.
(119) Steinmetz, N. F.; Evans, D. J.; Lomonossoff, G. P. Chemical Introduction of Reactive Thiols Into a Viral Nanoscaffold: A Method That Avoids Virus Aggregation. *ChemBioChem* **2007**, *8* (10), 1131–1136. https://doi.org/10.1002/cbic.200700126.
(120) Lomonossoff, G. p.; Shanks, M. The Nucleotide Sequence of Cowpea Mosaic Virus B RNA. *EMBO J.* **1983**, *2* (12), 2253–2258. https://doi.org/10.1002/j.1460-2075.1983.tb01731.x.
(121) van Wezenbeek, P.; Verver, J.; Harmsen, J.; Vos, P.; van Kammen, A. Primary Structure and Gene Organization of the Middle-Component RNA of Cowpea Mosaic Virus. *EMBO J.* **1983**, *2* (6), 941–946. https://doi.org/10.1002/j.1460-2075.1983.tb01525.x.
(122) Hesketh, E. L.; Meshcheriakova, Y.; Dent, K. C.; Saxena, P.; Thompson, R. F.; Cockburn, J. J.; Lomonossoff, G. P.; Ranson, N. A. Mechanisms of Assembly and Genome Packaging in an RNA Virus Revealed by High-Resolution Cryo-EM. *Nat. Commun.* **2015**, *6* (1), 10113. https://doi.org/10.1038/ncomms10113.
(123) Yildiz, I.; Lee, K. L.; Chen, K.; Shukla, S.; Steinmetz, N. F. Infusion of Imaging and Therapeutic Molecules into the Plant Virus-Based Carrier Cowpea Mosaic Virus: Cargo-Loading and Delivery. *J. Controlled Release* **2013**, *172* (2), 568–578. https://doi.org/10.1016/j.jconrel.2013.04.023.
(124) Fraenkel-Conrat, H. *Comprehensive Virology: Descriptive Catalogue of Viruses*; Springer Science & Business Media, 2012.
(125) Glasel, J. A. Validity of Nucleic Acid Purities Monitored by 260nm/280nm Absorbance Ratios. *BioTechniques* **1995**, *18* (1), 62–63.
(126) Hesketh, E. L.; Meshcheriakova, Y.; Thompson, R. F.; Lomonossoff, G. P.; Ranson, N. A. The Structures of a Naturally Empty Cowpea Mosaic Virus Particle and Its Genome-Containing Counterpart by Cryo-Electron Microscopy. *Sci. Rep.* **2017**, *7* (1), 539. https://doi.org/10.1038/s41598-017-00533-w.
(127) Scheres, S. H. W. RELION: Implementation of a Bayesian Approach to Cryo-EM Structure Determination. *J. Struct. Biol.* **2012**, *180* (3), 519–530. https://doi.org/10.1016/j.jsb.2012.09.006.
(128) Hansen, L. J. J.; Daoussi, R.; Vervaet, C.; Remon, J.-P.; De Beer, T. R. M. Freeze-Drying of Live Virus Vaccines: A Review. *Vaccine* **2015**, *33* (42), 5507–5519. https://doi.org/10.1016/j.vaccine.2015.08.085.
(129) Cicerone, M. T.; Pikal, M. J.; Qian, K. K. Stabilization of Proteins in Solid Form. *Adv. Drug Deliv. Rev.* **2015**, *93*, 14–24. https://doi.org/10.1016/j.addr.2015.05.006.
(130) Tang, G.; Peng, L.; Baldwin, P. R.; Mann, D. S.; Jiang, W.; Rees, I.; Ludtke, S. J. EMAN2: An Extensible Image Processing Suite for Electron Microscopy. *J. Struct. Biol.* **2007**, *157* (1), 38–46. https://doi.org/10.1016/j.jsb.2006.05.009.
(131) Rohou, A.; Grigorieff, N. CTFFIND4: Fast and Accurate Defocus Estimation from Electron Micrographs. *J. Struct. Biol.* **2015**, *192* (2), 216–221. https://doi.org/10.1016/j.jsb.2015.08.008.

(132) Pettersen, E. F.; Goddard, T. D.; Huang, C. C.; Couch, G. S.; Greenblatt, D. M.; Meng, E. C.; Ferrin, T. E. UCSF Chimera—A Visualization System for Exploratory Research and Analysis. *J. Comput. Chem.* **2004**, *25* (13), 1605–1612. https://doi.org/10.1002/jcc.20084.
(133) Lee, D. H. Update of Early Phase Clinical Trials in Cancer Immunotherapy. *BMB Rep.* **2021**, *54* (1), 70–88. https://doi.org/10.5483/BMBRep.2021.54.1.242.
(134) Riley, R. S.; June, C. H.; Langer, R.; Mitchell, M. J. Delivery Technologies for Cancer Immunotherapy. *Nat. Rev. Drug Discov.* **2019**, *18* (3), 175–196. https://doi.org/10.1038/s41573-018-0006-z.
(135) Cai, H.; Wang, C.; Shukla, S.; Steinmetz, N. F. Cowpea Mosaic Virus Immunotherapy Combined with Cyclophosphamide Reduces Breast Cancer Tumor Burden and Inhibits Lung Metastasis. *Adv. Sci. Weinh. Baden-Wurtt. Ger.* **2019**, *6* (16), 1802281. https://doi.org/10.1002/advs.201802281.
(136) Mao, C.; Beiss, V.; Fields, J.; Steinmetz, N. F.; Fiering, S. Cowpea Mosaic Virus Stimulates Antitumor Immunity through Recognition by Multiple MYD88-Dependent Toll-like Receptors. *Biomaterials* **2021**, *275*, 120914. https://doi.org/10.1016/j.biomaterials.2021.120914.
(137) Nkanga, C. I.; Steinmetz, N. F. Injectable Hydrogel Containing Cowpea Mosaic Virus Nanoparticles Prevents Colon Cancer Growth. *ACS Biomater. Sci. Eng.* **2022**, *8* (6), 2518–2525. https://doi.org/10.1021/acsbiomaterials.2c00284.
(138) Chariou, P. L.; Beiss, V.; Ma, Y.; Steinmetz, N. F. In Situ Vaccine Application of Inactivated CPMV Nanoparticles for Cancer Immunotherapy. *Mater. Adv.* **2021**, *2* (5), 1644–1656. https://doi.org/10.1039/D0MA00752H.
(139) Wang, C.; Fernández de Ávila, B. E.; Mundaca-Uribe, R.; Lopez-Ramirez, M. A.; Ramírez-Herrera, D. E.; Shukla, S.; Steinmetz, N. F.; Wang, J. Active Delivery of VLPs Promotes Anti-Tumor Activity in a Mouse Ovarian Tumor Model. *Small* **2020**, *16* (20), 1907150. https://doi.org/10.1002/smll.201907150.
(140) Shukla, S.; Wang, C.; Beiss, V.; Cai, H.; Washington, T.; Murray, A. A.; Gong, X.; Zhao, Z.; Masarapu, H.; Zlotnick, A.; Fiering, S.; Steinmetz, N. F. The Unique Potency of Cowpea Mosaic Virus (CPMV) in Situ Cancer Vaccine. *Biomater. Sci.* **2020**, *8* (19), 5489–5503. https://doi.org/10.1039/d0bm01219j.
(141) Tiwari, R. V.; Patil, H.; Repka, M. A. Contribution of Hot-Melt Extrusion Technology to Advance Drug Delivery in the 21st Century. *Expert Opin. Drug Deliv.* **2016**, *13* (3), 451–464. https://doi.org/10.1517/17425247.2016.1126246.
(142) Ortega-Rivera, O. A.; Shukla, S.; Shin, M. D.; Chen, A.; Beiss, V.; Moreno-Gonzalez, M. A.; Zheng, Y.; Clark, A. E.; Carlin, A. F.; Pokorski, J. K.; Steinmetz, N. F. Cowpea Mosaic Virus Nanoparticle Vaccine Candidates Displaying Peptide Epitopes Can Neutralize the Severe Acute Respiratory Syndrome Coronavirus. *ACS Infect. Dis.* **2021**, *7* (11), 3096–3110. https://doi.org/10.1021/acsinfecdis.1c00410.
(143) Shao, S.; Ortega-Rivera, O. A.; Ray, S.; Pokorski, J. K.; Steinmetz, N. F. A Scalable Manufacturing Approach to Single Dose Vaccination against HPV. *Vaccines* **2021**, *9* (1), 66. https://doi.org/10.3390/vaccines9010066.
(144) Lee, P. W.; Shukla, S.; Wallat, J. D.; Danda, C.; Steinmetz, N. F.; Maia, J.; Pokorski, J. K. Biodegradable Viral Nanoparticle/Polymer Implants Prepared via Melt-Processing. *ACS Nano* **2017**, *11* (9), 8777–8789. https://doi.org/10.1021/acsnano.7b02786.

(145) Amouzegar, A.; Chelvanambi, M.; Filderman, J. N.; Storkus, W. J.; Luke, J. J. STING Agonists as Cancer Therapeutics. *Cancers* **2021**, *13* (11), 2695. https://doi.org/10.3390/cancers13112695.
(146) Ramanjulu, J. M.; Pesiridis, G. S.; Yang, J.; Concha, N.; Singhaus, R.; Zhang, S.-Y.; Tran, J.-L.; Moore, P.; Lehmann, S.; Eberl, H. C.; Muelbaier, M.; Schneck, J. L.; Clemens, J.; Adam, M.; Mehlmann, J.; Romano, J.; Morales, A.; Kang, J.; Leister, L.; Graybill, T. L.; Charnley, A. K.; Ye, G.; Nevins, N.; Behnia, K.; Wolf, A. I.; Kasparcova, V.; Nurse, K.; Wang, L.; Puhl, A. C.; Li, Y.; Klein, M.; Hopson, C. B.; Guss, J.; Bantscheff, M.; Bergamini, G.; Reilly, M. A.; Lian, Y.; Duffy, K. J.; Adams, J.; Foley, K. P.; Gough, P. J.; Marquis, R. W.; Smothers, J.; Hoos, A.; Bertin, J. Design of Amidobenzimidazole STING Receptor Agonists with Systemic Activity. *Nature* **2018**, *564* (7736), 439–443. https://doi.org/10.1038/s41586-018-0705-y.
(147) Li, C.; Zhang, Y.; Wan, Y.; Wang, J.; Lin, J.; Li, Z.; Huang, P. STING-Activating Drug Delivery Systems: Design Strategies and Biomedical Applications. *Chin. Chem. Lett.* **2021**, *32* (5), 1615–1625. https://doi.org/10.1016/j.cclet.2021.01.001.
(148) *Removal of NEXPLANON® (etonogestrel implant) 68 mg Radiopaque*. https://www.nexplanon.com/removal/ (accessed 2022-12-01).
(149) Makadia, H. K.; Siegel, S. J. Poly Lactic-Co-Glycolic Acid (PLGA) as Biodegradable Controlled Drug Delivery Carrier. *Polymers* **2011**, *3* (3), 1377–1397. https://doi.org/10.3390/polym3031377.
(150) Wirth, D. M.; Pokorski, J. K. Design and Fabrication of a Low-Cost Pilot-Scale Melt-Processing System. *Polymer* **2019**, *181*, 121802. https://doi.org/10.1016/j.polymer.2019.121802.
(151) Wang, K. *Die Swell of Complex Polymeric Systems*; IntechOpen, 2012. https://doi.org/10.5772/50137.
(152) Leonov, A. I.; Prokunin, A. N. On the Stretching and Swelling of an Elastic Liquid Extruded from a Capillary Die. *Rheol. Acta* **1984**, *23* (1), 62–69. https://doi.org/10.1007/BF01333876.
(153) Uthaman, S.; Huh, K. M.; Park, I.-K. Tumor Microenvironment-Responsive Nanoparticles for Cancer Theragnostic Applications. *Biomater. Res.* **2018**, *22*, 22. https://doi.org/10.1186/s40824-018-0132-z.
(154) Zheng, Y.; Lee, P. W.; Wang, C.; Thomas, L. D.; Stewart, P. L.; Steinmetz, N. F.; Pokorski, J. K. Freeze-Drying To Produce Efficacious CPMV Virus-like Particles. *Nano Lett.* **2019**, *19* (3), 2099–2105. https://doi.org/10.1021/acs.nanolett.9b00300.
(155) Ghalanbor, Z.; Körber, M.; Bodmeier, R. Improved Lysozyme Stability and Release Properties of Poly(Lactide-Co-Glycolide) Implants Prepared by Hot-Melt Extrusion. *Pharm. Res.* **2010**, *27* (2), 371–379. https://doi.org/10.1007/s11095-009-0033-x.
(156) *Characterization of Nanoparticles Intended for Drug Delivery*; McNeil, S. E., Ed.; Methods in Molecular Biology; Springer New York: New York, NY, 2018; Vol. 1682. https://doi.org/10.1007/978-1-4939-7352-1.
(157) Hönig, W.; Kula, M.-R. Selectivity of Protein Precipitation with Polyethylene Glycol Fractions of Various Molecular Weights. *Anal. Biochem.* **1976**, *72* (1), 502–512. https://doi.org/10.1016/0003-2697(76)90560-1.
(158) Ingham, K. C. [20] Protein Precipitation with Polyethylene Glycol. In *Methods in Enzymology*; Part C: Enzyme Purification and Related Techniques; Academic Press, 1984; Vol. 104, pp 351–356. https://doi.org/10.1016/S0076-6879(84)04101-X.

(159) Company, T. D. C. CARBOWAX^{TM} Polyethylene Glycol (PEG) 3350. 1.
(160) 118-01806-01-Carbowax-Polyethylene-Glycol-Peg-8000-Tds.Pdf. https://www.dow.com/content/dam/dcc/documents/en-us/productdatasheet/118/118-01806-01-carbowax-polyethylene-glycol-peg-8000-tds.pdf (accessed 2022-12-02).
(161) Wang, C.; Fiering, S. N.; Steinmetz, N. F. Cowpea Mosaic Virus Promotes Anti-Tumor Activity and Immune Memory in a Mouse Ovarian Tumor Model. *Adv. Ther.* **2019**, *2* (5), 1900003. https://doi.org/10.1002/adtp.201900003.
(162) Liang, Y.; Offenhäusser, A.; Ingebrandt, S.; Mayer, D. PEDOT:PSS-Based Bioelectronic Devices for Recording and Modulation of Electrophysiological and Biochemical Cell Signals. *Adv. Healthc. Mater.* **2021**, *10* (11), 2100061. https://doi.org/10.1002/adhm.202100061.
(163) Xia, Y.; Dai, S. Review on Applications of PEDOTs and PEDOT:PSS in Perovskite Solar Cells. *J. Mater. Sci. Mater. Electron.* **2021**, *32* (10), 12746–12757. https://doi.org/10.1007/s10854-020-03473-w.
(164) Sun, K.; Zhang, S.; Li, P.; Xia, Y.; Zhang, X.; Du, D.; Isikgor, F. H.; Ouyang, J. Review on Application of PEDOTs and PEDOT:PSS in Energy Conversion and Storage Devices. *J. Mater. Sci. Mater. Electron.* **2015**, *26* (7), 4438–4462. https://doi.org/10.1007/s10854-015-2895-5.
(165) Fan, X.; Nie, W.; Tsai, H.; Wang, N.; Huang, H.; Cheng, Y.; Wen, R.; Ma, L.; Yan, F.; Xia, Y. PEDOT:PSS for Flexible and Stretchable Electronics: Modifications, Strategies, and Applications. *Adv. Sci.* **2019**, *6* (19), 1900813. https://doi.org/10.1002/advs.201900813.
(166) Boehler, C.; Aqrawe, Z.; Asplund, M. Applications of PEDOT in Bioelectronic Medicine. *Bioelectron. Med.* **2019**, *2* (2), 89–99. https://doi.org/10.2217/bem-2019-0014.
(167) Garma, L. D.; Ferrari, L. M.; Scognamiglio, P.; Greco, F.; Santoro, F. Inkjet-Printed PEDOT:PSS Multi-Electrode Arrays for Low-Cost in Vitro Electrophysiology. *Lab. Chip* **2019**, *19* (22), 3776–3786. https://doi.org/10.1039/C9LC00636B.
(168) Xiong, Z.; Liu, C. Optimization of Inkjet Printed PEDOT:PSS Thin Films through Annealing Processes. *Org. Electron.* **2012**, *13* (9), 1532–1540. https://doi.org/10.1016/j.orgel.2012.05.005.
(169) Ouyang, S.; Xie, Y.; Wang, D.; Zhu, D.; Xu, X.; Tan, T.; Fong, H. H. Surface Patterning of PEDOT:PSS by Photolithography for Organic Electronic Devices. *J. Nanomater.* **2015**, *2015*, e603148. https://doi.org/10.1155/2015/603148.
(170) Feig, V. R.; Tran, H.; Lee, M.; Liu, K.; Huang, Z.; Beker, L.; Mackanic, D. G.; Bao, Z. An Electrochemical Gelation Method for Patterning Conductive PEDOT:PSS Hydrogels. *Adv. Mater.* **2019**, *31* (39), 1902869. https://doi.org/10.1002/adma.201902869.
(171) Li, J.; Chang, X.; Li, S.; Shrestha, P. K.; Tan, E. K. W.; Chu, D. High-Resolution Electrochemical Transistors Defined by Mold-Guided Drying of PEDOT:PSS Liquid Suspension. *ACS Appl. Electron. Mater.* **2020**, *2* (8), 2611–2618. https://doi.org/10.1021/acsaelm.0c00491.
(172) Tarabella, G.; Vurro, D.; Lai, S.; D'Angelo, P.; Ascari, L.; Iannotta, S. Aerosol Jet Printing of PEDOT:PSS for Large Area Flexible Electronics. *Flex. Print. Electron.* **2020**, *5* (1), 014005. https://doi.org/10.1088/2058-8585/ab61c4.
(173) Thompson, B.; Yoon, H.-S. Aerosol-Printed Strain Sensor Using PEDOT:PSS. *IEEE Sens. J.* **2013**, *13* (11), 4256–4263. https://doi.org/10.1109/JSEN.2013.2264482.

(174) Pali, L. S.; Jindal, R.; Garg, A. Screen Printed PEDOT:PSS Films as Transparent Electrode and Its Application in Organic Solar Cells on Opaque Substrates. *J. Mater. Sci. Mater. Electron.* **2018**, *29* (13), 11030–11038. https://doi.org/10.1007/s10854-018-9185-y.
(175) Sinha, S. K.; Noh, Y.; Reljin, N.; Treich, G. M.; Hajeb-Mohammadalipour, S.; Guo, Y.; Chon, K. H.; Sotzing, G. A. Screen-Printed PEDOT:PSS Electrodes on Commercial Finished Textiles for Electrocardiography. *ACS Appl. Mater. Interfaces* **2017**, *9* (43), 37524–37528. https://doi.org/10.1021/acsami.7b09954.
(176) Zhang, P.; Travas-Sejdic, J. Fabrication of Conducting Polymer Microelectrodes and Microstructures for Bioelectronics. *J. Mater. Chem. C* **2021**, *9* (31), 9730–9760. https://doi.org/10.1039/D1TC01618K.
(177) Yuk, H.; Lu, B.; Lin, S.; Qu, K.; Xu, J.; Luo, J.; Zhao, X. 3D Printing of Conducting Polymers. *Nat. Commun.* **2020**, *11* (1), 1604. https://doi.org/10.1038/s41467-020-15316-7.
(178) Xu, Y.; Yang, X.; Thomas, A. K.; Patsis, P. A.; Kurth, T.; Kräter, M.; Eckert, K.; Bornhäuser, M.; Zhang, Y. Noncovalently Assembled Electroconductive Hydrogel. *ACS Appl. Mater. Interfaces* **2018**, *10* (17), 14418–14425. https://doi.org/10.1021/acsami.8b01029.
(179) Lu, B.; Yuk, H.; Lin, S.; Jian, N.; Qu, K.; Xu, J.; Zhao, X. Pure PEDOT:PSS Hydrogels. *Nat. Commun.* **2019**, *10* (1), 1043. https://doi.org/10.1038/s41467-019-09003-5.
(180) Teo, M. Y.; RaviChandran, N.; Kim, N.; Kee, S.; Stuart, L.; Aw, K. C.; Stringer, J. Direct Patterning of Highly Conductive PEDOT:PSS/Ionic Liquid Hydrogel via Microreactive Inkjet Printing. *ACS Appl. Mater. Interfaces* **2019**, *11* (40), 37069–37076. https://doi.org/10.1021/acsami.9b12069.
(181) Tagliaferri, S.; Panagiotopoulos, A.; Mattevi, C. Direct Ink Writing of Energy Materials. *Mater. Adv.* **2021**, *2* (2), 540–563. https://doi.org/10.1039/D0MA00753F.
(182) Zhang, Q.; Zhou, J.; Chen, Z.; Xu, C.; Tang, W.; Yang, G.; Lai, C.; Xu, Q.; Yang, J.; Peng, C. Direct Ink Writing of Moldable Electrochemical Energy Storage Devices: Ongoing Progress, Challenges, and Prospects. *Adv. Eng. Mater.* **2021**, *23* (7), 2100068. https://doi.org/10.1002/adem.202100068.
(183) Rivnay, J.; Wang, H.; Fenno, L.; Deisseroth, K.; Malliaras, G. G. Next-Generation Probes, Particles, and Proteins for Neural Interfacing. *Sci. Adv.* **2017**, *3* (6), e1601649. https://doi.org/10.1126/sciadv.1601649.
(184) Zhang, S.; Chen, Y.; Liu, H.; Wang, Z.; Ling, H.; Wang, C.; Ni, J.; Çelebi-Saltik, B.; Wang, X.; Meng, X.; Kim, H.-J.; Baidya, A.; Ahadian, S.; Ashammakhi, N.; Dokmeci, M. R.; Travas-Sejdic, J.; Khademhosseini, A. Room-Temperature-Formed PEDOT:PSS Hydrogels Enable Injectable, Soft, and Healable Organic Bioelectronics. *Adv. Mater.* **2020**, *32* (1), 1904752. https://doi.org/10.1002/adma.201904752.
(185) Gratson, G. M.; Xu, M.; Lewis, J. A. Direct Writing of Three-Dimensional Webs. *Nature* **2004**, *428* (6981), 386–386. https://doi.org/10.1038/428386a.
(186) Kim, N.; Kee, S.; Lee, S. H.; Lee, B. H.; Kahng, Y. H.; Jo, Y.-R.; Kim, B.-J.; Lee, K. Highly Conductive PEDOT:PSS Nanofibrils Induced by Solution-Processed Crystallization. *Adv. Mater.* **2014**, *26* (14), 2268–2272. https://doi.org/10.1002/adma.201304611.
(187) Kim, N.; Lee, B. H.; Choi, D.; Kim, G.; Kim, H.; Kim, J.-R.; Lee, J.; Kahng, Y. H.; Lee, K. Role of Interchain Coupling in the Metallic State of Conducting Polymers. *Phys. Rev. Lett.* **2012**, *109* (10), 106405. https://doi.org/10.1103/PhysRevLett.109.106405.

(188) Aasmundtveit, K. E.; Samuelsen, E. J.; Pettersson, L. A. A.; Inganäs, O.; Johansson, T.; Feidenhans'l, R. Structure of Thin Films of Poly(3,4-Ethylenedioxythiophene). *Synth. Met.* **1999**, *101* (1), 561–564. https://doi.org/10.1016/S0379-6779(98)00315-4.
(189) Murthy, N. S.; Minor, H. General Procedure for Evaluating Amorphous Scattering and Crystallinity from X-Ray Diffraction Scans of Semicrystalline Polymers. *Polymer* **1990**, *31* (6), 996–1002. https://doi.org/10.1016/0032-3861(90)90243-R.
(190) Garreau, S.; Louarn, G.; Buisson, J. P.; Froyer, G.; Lefrant, S. In Situ Spectroelectrochemical Raman Studies of Poly(3,4-Ethylenedioxythiophene) (PEDT). *Macromolecules* **1999**, *32* (20), 6807–6812. https://doi.org/10.1021/ma9905674.
(191) Jucius, D.; Lazauskas, A.; Grigaliūnas, V.; Gudaitis, R.; Guobienė, A.; Prosyčevas, I.; Abakevičienė, B.; Andrulevičius, M. Structure and Properties of Dual-Doped PEDOT:PSS Multilayer Films. *Mater. Res.* **2019**, *22*. https://doi.org/10.1590/1980-5373-MR-2019-0134.
(192) Chiu, W. W.; Travaš-Sejdić, J.; Cooney, R. P.; Bowmaker, G. A. Spectroscopic and Conductivity Studies of Doping in Chemically Synthesized Poly(3,4-Ethylenedioxythiophene). *Synth. Met.* **2005**, *155* (1), 80–88. https://doi.org/10.1016/j.synthmet.2005.06.012.
(193) Kara, M. O. P.; Frey, M. W. Effects of Solvents on the Morphology and Conductivity of Poly(3,4-Ethylenedioxythiophene):Poly(Styrenesulfonate) Nanofibers. *J. Appl. Polym. Sci.* **2014**, *131* (11). https://doi.org/10.1002/app.40305.
(194) Lee, S. H.; Park, H.; Kim, S.; Son, W.; Cheong, I. W.; Kim, J. H. Transparent and Flexible Organic Semiconductor Nanofilms with Enhanced Thermoelectric Efficiency. *J. Mater. Chem. A* **2014**, *2* (20), 7288–7294. https://doi.org/10.1039/C4TA00700J.
(195) Chang, C. L.; Lai, P. Y.; Li, Y. Y.; Lai, Y. P.; Huang, C. W.; Chen, S. H.; Lee, Y. W.; Huang, S. L. Parasitic Stimulated Amplification in High-Peak-Power and Diode-Seeded Nanosecond Fiber Amplifiers. *IEEE Photonics J.* **2014**, *6* (3), 1–8. https://doi.org/10.1109/JPHOT.2014.2319090.
(196) Cho, N.; Squair, J. W.; Bloch, J.; Courtine, G. Neurorestorative Interventions Involving Bioelectronic Implants after Spinal Cord Injury. *Bioelectron. Med.* **2019**, *5* (1), 10. https://doi.org/10.1186/s42234-019-0027-x.
(197) Inoue, A.; Yuk, H.; Lu, B.; Zhao, X. Strong Adhesion of Wet Conducting Polymers on Diverse Substrates. *Sci. Adv.* **2020**, *6* (12), eaay5394. https://doi.org/10.1126/sciadv.aay5394.
(198) Ouyang, L.; Wei, B.; Kuo, C.; Pathak, S.; Farrell, B.; Martin, D. C. Enhanced PEDOT Adhesion on Solid Substrates with Electrografted P(EDOT-NH2). *Sci. Adv.* **2017**, *3* (3), e1600448. https://doi.org/10.1126/sciadv.1600448.
(199) Boehler, C.; Oberueber, F.; Schlabach, S.; Stieglitz, T.; Asplund, M. Long-Term Stable Adhesion for Conducting Polymers in Biomedical Applications: IrOx and Nanostructured Platinum Solve the Chronic Challenge. *ACS Appl. Mater. Interfaces* **2017**, *9* (1), 189–197. https://doi.org/10.1021/acsami.6b13468.
(200) Pranti, A. S.; Schander, A.; Bödecker, A.; Lang, W. Highly Stable PEDOT:PSS Coating on Gold Microelectrodes with Improved Charge Injection Capacity for Chronic Neural Stimulation. *Proceedings* **2017**, *1* (4), 492. https://doi.org/10.3390/proceedings1040492.
(201) Sadekar, A. G.; Mohite, D.; Mulik, S.; Chandrasekaran, N.; Sotiriou-Leventis, C.; Leventis, N. Robust PEDOT Films by Covalent Bonding to Substrates Using in Tandem

Sol–Gel, Surface Initiated Free-Radical and Redox Polymerization. *J. Mater. Chem.* **2011**, *22* (1), 100–108. https://doi.org/10.1039/C1JM12563J.
(202) Wei, B.; Liu, J.; Ouyang, L.; Kuo, C.-C.; Martin, D. C. Significant Enhancement of PEDOT Thin Film Adhesion to Inorganic Solid Substrates with EDOT-Acid. *ACS Appl. Mater. Interfaces* **2015**, *7* (28), 15388–15394. https://doi.org/10.1021/acsami.5b03350.
(203) *Flexible Hybrid Electronics: Strategies to Enable Cheaper Substrates*. IDTechEx. https://www.idtechex.com/en/research-article/flexible-hybrid-electronics-strategies-to-enable-cheaper-substrates/20975 (accessed 2022-12-05).
(204) Wang, B.; Baeuscher, M.; Hu, X.; Woehrmann, M.; Becker, K.; Juergensen, N.; Hubl, M.; Mackowiak, P.; Schneider-Ramelow, M.; Lang, K.-D.; Ngo, H.-D. Development and Characterization of a Novel Low-Cost Water-Level and Water Quality Monitoring Sensor by Using Enhanced Screen Printing Technology with PEDOT:PSS. *Micromachines* **2020**, *11* (5), 474. https://doi.org/10.3390/mi11050474.
(205) Hua, L.; Zhou, R.; Thirumalai, D.; Berne, B. J. Urea Denaturation by Stronger Dispersion Interactions with Proteins than Water Implies a 2-Stage Unfolding. *Proc. Natl. Acad. Sci.* **2008**, *105* (44), 16928–16933. https://doi.org/10.1073/pnas.0808427105.
(206) Gulino, M.; Kim, D.; Pané, S.; Santos, S. D.; Pêgo, A. P. Tissue Response to Neural Implants: The Use of Model Systems Toward New Design Solutions of Implantable Microelectrodes. *Front. Neurosci.* **2019**, *13*.
(207) Miller, K. J.; Hermes, D.; Staff, N. P. The Current State of Electrocorticography-Based Brain–Computer Interfaces. *Neurosurg. Focus* **2020**, *49* (1), E2. https://doi.org/10.3171/2020.4.FOCUS20185.
(208) Kim, G. H.; Kim, K.; Lee, E.; An, T.; Choi, W.; Lim, G.; Shin, J. H. Recent Progress on Microelectrodes in Neural Interfaces. *Materials* **2018**, *11* (10), 1995. https://doi.org/10.3390/ma11101995.
(209) Chen, T.-W.; Wardill, T. J.; Sun, Y.; Pulver, S. R.; Renninger, S. L.; Baohan, A.; Schreiter, E. R.; Kerr, R. A.; Orger, M. B.; Jayaraman, V.; Looger, L. L.; Svoboda, K.; Kim, D. S. Ultrasensitive Fluorescent Proteins for Imaging Neuronal Activity. *Nature* **2013**, *499* (7458), 295–300. https://doi.org/10.1038/nature12354.
(210) Park, D.-W.; Ness, J. P.; Brodnick, S. K.; Esquibel, C.; Novello, J.; Atry, F.; Baek, D.-H.; Kim, H.; Bong, J.; Swanson, K. I.; Suminski, A. J.; Otto, K. J.; Pashaie, R.; Williams, J. C.; Ma, Z. Electrical Neural Stimulation and Simultaneous in Vivo Monitoring with Transparent Graphene Electrode Arrays Implanted in GCaMP6f Mice. *ACS Nano* **2018**, *12* (1), 148–157. https://doi.org/10.1021/acsnano.7b04321.
(211) Ghanbari, L.; Carter, R. E.; Rynes, M. L.; Dominguez, J.; Chen, G.; Naik, A.; Hu, J.; Sagar, M. A. K.; Haltom, L.; Mossazghi, N.; Gray, M. M.; West, S. L.; Eliceiri, K. W.; Ebner, T. J.; Kodandaramaiah, S. B. Cortex-Wide Neural Interfacing via Transparent Polymer Skulls. *Nat. Commun.* **2019**, *10* (1), 1500. https://doi.org/10.1038/s41467-019-09488-0.
(212) Yazdan-Shahmorad, A.; Kipke, D. R.; Lehmkuhle, M. J. Polarity of Cortical Electrical Stimulation Differentially Affects Neuronal Activity of Deep and Superficial Layers of Rat Motor Cortex. *Brain Stimulat.* **2011**, *4* (4), 228–241. https://doi.org/10.1016/j.brs.2010.11.004.
(213) Cogan, S. F. Neural Stimulation and Recording Electrodes. *Annu. Rev. Biomed. Eng.* **2008**, *10* (1), 275–309. https://doi.org/10.1146/annurev.bioeng.10.061807.160518.

(214) Dell, R. B.; Holleran, S.; Ramakrishnan, R. Sample Size Determination. *ILAR J.* **2002**, *43* (4), 207–213. https://doi.org/10.1093/ilar.43.4.207.
(215) Gomez-Tames, J.; Asai, A.; Hirata, A. Multiscale Computational Model Reveals Nerve Response in a Mouse Model for Temporal Interference Brain Stimulation. *Front. Neurosci.* **2021**, *15*, 684465. https://doi.org/10.3389/fnins.2021.684465.
(216) Asan, A. S.; Gok, S.; Sahin, M. Electrical Fields Induced inside the Rat Brain with Skin, Skull, and Dural Placements of the Current Injection Electrode. *PLOS ONE* **2019**, *14* (1), e0203727. https://doi.org/10.1371/journal.pone.0203727.
(217) Paschen, E.; Elgueta, C.; Heining, K.; Vieira, D. M.; Kleis, P.; Orcinha, C.; Häussler, U.; Bartos, M.; Egert, U.; Janz, P.; Haas, C. A. Hippocampal Low-Frequency Stimulation Prevents Seizure Generation in a Mouse Model of Mesial Temporal Lobe Epilepsy. *eLife* **2020**, *9*, e54518. https://doi.org/10.7554/eLife.54518.
(218) Shannon, R. V. A Model of Safe Levels for Electrical Stimulation. *IEEE Trans. Biomed. Eng.* **1992**, *39* (4), 424–426. https://doi.org/10.1109/10.126616.
(219) Kunori, N.; Takashima, I. A Transparent Epidural Electrode Array for Use in Conjunction with Optical Imaging. *J. Neurosci. Methods* **2015**, *251*, 130–137. https://doi.org/10.1016/j.jneumeth.2015.05.018.
(220) Kim, J.; Kim, M.; Lee, M.-S.; Kim, K.; Ji, S.; Kim, Y.-T.; Park, J.; Na, K.; Bae, K.-H.; Kyun Kim, H.; Bien, F.; Young Lee, C.; Park, J.-U. Wearable Smart Sensor Systems Integrated on Soft Contact Lenses for Wireless Ocular Diagnostics. *Nat. Commun.* **2017**, *8* (1), 14997. https://doi.org/10.1038/ncomms14997.
(221) Yang, C.; Wu, Q.; Liu, J.; Mo, J.; Li, X.; Yang, C.; Liu, Z.; Yang, J.; Jiang, L.; Chen, W.; Chen, H.; Wang, J.; Xie, X. Intelligent Wireless Theranostic Contact Lens for Electrical Sensing and Regulation of Intraocular Pressure. *Nat. Commun.* **2022**, *13* (1), 2556. https://doi.org/10.1038/s41467-022-29860-x.
(222) Weng, Y.; Liu, J.; Jin, S.; Guo, W.; Liang, X.; Hu, Z. Nanotechnology-Based Strategies for Treatment of Ocular Disease. *Acta Pharm. Sin. B* **2017**, *7* (3), 281–291. https://doi.org/10.1016/j.apsb.2016.09.001.
(223) Yuan, X.; Marcano, D. C.; Shin, C. S.; Hua, X.; Isenhart, L. C.; Pflugfelder, S. C.; Acharya, G. Ocular Drug Delivery Nanowafer with Enhanced Therapeutic Efficacy. *ACS Nano* **2015**, *9* (2), 1749–1758. https://doi.org/10.1021/nn506599f.
(224) *Publications*. Steinmetz Lab. https://www.steinmetzlab.com/3011086-publications (accessed 2022-12-04).
(225) Vaajanen, A.; Vapaatalo, H. A Single Drop in the Eye – Effects on the Whole Body? *Open Ophthalmol. J.* **2017**, *11* (1). https://doi.org/10.2174/1874364101711010305.
(226) Ricci, M. *Bioelectronic wearable shows promise in psoriasis* -. https://pharmaphorum.com/news/bioelectronic-wearable-shows-promise-psoriasis/ (accessed 2022-12-06).
(227) Jung, E.; Mao, C.; Bhatia, M.; Koellhoffer, E. C.; Fiering, S. N.; Steinmetz, N. F. Inactivated Cowpea Mosaic Virus for In Situ Vaccination: Differential Efficacy of Formalin vs UV-Inactivated Formulations. *Mol. Pharm.* **2022**. https://doi.org/10.1021/acs.molpharmaceut.2c00744.
(228) Burke, A.; Chevreuil, M.; Paris, A.; de La Grange, V.; Goldmann, C.; Pérez, J.; Constantin, D.; Tresset, G. Nanoparticle-Templated Self-Assembly of Viral Capsids Probed by Time-Resolved Absorbance Spectroscopy and X-Ray Scattering. *Phys. Rev. Appl.* **2018**, *10* (5), 054065. https://doi.org/10.1103/PhysRevApplied.10.054065.

(229) Qiao, J.-N.; Yang, Q.-C.; Li, Y.; lv, Z.; Tang, J.-H.; Lei, J.; Li, Z.-M. Baroplastics with Ultrahigh Strength and Modulus via Hydrogen-Bonding Interactions with Agar. *ACS Appl. Polym. Mater.* **2020**, *2* (12), 5550–5557. https://doi.org/10.1021/acsapm.0c00892.
(230) Iwasaki, Y.; Takemoto, K.; Tanaka, S.; Taniguchi, I. Low-Temperature Processable Block Copolymers That Preserve the Function of Blended Proteins. *Biomacromolecules* **2016**, *17* (7), 2466–2471. https://doi.org/10.1021/acs.biomac.6b00641.
(231) Lv, Z.; Qiao, J.-N.; Song, Y.-N.; Ji, X.; Tang, J.-H.; Yan, D.-X.; Lei, J.; Li, Z.-M. Baroplastics with Robust Mechanical Properties and Reserved Processability through Hydrogen-Bonded Interactions. *ACS Appl. Mater. Interfaces* **2019**, *11* (12), 12008–12016. https://doi.org/10.1021/acsami.8b20676.
(232) Paulson, C. *Extrusion - Pressure, Temperature, Heating and Cooling Control*. Paulson Training Programs. https://www.paulsontraining.com/extrusion-pressure-temperature-heating-cooling-control/ (accessed 2022-12-06).
(233) Ameduri, B. The Promising Future of Fluoropolymers. *Macromol. Chem. Phys.* **2020**, *221* (8), 1900573. https://doi.org/10.1002/macp.201900573.
(234) Kannan, R. Y.; Salacinski, H. J.; Butler, P. E.; Hamilton, G.; Seifalian, A. M. Current Status of Prosthetic Bypass Grafts: A Review. *J. Biomed. Mater. Res. B Appl. Biomater.* **2005**, *74B* (1), 570–581. https://doi.org/10.1002/jbm.b.30247.
(235) Chen, G.; Wang, K.; Wang, Y.; Wu, P.; Sun, M.; Oupický, D. Fluorination Enhances Serum Stability of Bioreducible Poly(Amido Amine) Polyplexes and Enables Efficient Intravenous SiRNA Delivery. *Adv. Healthc. Mater.* **2018**, *7* (5), 1700978. https://doi.org/10.1002/adhm.201700978.
(236) Wang, L.-H.; Wu, D.-C.; Xu, H.-X.; You, Y.-Z. High DNA-Binding Affinity and Gene-Transfection Efficacy of Bioreducible Cationic Nanomicelles with a Fluorinated Core. *Angew. Chem. Int. Ed.* **2016**, *55* (2), 755–759. https://doi.org/10.1002/anie.201508695.
(237) Zhang, Z.; Shen, W.; Ling, J.; Yan, Y.; Hu, J.; Cheng, Y. The Fluorination Effect of Fluoroamphiphiles in Cytosolic Protein Delivery. *Nat. Commun.* **2018**, *9* (1), 1377. https://doi.org/10.1038/s41467-018-03779-8.
(238) Xu, J.; Li, Z.; Fan, Q.; Lv, J.; Li, Y.; Cheng, Y. Dynamic Polymer Amphiphiles for Efficient Intracellular and In Vivo Protein Delivery. *Adv. Mater.* **2021**, *33* (52), 2104355. https://doi.org/10.1002/adma.202104355.
(239) Song, T.; Gao, Y.; Song, M.; Qian, J.; Zhang, H.; Zhou, J.; Ding, Y. Fluoropolymers-Mediated Efficient Biomacromolecule Drug Delivery. *Med. Drug Discov.* **2022**, *14*, 100123. https://doi.org/10.1016/j.medidd.2022.100123.
(240) Wang, X.; Rong, G.; Yan, J.; Pan, D.; Wang, L.; Xu, Y.; Yang, M.; Cheng, Y. In Vivo Tracking of Fluorinated Polypeptide Gene Carriers by Positron Emission Tomography Imaging. *ACS Appl. Mater. Interfaces* **2020**, *12* (41), 45763–45771. https://doi.org/10.1021/acsami.0c11967.
(241) Huang, Y.; Chen, F.; Pan, Y.; Chen, C.; Jiang, L.; Dan, Y. Effect of Hydrophobic Fluoropolymer and Crystallinity on the Hydrolytic Degradation of Poly(Lactic Acid). *Eur. Polym. J.* **2017**, *97*, 308–318. https://doi.org/10.1016/j.eurpolymj.2017.09.044.
(242) Kwon, S. G.; Kwon, Y. W.; Lee, T. W.; Park, G. T.; Kim, J. H. Recent Advances in Stem Cell Therapeutics and Tissue Engineering Strategies. *Biomater. Res.* **2018**, *22*, 36. https://doi.org/10.1186/s40824-018-0148-4.

(243) Liu, X.; Zhou, L.; Zhang, F. Reactive Melt Extrusion To Improve the Dissolution Performance and Physical Stability of Naproxen Amorphous Solid Dispersions. *Mol. Pharm.* **2017**, *14* (3), 658–673. https://doi.org/10.1021/acs.molpharmaceut.6b00960.